

**Development of tetragonal Heusler
compounds with perpendicular
anisotropy for Magnetic Random Access
Memory applications**

Dissertation

zur Erlangung des Doktorgrades der Ingenieurwissenschaften (Dr. Ing.)

der

Naturwissenschaftlichen Fakultät II
Chemie, Physik und Mathematik

der Martin-Luther-Universität Halle-Wittenberg

vorgelegt von

Herrn **Yari Ferrante**
geb. am 21.12.1988 in Torino, Italia

Gutachter: Prof. Dr. Stuart S. P. Parkin
Prof. Dr. Georg Woltersdorf
Prof. Dr. Günter Reiss

Tag der öffentlichen Verteidigung: 17.10.2017

"ipsa scientia potestas est"
(knowledge itself is power)

Sir Francis Bacon
22/01/1561 – 09/04/1626

Contents

Contents	iii
List of Figures	vii
List of Tables	ix
Abbreviations	xi
1 Introduction	1
1.1 General introduction	1
1.2 Magnetic tunnel junctions and tunneling magnetoresistance effect	6
1.2.1 Symmetry spin filtering effect	8
1.3 Magnetic Random Access Memory	9
1.3.1 Toggle-MRAM vs. STT-MRAM	10
2 Heusler compounds	17
2.1 Introduction	17
2.2 Cubic compounds	19
2.3 Tetragonal compounds	21
2.3.1 Origin of tetragonal distortion	21
2.3.2 Perpendicular magnetocrystalline anisotropy arising from the tetragonal structure	24
2.3.3 Application of tetragonal Heuslers to STT-MRAM	27
2.3.4 $D0_{22}$ - Mn_3Ge	28
3 Thin films deposition system	31
3.1 Multichamber, all-vacuumed deposition system	31
3.2 The "G-system"	33
4 Buffer layers development and optimization	39
4.1 Introduction	39

4.2	Selection of buffer layers for the growth of tetragonal Mn_3Ge films	41
4.2.1	Si(001)/ SiO_2 /TaN/Ir Mn_3 (TI)	43
4.2.2	Si(001)/ SiO_2 /TaN/Ir Mn_3 /TaN (TIT)	45
4.2.3	MgO(001)/MgO/Cr (MC)	46
4.3	Summary	49
5	Mn_3Ge: a tetragonal Heusler compound with giant perpendicular magnetic anisotropy	51
5.1	Optimization of structural, morphological, and magnetic properties of Mn_3Ge thin films	51
5.1.1	Composition dependence	52
5.1.2	Growth temperature dependence and 3-step process	54
5.2	Mn_3Ge -based perpendicular magnetic tunnel junctions	58
5.2.1	Devices fabrication	58
5.2.2	Tunneling magnetoresistance properties	59
5.2.3	Theoretical calculations of TMR and influence of the Brillouin zone filtering effect	60
5.3	Summary	67
6	Doping Mn_3Ge with Cobalt: study of the structural, electronic and magnetic properties of a $\text{Mn}_{3-x}\text{Co}_x\text{Ge}$ system	69
6.1	Theoretical calculations	70
6.1.1	Influence of Cobalt doping on the Brillouin zone filtering effect	73
6.2	Experimental results and comparison with theoretical predictions	76
6.2.1	Thin films growth method	76
6.2.2	Structural and magnetic properties variation upon Cobalt doping	77
6.3	Summary	82
7	Conclusions	85
A	Calculations of layer-dependent density of states of the $\text{Mn}_{3-x}\text{Co}_x\text{Ge}$ systems	89
B	Calculations of disordered $\text{Mn}_{3-x}\text{Co}_x\text{Ge}$ systems	97
	Bibliography	101

Publications	123
Acknowledgements	125
Curriculum Vitae	127
Eidesstattliche Erklärung	129

List of Figures

1.1	Comparison of the densities of states between Cu and Ni	3
1.2	Schematics of spin valve and magnetic tunnel junction structures	4
1.3	Origin of tunnelin magnetoresistance effect	7
1.4	Structure of Toggle MRAM and STT-MRAM cells	10
1.5	Schematic of the reading and writing operation in a perpendicular STT-MRAM cell	12
2.1	Periodic table of elements	18
2.2	Structure schematics of half-Heusler, regular-Heusler and inverse-Heusler cubic unit cells	20
2.3	Relationship between inverse and regular cubic Heusler structures and their corresponding tetragonal structure	22
2.4	Probability of tetragonal distortion of cubic Heusler systems	23
2.5	Magnetization behavior for single crystal Iron, Cobalt and Nickel	25
2.6	Tetragonal unit cell of $D0_{22}$ - Mn_3Ge	26
3.1	Thin films deposition system of the 'Spintronics and Magnetoelectronics' lab at IBM Almaden Research	32
3.2	'G-system' chamber interior	35
3.3	Schematic of a Kaufman ion source	37
4.1	$L1_2$ - $IrMn_3$ unit cell	42
4.2	Reactive sputtering of $Ta_{1-x}N_x$ seed layers	44
4.3	(001)-textured TI buffer layers	45
4.4	Inter-mixing between $IrMn_3$ and Mn_3Ge layers	46
4.5	TaN inter-diffusion barrier	47
4.6	bcc -Cr unit cell	48
4.7	Schematics of substrates and buffer layers used	50
5.1	$Mn_{3+x}Ge$ films composition dependence	52
5.2	M vs. H hysteresis at RT of a Mn_3Ge film grown at 450 °C	54

5.3	Structural and topographical properties of Mn_3Ge films deposited using different growth conditions on TI buffer layers	56
5.4	Thickness dependence of Mn_3Ge Heusler films with giant PMA . . .	57
5.5	Schematics of MTJ stacks	59
5.6	Characteristics of Mn_3Ge -based MTJ devices	61
5.7	Mn_3Ge bands structure along the Γ -Z line	62
5.8	Schematics of the Brillouin zone filtering effect in MTJs	64
5.9	Layer-resolved bulk- Mn_3Ge density of states	64
5.10	TMR theoretical predictions for a $\text{Mn}_3\text{Ge}/\text{MgO}/\text{Fe}$ MTJ	65
6.1	Crystal structure schematics for different Co contents	72
6.2	$\text{Mn}_{3-x}\text{Co}_x\text{Ge}$ bands structure along the Z- Γ line	75
6.3	Influence of Co doping on the films structure	77
6.4	Influence of Co doping on the films magnetization	79
6.5	Comparison of the $\text{Mn}_{3-x}\text{Co}_x\text{Ge}$ system magnetization between calculations and experiments	80
6.6	Influence of Co doping on the films coercivity, effective field, and roughness	82
A.1	Layer-dependent DOS of Mn_3Ge	90
A.2	Layer-dependent DOS of $\text{Mn}_{2.75}\text{Co}_{0.25}\text{Ge}$	91
A.3	Layer-dependent DOS of $\text{Mn}_{2.5}\text{Co}_{0.5}\text{Ge}$	92
A.4	Layer-dependent DOS of Mn_2CoGe	93
A.5	Layer-dependent DOS of $\text{Mn}_{1.5}\text{Co}_{1.5}\text{Ge}$	94
A.6	Layer-dependent DOS of MnCo_2Ge	95

List of Tables

6.1	Structural and magnetic evolution of the $\text{Mn}_{3-x}\text{Co}_x\text{Ge}$ system	71
6.2	Layer-dependent bulk spin polarization of the $\text{Mn}_{3-x}\text{Co}_x\text{Ge}$ compounds	74
B.1	Energy configuration and magnetic moment of a <i>disordered</i> $\text{Mn}_{2.5}\text{Co}_{0.5}\text{Ge}$ system	98
B.2	Energy configuration and magnetic moment of a <i>disordered</i> Mn_2CoGe system	99

Abbreviations

AFM	AntiFerro-Magnetic
AP	Anti-Parallel
<i>bcc</i>	Body-Centered Cubic
BZ	Brillouin Zone
BZF	Brillouin Zone Filtering
DC	Direct Current
DOS	Density Of States
EELS	Electron Energy Loss Spectroscopy
E_F	Fermi Energy
<i>fcc</i>	Face-Centered Cubic
FiM	Ferri-Magnetic
FM	Ferro-Magnetic
<i>hcp</i>	Hexagonal Close Packed
HRTEM	High Resolution Transmission Electron Microscopy
IBD	Ion Beam Deposition
IMA	In-plane Magnetic Anisotropy
MC	MgO/Cr
MRAM	Magnetic Random Access Memory
MTJ	Magnetic Tunnel Junction
NM	Non-Magnetic

O	Octahedrally-coordinated
P	Parallel
SP	Spin Polarization
PLD	Pulsed Laser Deposition
PMA	Perpendicular Magnetic Anisotropy
PVD	Physical Vapor Deposition
RA	Resistance-Area
RBS	Rutherford Backscattering Spectrometry
RF	Radio Frequency
RT	Room Temperature
SQUID	Superconductive Quantum Interference Device
STT	Spin Transfer Torque
T	Tetrahedrally-coordinated
TD	Tetragonal Distortion or Tetragonally-Distorted
TI	TaN/ IrMn ₃
TIT	TaN/ IrMn ₃ / TaN
TMR	Tunneling MagnetoResistance
TSD	Target-Substrate Distance
UHV	Ultra-High Vacuum
VSM	Vibrating Sample Magnetometer
XRD	X-ray Diffraction

To Leonardo...

Chapter 1

Introduction

1.1 General introduction

“All the known magnetic properties of matter are attributable to the rotation of electric charges” [1]. Electrons are elementary particles, each having finite mass and charge. As Fermi particle, the electron also possesses another intrinsic property referred to as spin angular momentum or just spin. Due to its orbital motion about the nucleus, each electron is also associated with an orbital angular momentum. Spin and orbital angular momenta are quantized and can, in some atomic systems, be coupled via spin-orbit interactions.

The spin is a purely quantum-mechanical quantity representing a measure of the quantized angular momentum, $s = \frac{1}{2}\hbar$, of the nucleus and surrounding electrons (\hbar is the reduced Planck’s constant). The nuclear contribution of angular momentum to the atomic magnetic moment is very small due to the much larger mass of the nucleus with respect to the electron mass. In practice, nuclear magnetism is usually

negligible, and electrons contribute for the biggest part to the magnetic moment of solid-state matter.

The electron spin is associated with an intrinsic dipole magnetic moment that takes a value very close to the universal Bohr magneton constant, $1 \mu_B = \frac{e\hbar}{2m_e} = 9.27 \times 10^{-24} \text{Am}^2$ (e and m_e are the electron charge and mass respectively), and can only adopt one of two possible orientations with respect to an external magnetic field. The component along any axis (here chosen to be z) of this dipole moment can be written as:

$$m_z = -\frac{e}{m_e} \hbar m_s$$

, with $m_s = \pm \frac{1}{2}$ being the spin quantum number. Therefore, in a naive picture, the spin can be thought as an infinitesimal magnet pointing either up (spin up or \uparrow) or down (spin down or \downarrow) depending on the direction of the applied magnetic field (the magnetic dipole minimizes its energy by aligning in the same direction of the magnetic field).

Generally, in non-magnetic (NM) transition metals like Cu or Ag, \uparrow and \downarrow electrons are completely balanced in the absence of a magnetic field, as they equally populate the atomic energy levels. On the other hand, in ferromagnetic (FM) elements such as Fe, Co, Ni, and in FM alloys formed from combinations of these elements, the up and down spins are not balanced even at equilibrium due to strong exchange interactions which favor the parallel alignment of the spins. As a consequence, up and down spin channels are not equally populated, giving rise to asymmetric electron density of states at the Fermi energy (E_F) (as shown in Fig. 1.1b for Ni), resulting into strong spin-dependent scattering probabilities [2]. Therefore, when an unpolarized (same number of \uparrow and \downarrow) charge current is flowed into a FM system, the mean-free path between scattering events for spin up and down electrons is different, thus the two spin channels exhibit different conductivities. Hence, the

flowing current becomes spin-polarized (it would remain unpolarized if flowing through a NM material instead). This mechanism, whose fundamental principle relies on the intrinsic property of spin angular momentum of the electron, is at the basis of the science called spin-electronics or spintronics.

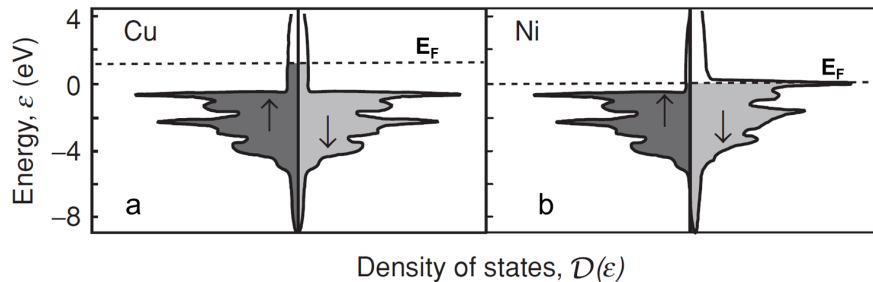


FIGURE 1.1: Density of states of bulk (a) Cu and (b) Ni. Reprinted from [3] with permission of Cambridge University Press.

As a complementary discipline of conventional charge-based electronics, in which the charge of the electron is the sole degree of freedom, spintronics exploits the angular momentum of the electron to store and read the information. This branch of solid-state physics revolutionized standard microelectronics devices by adding quantum-mechanical spin-dependent phenomena that originate from the interaction of the carrier spin and the magnetic properties of the material [4].

The discovery of the giant magnetoresistance (GMR) effect in the late 1980s [5, 6] using a spin-valve structure (Fig. 1.2a) and, in the following decade, of a large tunneling magnetoresistance (TMR) effect [7] at room temperature (RT) in magnetic tunnel junction (MTJ) structures [8, 9] (Fig. 1.2b) showed that it is possible to neatly control the charge transport in magnetic nanostructures through the magnetization of the materials. The ability to create, manipulate and detect spin-polarized currents using the spin of the electron allowed the development of novel devices with improved properties with respect to standard charge-based

semiconductor devices, especially in the field of magnetic recording such as hard-disk drives and magnetic random access memory (MRAM). Such properties include inherent non-volatility, decreased power consumption, and increased data storage and processing speed.

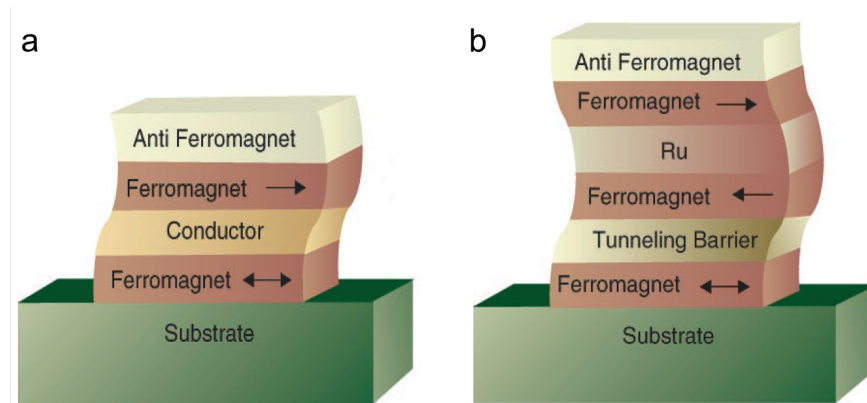


FIGURE 1.2: Schematics of (a) spin valve and (b) magnetic tunnel junction structures. The ferromagnets depicted with double (single) arrow are the free (fixed) electrodes. Image from [4]. Reprinted with permission from AAAS.

Following the publications of 1995 [8, 9] and up to this date, an extensive amount of research has been conducted throughout the world in order to make MRAM possible. The fundamental principles and potentials of this magnetic solid state memory make it a possible candidate for becoming a 'universal memory' that can be used for a wide variety of technological applications, from data storage in computers, smartcards, and mobiles to automotive, military, and space applications [2, 10].

The primary goal of the research presented in this dissertation was to identify and develop novel magnetic materials among the family of tetragonally-distorted Heusler compounds displaying large perpendicular magnetic anisotropy (PMA) for perpendicularly-magnetized magnetic tunnel junctions (p-MTJs) suitable for next-generation MRAM applications. General descriptions of MTJs, the TMR effect,

and the two main different generations of MRAM are presented later on in this chapter. Chapter 2 is devoted to a general description of Heusler compounds, with a major focus on Heuslers forming with a tetragonal crystallographic structure. The peculiar properties associated to some of these tetragonal compounds, like the PMA, are presented explaining why such materials could be used for p-MTJ devices.

The deposition system and techniques used for the growth of the thin films characterized in this work are described in Chapter 3. While Chapter 4 deals with the development and optimization of appropriate buffer layers for the growth of tetragonal Heusler alloys on amorphous Si/SiO₂ substrates, Chapter 5 summarizes the results obtained from the study of structural, topographical, and magnetic properties of tetragonal Mn₃Ge Heusler thin films, as well as transport characteristics and TMR of Mn₃Ge-based perpendicular tunnel junction devices developed in this work. A possible explanation is addressed for the compensated tunneling magnetoresistance effect found from measurements of these devices. This explanation is supported by theoretical calculations of transmission functions of similar MTJ structures and the influence on the TMR of the Brillouin zone filtering effect that arises at the interface between Mn₃Ge and the MgO tunnel barrier.

In Chapter 6, the evolution of the structural and magnetic properties of a Mn_{3-x}Co_xGe system are compared between theoretical and experimental studies. Furthermore, theoretical investigations of the layer-dependent electronic properties of the Mn_{3-x}Co_xGe system and the influence of Co on both the Brillouin zone filtering effect and spin polarization associated to each compound for different x concentrations are presented. Finally, Chapter 7 provides a conclusive summary of this dissertation and some comments from the author.

1.2 Magnetic tunnel junctions and tunneling magnetoresistance effect

The NM metallic spacer of a spin-valve structure was replaced by a thin (10-20 Å) NM *insulating* spacer, thus creating a magnetic tunnel junction [2] (see Fig. 1.2). A typical MTJ structure consists of two ferromagnetic electrodes - a reference (or pinned or fixed) electrode and a recording (or free) electrode - sandwiching a thin tunnel barrier, as shown in Fig. 1.2b. The orientation of the fixed electrode does not change and sets the spin-polarization direction, while the recording layer is 'free' to alternate its magnetic orientation so as to store the information.

Originally, different oxide materials have been tested as insulating spacer [11, 12, 13], with amorphous aluminum oxide (Al_2O_3) barriers displaying better tunneling magnetoresistance properties [14, 15]. However, thanks to theoretical predictions of giant TMR for a Fe/MgO/Fe system [16, 17], recently developed MTJs are formed using a thin crystalline insulating magnesium oxide (MgO) tunnel barrier [18, 19, 20, 21, 22, 23, 24].

Under a bias voltage applied across MgO, electrons quantum-mechanically tunnel from one electrode through the barrier to the second electrode. The probability of the tunneling is determined by the relative orientation of the magnetization of the two electrodes: if the two electrodes' magnetizations point along the same direction, i.e. they are aligned parallel (P) to each other, then the tunneling current typically flows more easily across the spacer, leading to a low-state of tunneling resistance R_P (Fig. 1.3a); on the other hand, if the magnetization of the electrodes are anti-parallel (AP) aligned, the probability of tunneling of the spin-polarized electrons is reduced, giving rise to a high-resistance state, R_{AP} (Fig. 1.3b). Hence, in order to set the state of the magnetic bit to a '1' or to a '0', one

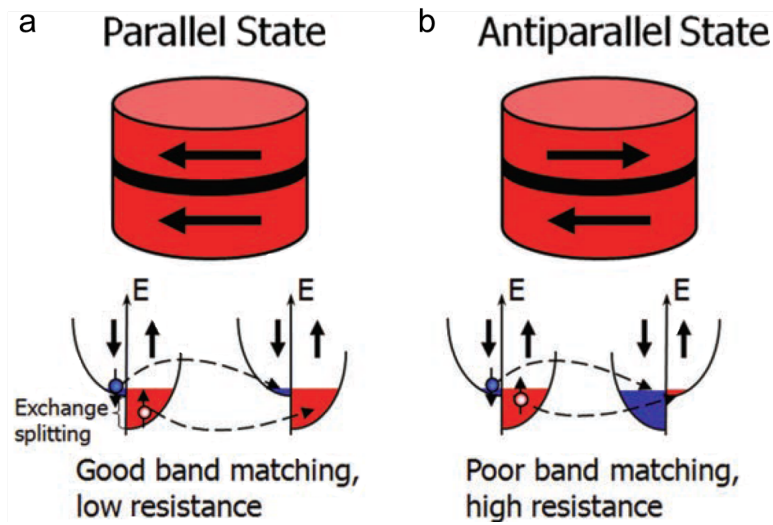


FIGURE 1.3: Assuming that the electron spin is conserved during tunneling, electrons from one electrode with a certain spin orientation can tunnel to the other electrode only if the latter has available empty states corresponding to the same spin orientation. Image from [25]. Reprinted by permission from ACM.

needs to switch the electrodes' magnetic orientation from P to AP or from AP to P, thereby changing the tunneling resistance from low to high or from high to low (assuming that the FM electrodes have positive spin polarization). The magnitude of the tunneling magnetoresistance is quantified using the formula $TMR = (R_{AP} - R_P)/R_P$: the higher the TMR, the higher is the difference in the two resistance states, the better is the reading performance of the memory element. The process of reading a '0' or '1' bit is achieved by simply detecting the current flowing through the MTJ device at small bias voltages or by detecting the voltage across the device when a small current is flowed through the device. On the other hand, the writing operation can be carried out using two different techniques: either using an external magnetic field or directly flowing a larger current (compared to the current used for reading) through the junction by exploiting the mechanism of spin transfer torque. These two techniques are presented later in more details.

1.2.1 Symmetry spin filtering effect

Julliere associated the TMR to the electrodes' tunneling spin polarization (SP), i.e. the ratio between the difference of spin up and spin down electron density of states (DOS) at the Fermi energy over their sum, $SP = (\text{DOS}_\uparrow - \text{DOS}_\downarrow) / (\text{DOS}_\uparrow + \text{DOS}_\downarrow)$ [7]. The TMR was then defined also as $\text{TMR} = 2 SP_1 \cdot SP_2 / (1 - SP_1 \cdot SP_2)$, where SP_1 and SP_2 are the spin polarization of the first and second electrode, respectively. Following Julliere's paper, several tunneling conductance studies of different metal-insulator systems have been investigated in order to understand the underlying physics behind such junctions.

Presumably one of the most revolutionary discoveries in the history of MTJs, the epitaxial Fe(001)/MgO(001)/Fe(001) system was predicted to show giant TMR ratios [16, 17]. In this system, the MgO(001) spacer focuses the transmission function into the Γ -point (i.e. $k_{\parallel} = 0$) of the k_{\parallel} plane of the two-dimensional (2D) Brillouin zone (BZ), since in bulk MgO the evanescent state with $k_{\parallel} = 0$ has the smallest attenuation constant for energies within the MgO band gap. This state has Δ_1 symmetry (it is invariant with respect to the square-group symmetry transformations of x and y coordinates) and mostly consist of a mixture of $m = 0$ orbitals: s-orbitals of Mg and p_z -orbitals of O (m is the projection of the angular momentum along the z axis). The attenuation constant increases as the in-plane momentum k_{\parallel} increases. Therefore, as the MgO thickness increases the transmission functions are focused closer and closer to the Γ -point in the 2D BZ [16, 17].

Moreover, in bulk Fe the majority electrons have states with Δ_1 -symmetry at the Γ -H line (along the k_z -axis) in the BZ at E_F , therefore they can couple to the Δ_1 -symmetry evanescent state of MgO. On the other hand, minority Fe electrons do not have bands with Δ_1 -symmetry crossing the Γ -H line at E_F . Thus, due

to symmetry-mismatch considerations, minority Fe electrons with $k_{\parallel} = 0$ cannot couple to the Δ_1 -symmetry evanescent state of MgO: their contribution to the transmission at the Fe/MgO interface is then suppressed. This effect is called symmetry spin filtering [16, 17]. Furthermore, bulk Fe has a large positive SP. Both symmetry spin filtering and large SP of Fe contribute coherently to the increase of the TMR. Therefore, the TMR of a Fe/MgO/Fe MTJ is large and robust, with optimistic values exceeding 10,000% for a number of MgO layers greater than 8, as later shown in Fig. 5.10a of Chapter 5.

1.3 Magnetic Random Access Memory

Magnetic random access memory (MRAM) is one of the most promising emerging memory technologies today. One of the key properties of MRAM is the inherent non-volatility. This means that the state of the memory is maintained even when the power is switched off and removed from the memory [26]. Also, in contrast to hard-disk drives, there are no moving parts in MRAM. The operation of storing the information is restrained only to the back-and-forth rotation of the magnetization of the free layer of the MTJ, which acts as the core storing element for MRAM [27]. As long as the magnetic materials used to form the MTJ electrodes are robust and stable over time against both thermal perturbations and small magnetic fields, then the stored data are securely retained, hence providing virtually infinite endurance; additionally, neither transistors nor capacitors, like in static and dynamic random access memory architectures (SRAM and DRAM, respectively), are needed in MRAM to store the magnetic bits, allowing the MRAM design to be denser and cheaper.

In MRAM, stored data can be read by activating the only transistor connected in series to the MTJ device (see Fig. 1.4) and measuring the MTJ resistance. The time required to read the state of the bit cell depends on how large the difference in signal between the P and AP states of the MTJ is. Therefore, the higher the tunneling magnetoresistance the better the reading performance and the faster the memory.

1.3.1 Toggle-MRAM vs. STT-MRAM

In first-generation MRAM, the magnetic tunnel junctions are formed using magnetic materials with in-plane magnetization. Each MTJ device is located at the intersection between two conductive lines, namely the bit and word line placed respectively above and below each junction, as shown in Fig. 1.4a.

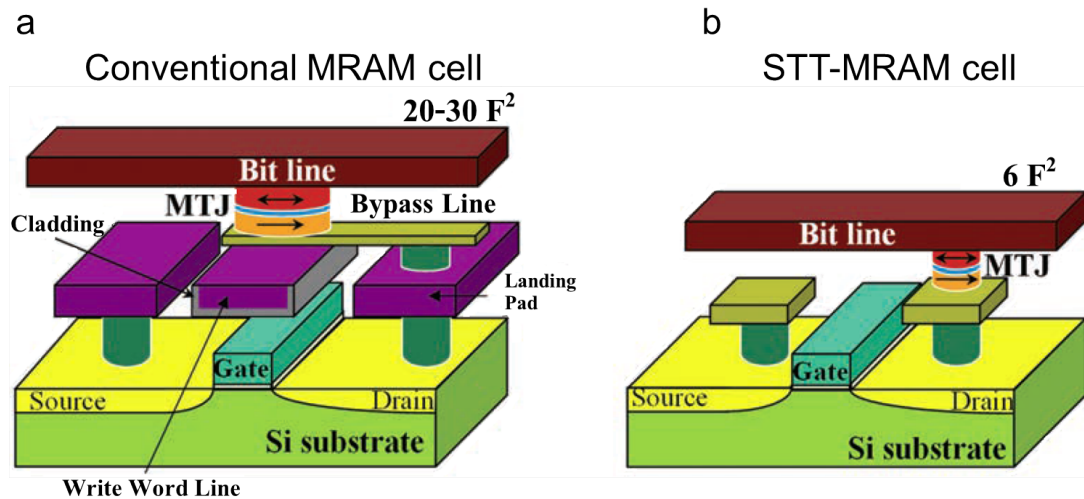


FIGURE 1.4: Structure of (a) conventional field-switched MRAM cell and (b) STT-MRAM cell. Image from [25]. Reprinted with permission from ACM.

Electric currents are driven through both the bit and word lines in order to activate one specific memory cell. These currents locally generate two Oersted magnetic

fields that, only when acting together, can induce a sufficient torque that rotates the free electrode magnetic orientation back and forth (by inverting the current polarity) with respect to the fixed electrode orientation: from this principle the name 'toggle'-MRAM was coined.

While only the selected MTJ cell experiences the contribution of both magnetic fields from the bit and word lines, all the other bit cells along the same bit line (or along the same word line) inevitably sense one magnetic field which can cause perturbations to the state of other MTJs. These latter bits are referred to as 'half-selected' bits [28, 29]. A key requirement of toggle-MRAM is to switch only the selected bit and not the half-selected ones. Thus, synthetic antiferromagnet (SAF) [30, 31] free layer structures with bit shapes 45°-rotated with respect to the metallic conductive lines and a specific sequence of current pulses are used in order to avoid any detrimental perturbation of the half-selected bits: this method is called the 'Savtchenko switching', as it was named after its inventor [29, 32, 33].

Toggle-MRAM chips have been in the market from 2006 (commercialized for the first time by Freescale Semiconductor) and have been used in critical aircraft and automotive applications. However, the market for this conventional MRAM did not significantly expand due to its high power consumption and limited scaling potential related to the utilization of magnetic fields as a mean to write the information [34].

After the discovery of the spin transfer torque (STT) [35, 36] - transfer of angular momentum from a spin-polarized current to the local magnetization of a FM conductor as a conservation of the total angular momentum - and the demonstration of current-induced switching of magnetic layers via STT [37, 38, 39, 40, 41], the magnetic Oersted fields were replaced by the STT as main mechanism to write the information in MRAM. Indeed, in STT-MRAM the bypass and word lines are

removed (see Fig. 1.4) and both reading and writing operations are simply carried out by passing a current directly through the selected cell. Therefore, compared to conventional MRAM, the design of STT-MRAM is much simpler and allows for reduced power consumption as well as improved scalability and storage density.

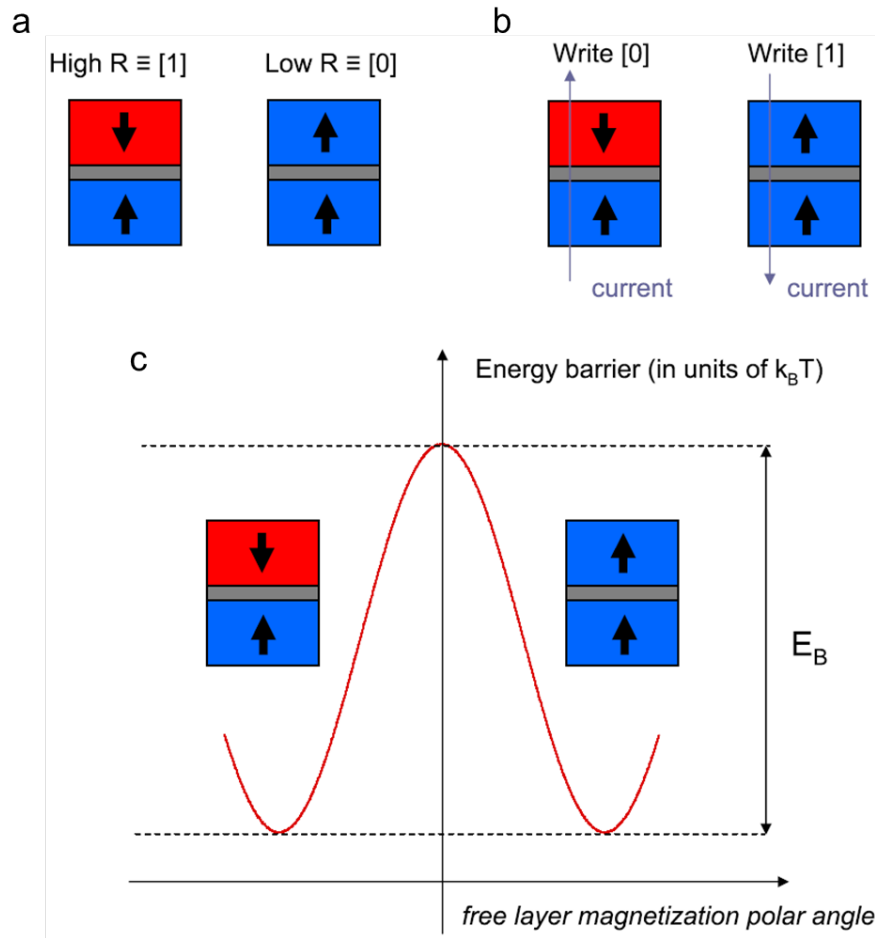


FIGURE 1.5: Schematic of (a) reading and (b) writing operations in a perpendicular STT-MRAM cell. The top layer represents the free layer, while the bottom one is the fixed layer. (c) Schematic of the energy barrier E_B that must be overcome to switch the free layer between AP and P states in a p-MTJ. Reprinted from [34], with the permission of AIP Publishing.

While small currents are used to read the MTJ state, larger currents can cause

excitations of the free electrode magnetization via STT and, above a critical current, the state of the MTJ can be changed. By reversing the current polarity, the MTJ state can be alternately set to a '0' or to a '1' as illustrated in Fig. 1.5b in the case of a p-MTJ. The writing current that is needed to switch the free layer is determined by the degree of spin polarization of the tunneling current, as well as by the efficiency of transfer of spin angular momentum from the tunneling current to the magnetization of the free layer that is characterized in large part by the 'damping' parameter, α . The smaller is the damping, the smaller is the writing current. Moreover, the writing current is influenced by the energy barrier (E_B) that must be overcome to switch the state of the MTJ (see Fig. 1.5c). In the simplest models of switching, the switching current is directly proportional to the magnitude of the energy barrier (for a given time for which the current is applied). Thus, there is an apparent conflict between the key requirements for high energy barriers that determine the lifetime of the storage element (discussed later in more details), and the need for low switching currents that necessitate low energy barriers.

STT-induced switching of in-plane MTJs has been studied [42, 43] and successfully observed [44, 45, 46]. Also, the functionality of in-plane STT-MRAM chips has been demonstrated since 2005 by Sony [47], followed in the years by Hitachi, Grandis, TSMC and Qualcomm [48, 49, 50], with the latest realization of a fully functional 64Mb in-plane STT-MRAM chip presented by Everspin Technologies [51].

However, a major problem associated with scaling to smaller dimensions of in-plane STT-MRAM cells is the superparamagnetic limit, whereby the magnetic anisotropy, that allows the free layer of the MTJ device to be set to the P or AP state, is not sufficiently large to stabilize the device against thermal fluctuations. Due to the small volume anisotropy of in-plane magnetic materials, the stability of

these cells depends significantly on the devices' needle-shape that provides modest shape-anisotropy effects.

Higher thermal stability can be achieved by using MTJs that display large PMA, wherein the moments of the free and reference layers are oriented perpendicular to the plane of the films (Fig. 1.5). Since a typical requirement is that a MTJ memory element must reliably store a data bit for a minimum period of ten years, this necessitates that $E_B \geq 50 k_B T$ [52, 53], where $E_B = K_U \cdot V$, and $K_U = H_K \cdot \frac{M_S}{2} + 2\pi M_S^2$ is the uniaxial magnetic anisotropy energy density. k_B is the Boltzmann constant, T is the temperature, V and M_S are the volume and the spontaneous magnetization of the free layer respectively, and H_K is its effective anisotropy field. Thus, free layers with sufficiently high anisotropy energies are needed. This can be readily accomplished with perpendicularly magnetized materials.

Moreover, the perpendicular magnetic anisotropy partially counteracts the contribution of the large out-of-plane demagnetizing field of the free layer that increases the switching current density [43, 54, 55]. Thus, the current that is needed to switch the state of an MTJ is lower for a p-MTJ than for an in-plane magnetized MTJ having the same barrier [25, 56, 57, 58]. The critical current density for a p-MTJ is given by the following formula:

$$J_{c0} = \frac{1}{\eta} \frac{2e\alpha}{\hbar} (M_S t) H_K$$

where η is the spin transfer efficiency, α is the damping constant, e is the electron charge, \hbar is the reduced Planck constant, M_S and t are respectively the free layer spontaneous magnetization and thickness, and H_K is the effective anisotropy field defined above through K_U . The critical current density increases the greater is the magnetic moment of the free layer: thus the smaller M_S the better. Alloys of Co, Fe, and B in the form of thin films and for different compositions have

been reported to display PMA, promoted by anisotropy effects originating at the interface between the CoFeB layer and a underlayer or overlayer [59, 60]. This PMA, which decreases in magnitude with the thickness of CoFeB, might not be strong enough to sustain device sizes below a 20 nm node without degrading TMR and thermal stability properties of the p-MTJs: these conditions would not fulfill all the key requirements for technologically-relevant applications. Furthermore, the M_s value of CoFeB films is quite significant, i.e. typically greater than 1000 emu/cc. Nevertheless, current-induced switching of p-MTJs using STT has been demonstrated [61] using both $L1_0$ [56, 62] and CoFeB electrodes [57, 58, 59, 63, 64], with a recent development of a STT-MRAM chip using CoFeB-based 50nm-wide p-MTJs showing high STT efficiency and data retention [34].

J_{c0} is also closely tied to damping within the free layer. The damping of the free layer depends both on the intrinsic damping of the material itself - a volume effect - but also on mechanisms such as spin pumping whereby spin currents can flow from the magnetic layer into neighboring layers, e.g. especially any metallic underlayer or overlayers. These latter effects, that are interfacial in nature, often can dominate the damping of thin magnetic layers. The volume damping term, often referred to as Gilbert damping, is typically higher the higher the spin-orbit coupling parameter which itself is typically higher the higher the atomic number. High PMA is often achieved from interfaces between ultra thin Co, Ni, and Fe magnetic layers and heavy 4d or 5d transition metal layers [41, 65, 66, 67], which exhibit high α and, consequently, higher switching currents.

Considering the properties of weak interface-driven PMA, high magnetization and/or high damping associated to the magnetic materials mentioned above which are being used nowadays, the main goal of this work was to find and develop novel magnetic materials displaying better properties altogether. The research presented in this thesis primarily focused on the investigation of Heusler compounds with

a tetragonal structure in the ground state. Some of these compounds, formed using light elements and showing low magnetic moment, are predicted to show giant PMA promoted directly by the 'broken' symmetry of the tetragonal structure and not by interface effects. These materials are potential candidates for next-generation perpendicular STT-MRAM.

Chapter 2

Heusler compounds

2.1 Introduction

The first Heusler compounds were discovered in 1903 by Friedrich Heusler. He found that the ternary alloys CuMnSn , Cu_2MnSn and Cu_2MnAl displayed FM properties, even though none of the constituting elements is itself FM. His pioneering results sparked an immense interest among the scientific community, especially chemists, physicists, and material scientists. After more than a century from Heusler's original discoveries, Heusler materials are still intensively investigated, with more than a thousand of different alloys reported as of today (Fig. 2.1).

A signature feature of Heusler compounds is the fact that their intrinsic electronic and magnetic properties can be theoretically predicted and, in some cases, experimentally controlled by altering their elemental composition, i.e. changing the number of electrons occupying the outermost atomic orbitals (valence electrons) [69]. Therefore, the task of scientists has been to develop specific Heusler alloys according to the kind of application they wanted to employ them for. In fact,

X₂YZ Heusler compounds

H 2.20																	He	
Li 0.98	Be 1.57											B 2.04	C 2.55	N 3.04	O 3.44	F 3.98	Ne	
Na 0.93	Mg 1.31											Al 1.61	Si 1.90	P 2.19	S 2.58	Cl 3.16	Ar	
K 0.82	Ca 1.00	Sc 1.36	Ti 1.54	V 1.63	Cr 1.66	Mn 1.55	Fe 1.83	Co 1.88	Ni 1.91	Cu 1.90	Zn 1.65	Ga 1.81	Ge 2.01	As 2.18	Se 2.55	Br 2.96	Kr 3.00	
Rb 0.82	Sr 0.95	Y 1.22	Zr 1.33	Nb 1.60	Mo 2.16	Tc 1.90	Ru 2.20	Rh 2.28	Pd 2.20	Ag 1.93	Cd 1.69	In 1.78	Sn 1.96	Sb 2.05	Te 2.10	I 2.66	Xe 2.60	
Cs 0.79	Ba 0.89			Hf 1.30	Ta 1.50	W 1.70	Re 1.90	Os 2.20	Ir 2.20	Pt 2.20	Au 2.40	Hg 1.90	Tl 1.80	Pb 1.80	Bi 1.90	Po 2.00	At 2.20	Rn
Fr 0.70	Ra 0.90																	
		La 1.10	Ce 1.12	Pr 1.13	Nd 1.14	Pm 1.13	Sm 1.17	Eu 1.20	Gd 1.20	Tb 1.10	Dy 1.22	Ho 1.23	Er 1.24	Tm 1.25	Yb 1.10	Lu 1.27		
		Ac 1.10	Th 1.30	Pa 1.50	U 1.70	Np 1.30	Pu 1.28	Am 1.13	Cm 1.28	Bk 1.30	Cf 1.30	Es 1.30	Fm 1.30	Md 1.30	No 1.30	Lr 1.30		

FIGURE 2.1: Periodic table of elements: colors indicate the possible combinations of X,Y and Z elements that can be used to form many distinct Heusler alloys. Reprinted from [68], Copyright 2011, with permission from Elsevier.

this class of materials covers an impressive wide range of scientific applications. Their multi-functionality has been established with the significant discoveries of topological insulators [70, 71], semiconductors [72, 73, 74, 75, 76], superconductors [77, 78, 79], thermoelectric materials [80] and, among the family of magnetic materials, ferri-magnetic non-collinear magnets [81], magneto-optical [82] and magneto-caloric [83] materials, and exchange-bias compensated ferri-magnetic systems [84].

The impact on spintronics has also been remarkable [69]. The prediction [85] and observation [86] of half-metallicity amid cubic Co₂-based alloys at RT triggered great attention among many semiconductor industries. Half-metallic ferromagnets exhibit a metallic behavior for electrons of one spin orientation, while they are insulating for electrons with the opposite spin orientation. This means that a current flowing through such material would be fully spin-polarized. The control of such current that ideally carries only one "orientation" of spin angular momentum can enable scientists to take full advantage of various spintronic devices such as,

for instance, MTJs for highly-dense STT-MRAM. In an ideal case, the utilization of half-metallic magnetic electrodes should lead to no current flow for one magnetic state, so that infinite TMR values would be possible.

Furthermore, the discovery of high perpendicular uniaxial magnetic anisotropy within tetragonal Mn_3 -based Heusler materials [87, 88] has also affirmed the potentiality of Heusler compounds for STT-MRAM as well as rare-earth-free permanent magnets, magnetic sensors, high-frequency STT-oscillators, and current-perpendicular-to-plane giant magnetoresistance (CPP-GMR) devices as read-head sensors for hard disk drives [89].

2.2 Cubic compounds

Two distinct classes of Heusler materials are known depending on the number of primitive sublattices that form the cubic unit cell. Compounds formed by three face-centered cubic (*fcc*) sublattices that interpenetrate one another are referred to as Half-Heusler compounds, while four interpenetrating *fcc* sublattices define the full-Heusler compounds, or simply Heusler [68].

Half-Heuslers are represented with the formula XYZ, in which the X and Z atoms are, respectively, the most electropositive and electronegative elements. X and Y atoms can be from a main group, or transition metal elements (X can also be a rare-earth element), whereas Z is a main group element. Given the odd number of interpenetrating sublattices, half-Heuslers crystallize in a non-centrosymmetric $C1_b$ structure, with space group 216, in which each of the constituting element's atoms define one atomic sublattice (Fig. 2.2a). The prototype of half-Heusler compounds is MgAgAs.

Slightly different is the case of full-Heusler alloys. These compounds are typically represented by the formula X_2YZ (I), or $XYX'Z$ (II) where X, X' and Y are transition metals or lanthanides and Z is from a main group metal. There exists two different Heusler structures: (I) denotes the 'regular' (or 'reg') structure (Cu_2MnAl , with $L2_1$ structure, is the prototype and space group 225), within which the X atoms are located at the same layer and occupying the two tetrahedrally-coordinated unit cell sites (Fig. 2.2b). On the other hand, (II) represents the 'inverse' (or 'inv') structure (CuHg_2Ti , with X_a -type structure, is the prototype and space group 216) with X and X' (atoms from the same element) sitting not at the same layer but at two adjacent layers, i.e. one atom at a tetrahedrally-coordinated site and the other one at an octahedrally-coordinated site (Fig. 2.2c) [68].

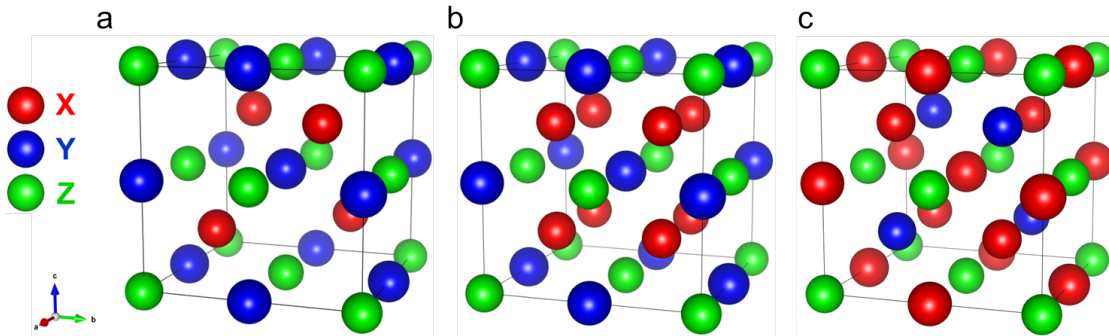


FIGURE 2.2: Schematics of (a) half-Heusler, (b) reg-Heusler, and (c) inv-Heusler cubic crystal structures.

Within the family of magnetic Heusler compounds, the X and Y atoms or, for some cases [90], the X and X' atoms are responsible for the magnetism character of the compound. The nature of exchange interaction between adjacent layer atoms, together with the magnitude of their corresponding magnetic moments, determine the formation of ferromagnetic, ferrimagnetic (FiM) or completely compensated systems, as theoretically predicted for some Mn-based Heusler materials [91].

2.3 Tetragonal compounds

Besides the cubic family of Heusler compounds, there exists a sub-family of Heuslers whose unit cell undergoes to a tetragonal distortion (TD) along one of the crystal axes in order to minimize its internal energy configuration. The tetragonal unit cell can be derived from the cubic one by means of a 45° in-plane rotation of the cell edges and an elongation along the c axis, as illustrated in Fig. 2.3. Compared to the cubic configuration, the TD unit cell has a shrunk in-plane a_{tet} lattice constant, with $a_{cub} = \sqrt{2} a_{tet}$, and a stretched out-of-plane c_{tet} lattice constant, with $[c_{tet} / (\sqrt{2} a_{tet})] > 1$. As illustrated in Fig. 2.3, Mn_2NiSn and Ni_2MnSn are the prototypes for the inverse tetragonal and regular tetragonal Heusler crystal structures, respectively.

2.3.1 Origin of tetragonal distortion

The change of the cubic structure of some Heusler compounds into a TD structure is a consequence of the crystal energy minimization due to its unstable cubic configuration. It is generally believed [92, 93] that such distortion is associated to the high DOS peaks near E_F , $DOS(cub, E_F)$, in the cubic phase. The higher the $DOS(cub, E_F)$ the higher the probability of tetragonal distortion, as shown in Fig. 2.4.

The study of the DOS of cubic and tetragonal phases of many compounds [94] has shown that the mechanism behind the tetragonal distortion is related to the peak-and-valley character of some cubic systems' DOS (arising from localized d -bands and van Hove singularities [95]) in conjunction with a smooth shift of majority and/or minority DOS structures close to E_F when valence electrons are added

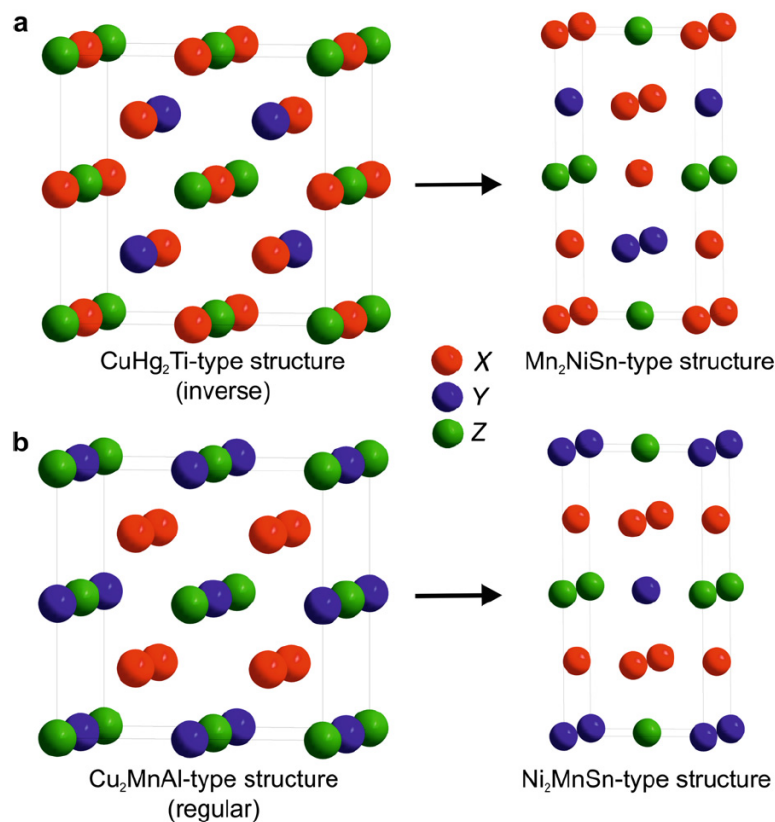


FIGURE 2.3: Schematic comparison between (a) inverse cubic Heusler and its corresponding tetragonal unit cell, and (b) regular cubic Heusler and its corresponding tetragonal unit cell. Reprinted from [68], Copyright 2011, with permission from Elsevier.

into each system, leading to an alternation between stable and unstable cubic phases [94].

When E_F is found in the middle of a DOS peak (i.e. unstable energy configuration) in the cubic structure, the crystal energy could be lowered by undergoing a TD. This effect can take place for the following reasons. Firstly, a cubic system is characterized by many points, lines and surfaces in the Brillouin zone (BZ) that are equivalent by symmetry considerations. The energy of equivalent k-points' bands corresponding to these points/lines/surfaces is the same, leading to peaky structures of DOS. After a structural distortion, the symmetry of the system decreases

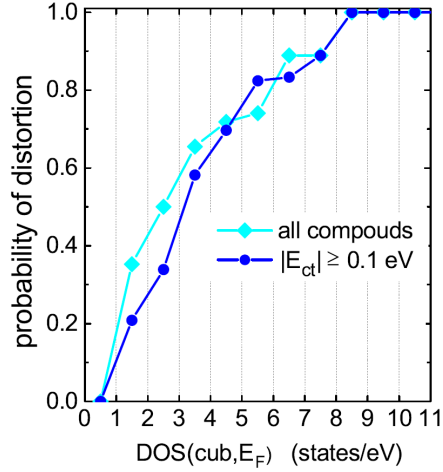


FIGURE 2.4: Probability of tetragonal distortion depending on the number of DOS at E_F in the cubic phase. The data are collected from [94]. Cyan points correspond to all the 286 Heusler compounds studied in [94], while blue points refer to the 220 compounds found to be stable in the tetragonal phase, i.e. $|E_{ct}| \geq 0.1$ eV. E_{ct} is defined as the difference between the total energy of the cubic phase (E_c) and the total energy of the corresponding tetragonal phase (E_t) for each Heusler compound, $E_{ct} = E_c - E_t$. Reprinted with permission from [94] Copyright (2017) by the American Physical Society.

and the energies of the k-points that were equivalent in the cubic system become non-equivalent in the TD system. Secondly, degenerated in the high-symmetry (cubic phase) k-points (e.g. Γ -point), partly occupied bands can split to different energies due to the lower symmetry (tetragonal phase) of the system (band Jahn-Teller effect [96, 97]). Thirdly, due to the TD, the width of the bands originating from orbitals which overlap in the direction of crystal contraction becomes broader [98]. All these three described effects result into a reduction (and/or shift away from E_F) of the DOS peaks and, in general, into more smoothly-distributed DOS, with lower values at E_F in the TD phase as compared to the cubic phase. As described above, the tetragonal crystal structure is characterized by two lattice constants instead of just one. This additional degree of freedom also helps to avoid energy-unfavorable DOS peaks at E_F . In reference [94], the changes in the DOS

configurations from the cubic to the tetragonal phase (the latter one only if existing) are shown for different Heusler compounds by adding one valence electron at a time into the system.

2.3.2 Perpendicular magnetocrystalline anisotropy arising from the tetragonal structure

In a ferromagnetic material, despite the energy contributions arising from *extrinsic* constraints, such as its shape, or interatomic effects induced at its interfaces with other FM or NM materials, there is another type of energy that causes the magnetization to align along specific crystallographic axes, the latter referred to as easy axes of magnetization. This energy, called magnetocrystalline anisotropy energy (MCA), derives from *intrinsic* properties of the material, i.e. the crystallographic configuration and the spin-orbit coupling effect [99], the latter usually being greater for heavier elements. In FM materials, the magnetization of the crystal 'sees' the lattice through the overlap of the electrons charge distributions among the atoms: each spin interacts with its orbital motion, by means of the spin-orbit coupling, and with the other spins in the crystal [100]. As a consequence, the magnetization process is different when the magnetic field is applied along different crystallographic directions, as shown in Fig. 2.5 for cubic Fe and Ni, and for hexagonal Co.

Generally, FM materials with a cubic crystal symmetry show weak anisotropy, since the sum of the magnetic dipolar interaction contributions from all the neighboring spin pairs in the crystal cancels out. Thus, thin films formed from any magnetic material with a cubic structure such as, for instance, transition metals like Fe and Ni, or binary and ternary cubic alloys like Co_xFe_y , or even cubic Heusler compounds, will show in-plane magnetic anisotropy (IMA), i.e. the atoms'

magnetic moments will lie along the plane of the film due to demagnetizing effects induced by shape anisotropy (assuming that the thickness of the film is much smaller than its lateral dimensions).

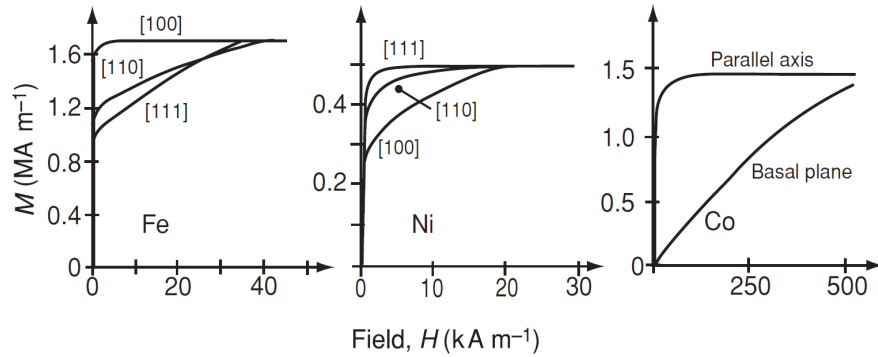


FIGURE 2.5: The magnetization curves of single crystals of the three 3d ferromagnetic elements, corrected for the demagnetizing field, show a different approach to saturation when magnetized in different crystallographic directions. Reprinted from [3] with permission of Cambridge University Press.

However, the situation is different for materials crystallizing with a 'broken'-symmetry structure, in which the sum of the magnetic dipolar interaction energies is not zero. These systems possess higher MCA. For instance, the anisotropy energy of hexagonal close packed (*hcp*) Co is of the form:

$$E = K_1 \sin^2 \theta + K_2 \sin^4 \theta$$

, where K_1 and K_2 are the first and second anisotropy constants (strongly temperature dependent), and θ is the angle between the magnetization M and the easy axis. In *hcp* Co the easy axis of magnetization is the axis perpendicular to the basal plane of the hexagonal lattice [101] (both K_1 and K_2 are positive): hence, *hcp*-Co displays PMA property.

The same considerations apply to FM alloys crystallizing with a tetragonal structure. Also in tetragonal FM alloys the easy axis of magnetization is along the

elongated axis of the crystal lattice. Tetragonal FeCo alloys with $c/a > 1$ were predicted [102] and demonstrated [103, 104] to show PMA.

Among the family of tetragonal Heusler materials, many Mn_2 -based compounds have been intensively investigated [87, 88, 93, 105, 106, 107, 108, 109, 110, 111, 112, 113, 114], some of which have been demonstrated to show good PMA properties. As an example of a typical Heusler tetragonal crystallographic configuration, the unit cell of $D0_{22}$ - Mn_3Ge is displayed in Fig. 2.6. Like for the case of *hcp*-Co, in Mn_3Ge the Mn spins align along the c out-of-plane easy axis of magnetization, thus giving rise to perpendicular magnetic anisotropy. Due to the high PMA as well as other properties that are discussed in the next section, some of these tetragonal Heusler compounds [115] are of significant interest for different spintronic applications such as STT-MRAM, permanent magnets and STT-oscillators, in which novel and rare-earth-free materials with very large PMA can be used to improve the performances and lessen the costs.

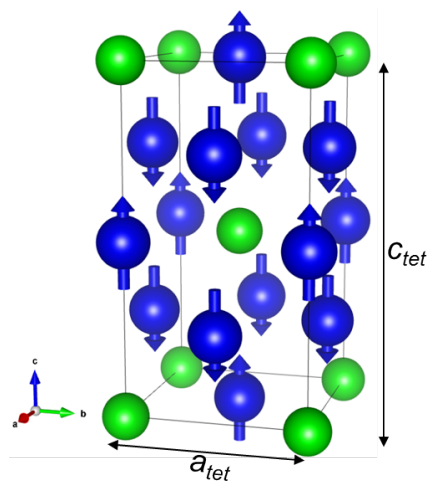


FIGURE 2.6: $D0_{22}$ -tetragonal unit cell of Mn_3Ge . The blue and green atoms correspond to Mn and Ge atoms, respectively.

2.3.3 Application of tetragonal Heuslers to STT-MRAM

To this date, MRAM is one of the most promising and emerging non-volatile type of memories. A key approach for the enhancement of its performances lies in the development of novel electrode materials for the MTJ memory components, possessing enough stability against thermal fluctuations so as to endure deeply scaled devices. The state of the art of magnetic materials used for MTJs mainly includes alloys formed with Co, Fe and B elements (with different compositions, usually B-poor). CoFeB films are utilized as magnetic electrodes and typically interfaced with an insulating tunnel barrier formed by MgO(001) thin layers [20, 59, 116]. In order to reduce the amount of current density required to switch the states of the MTJ between parallel and anti-parallel (and vice-versa) by transferring of angular momentum from a spin-polarized current [35, 36, 117], the magnetic electrodes must possess sufficient PMA [118, 119] so that their magnetization align perpendicular to the layers plane, thus counteracting the demagnetizing fields that would induce the magnetization of the electrodes to lie in the plane of the MTJ.

CoFeB thin layers show PMA due to effects originating at the *interface* between these layers and a MgO layer and/or a buffer layer onto which CoFeB is grown [59, 60, 120, 121]. In order to increase the memory storage density by shrinking the devices' size even below ~ 20 nm, the CoFeB layer has to be sufficiently thin such that (I) the interface-driven PMA can overcome the demagnetization energy that originates from (and increases with) the volume of the CoFeB thin film, and (II) to allow for diminished current densities by means of the STT. Therefore, new magnetic materials with large PMA arising from *volume* MCA are needed [87] for this type of memory application.

As mentioned in the previous section, some tetragonally-distorted Heusler compounds have been demonstrated to display this property. For instance, Mn_{3-x}Ga

and Mn_3Ge have been synthesized and developed in both bulk and thin film forms. The first Mn_3Ga bulk alloys were found back in 1970 by Kren and Kadar [105]. The authors reported that the hexagonal and antiferromagnetic (AFM) D0_{19} phase of Mn_3Ga transformed into a tetragonal D0_{22} FiM phase upon annealing of the sample at 750 K. In 2007, Balke and collaborators described the study of a stable D0_{22} - Mn_3Ga tetragonal structure and estimated the SP to be of 88% at E_F , from a theoretical study of the electronic structure [109]. More recently, tetragonal Mn_2 -based Heusler compounds were grown in the form of thin films: in 2011 Kurt and coworkers experimentally measured the spin polarization of FiM- Mn_3Ga films to be as high as 58% using point-contact Andreev reflection measurements. Mn_{3-x}Ga [88, 113, 122, 123] and Mn_3Ge [87, 111] were also shown to exhibit large PMA with coercive fields greater than 1 T. Furthermore, these Mn-based TD Heuslers were found to show a FiM configuration - with low values of spontaneous magnetization - due to an AFM coupling between the Mn magnetic moments located at two distinct layers in the unit cell. The combination of low magnetization, large PMA, and high bulk SP represent some of the important properties that are looked for in novel magnetic materials for the development of next-generation spin-transfer torque magnetic random access memories.

2.3.4 D0_{22} - Mn_3Ge

The ground state configuration of Mn_3Ge is the D0_{22} tetragonal phase with estimated lattice constants of $a_{tet} = 3.75 \text{ \AA}$ and $c_{tet} = 7.12 \text{ \AA}$ [108]. The out-of-plane c dimension is elongated with respect to the in-plane dimension, with $[c_{tet} / (\sqrt{2} a_{tet})]$ ratio of ~ 1.34 (see Fig. 2.6). D0_{22} - Mn_3Ge crystallizes in a layer-by-layer fashion, in which Mn-Mn atoms sit in one layer (at tetrahedrally-coordinated sites

by the Ge element) and Mn-Ge atoms sit on the adjacent layer (at octahedrally-coordinated sites by the Ge element). The broken symmetry induces the Mn atoms' magnetic moments to orient in the direction perpendicular to the ab plane, thus promoting large PMA.

The FiM character of Mn_3Ge arises from the overlap of the charge distributions of neighboring Mn atoms: the symmetry of the orbitals and their relative distance within the tetragonal unit cell favor a stronger hybridization of the d_{xy} , d_{yz} , d_{xz} localized orbitals of Mn atoms between adjacent layers, compared to same-layer (in-plane) orbital interactions. This leads to the formation of an AFM exchange coupling (in the out-of-plane direction) between Mn magnetic moments sitting on adjacent layers (nearest neighbor), and a FM exchange coupling between Mn moments sitting on the same layer (second nearest neighbor). The magnitude and sign of the Mn-Mn and Mn-Ge magnetic moments are different (presented in Chapter 6), giving rise to the FiM configuration with net magnetic moment of 1 Bohr magneton (equivalent to $M_S \sim 175$ emu/cc). This value is almost 6-7 times smaller than for cubic and FM Co-based Heusler compounds, like Co_2MnX ($X = \text{Si}$ and Ge) with $M_S \sim 1000$ emu/cc, as well as for CoFeB ($M_S \sim 1200$ emu/cc for a 20:60:20 composition). Note that one way to reduce the critical current needed to switch the MTJ between its two magnetic states using STT is to utilize recording layer materials with low M_S [35, 36].

The DOS (displayed later in Fig. 5.9) calculated from the electronic structure of bulk- Mn_3Ge showed that this compound possesses high negative spin polarization of $\sim -70\%$. Thus, in the case of the development of a magnetic tunnel junction formed with two Mn_3Ge electrodes sandwiching an amorphous insulating spacer could give rise to TMR values $> \sim -200\%$, according to Julliere's model [7].

Given its mentioned properties, TD-Mn₃Ge was considered to be of significant interest for the aim of this project and was identified as the first candidate to be investigated.

Chapter 3

Thin films deposition system

In this chapter, a brief overview of the IBM Almaden thin film deposition system is firstly presented. Then, a description of the sputtering chamber and deposition techniques used in this work for the growth of thin films are presented.

3.1 Multichamber, all-vacuumed deposition system

The multichamber, all-vacuumed thin film deposition system of the Spintronics and Magnetoelectronics group's lab at the IBM Research center of Almaden is depicted in Fig. 3.1. The entire system was designed at Almaden and assembled from 2003, when the first deposition chamber - a Pulsed Laser Deposition (PLD) chamber - was installed, to 2009 when the sputtering chamber was integrated. Referred to as the 'PLD-TEON', this system is composed by seven distinct chambers that are all interconnected through a middle robot chamber. Inside the latter, the robot arm automatically moves samples from one chamber to another one

without exposing the specimens to atmosphere pressure. In fact, all the chambers are under vacuum conditions (some of them actually reach ultra-high vacuum) to prevent any kind of contamination from ambient pressure during samples transfer.

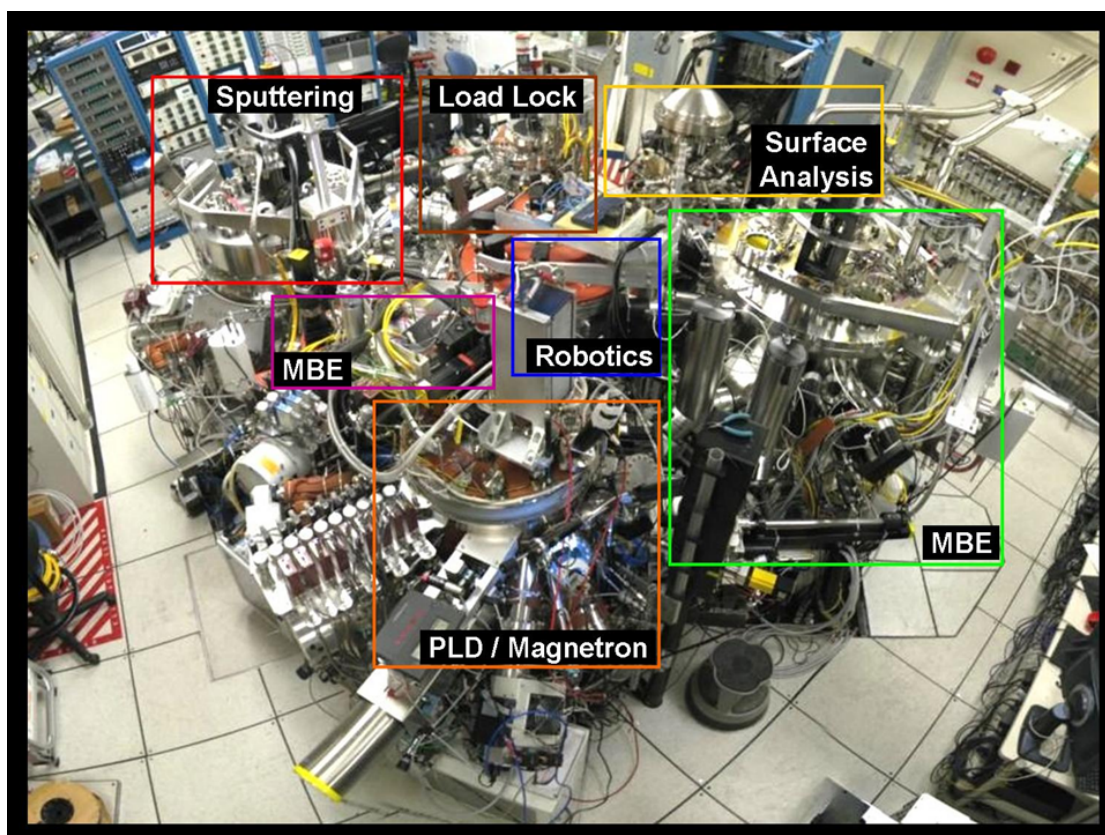


FIGURE 3.1: Picture of the seven chambers composing the thin films deposition system at the Spintronics lab at IBM Almaden.

Besides the PLD, sputtering, and robotics chambers, the PLD-TEON is equipped with two molecular beam epitaxy chambers, a surface analysis chamber with x-ray photoelectron spectroscopy and ultraviolet photoelectron spectroscopy capabilities, and a final loadlock in which up to 60 samples can be stored. The deposition technique of the four thin-film deposition chambers is based on the physical vapor deposition (PVD) method. All the samples that were prepared for this work were grown using the sputtering chamber which is described in the next section.

3.2 The "G-system"

Sputtering is a deposition technique that is vastly used in many different industries involved in, for example, semiconductors, automotive, medical, data storage, energy, and aerospace applications. Contrary to evaporation techniques, sputtering is faster and more versatile, allowing also for deposition of materials with high melting point [124].

Almaden's sputtering system, simply called the "G-system", is a custom-made PVD-based chamber developed at Almaden in 2009. The G-system has the capability of transferring samples in and out of the chamber (by sending the central robot arm through a main gate valve that connects the robot chamber with the sputtering chamber) without breaking the vacuum conditions, thus preventing any exposure to ambient pressure and allowing for a continuous and automatic deposition of new specimens. The G-system is generally opened only for maintenance and/or to change the material targets.

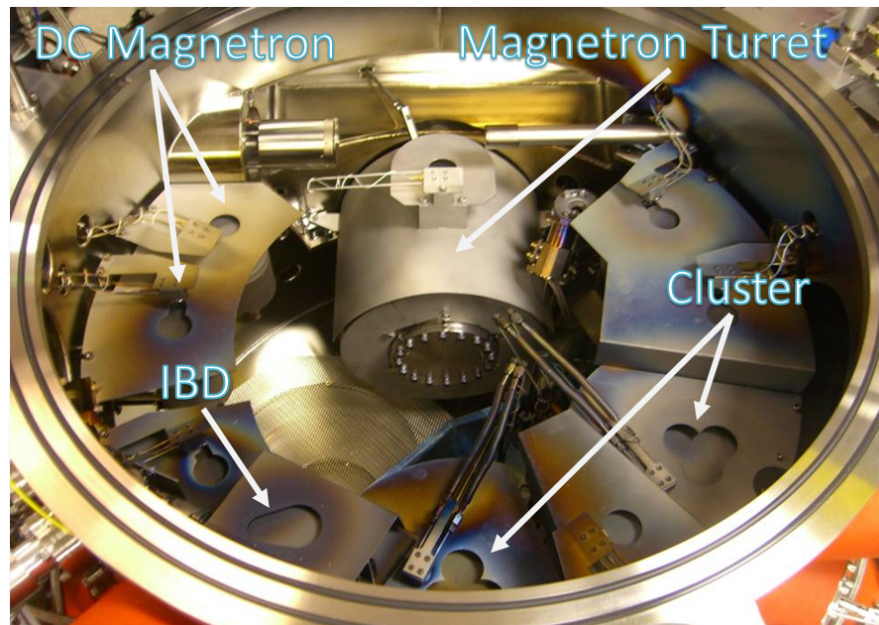
This chamber is equipped with three substrate stages, each of them having a doped-SiC heater providing heating to temperatures up to ~ 1200 °C, and being independently rotated during deposition to improve films uniformity. The chamber base pressure is $\sim 4 \times 10^{-10}$ Torr, which is of vital importance during *in-situ* annealing procedures to prevent any gas incorporation into the annealed films. Right below each substrate, shadow-masks with specific shapes and features can also be inserted to directly develop multi-layered devices without using any lithographic procedure. Both substrates and masks can be up to 1"-wide in diameter.

A total of 29 different material targets can be installed inside the G-system. The following is a list of the sputtering sources along with their corresponding number of available targets.

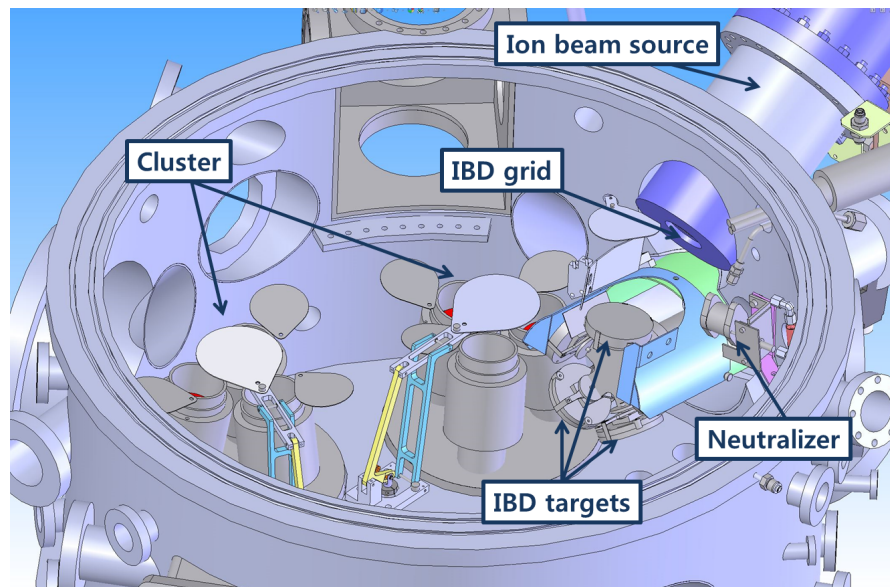
- Six individual 2" direct-current (DC) magnetron sources.
- Two 3-source 2" DC magnetron clusters or "triodes" (for co-sputtering with adjustable target-substrate distance, TSD).
- One 5-target 3" radio-frequency (RF) ion-beam source for ion-beam deposition (IBD).
- One rotating magnetron turret (DC or RF) with twelve individually selectable targets, with off-axis sputtering capability and adjustable TSD.

Note that the capabilities of adjusting the TSD and perform off-axis deposition are powerful tools for the variation and control of the chemical composition, and hence the properties, of the sputtered alloys particularly for the Heusler compounds. This feature along with the wide option of different material targets available makes the G-system a very powerful, versatile, and fully-automatic thin films deposition tool. The interior of the chamber is displayed in Fig. 3.2.

After maintenance and/or new targets insertion, the entire chamber is usually baked at 120 °C for at least 24 hours in order to degas all interior components and recover the base pressure. Then, the substrate holders are let to cool down to RT and calibration films, generally using 1"-Si (001) substrates covered with 250 Å of thermally-grown SiO₂, are grown using specially designed calibration masks used to quantify the film thickness and calibrate the deposition rates. The typical thickness used for the calibration films ranges between 300 to 500 Å, and it is measured using a profilometer. Moreover, the same wafers can be used to measure the film composition using Rutherford backscattering spectrometry (RBS), which additionally provides a measure of impurity concentrations (if any) and the thickness of the film based on the atomic density of the film elements.



(A) Real picture of the open chamber. Each sputtering source is hidden beneath its shield and shutter.



(B) CAD image. It is a $\sim 50^\circ$ counterclockwise rotated image of (A). Only the two magnetron clusters and the IBD are shown to improve picture clarity. The other guns and many other parts (e.g. top shields, neutralizer's RF power supply and gas lines) are hidden.

FIGURE 3.2: 'G-system' chamber interior

The magnetron modules used in the G-system are from the A300 AJA series, made with a large, plated Fe slug in the center with peripheral stacked NdFeB permanent magnets. The usual magnetron sputtering conditions involve the use of Argon (Ar) as the sputtering gas, kept at a constant pressure of 3 mTorr. However, gas mixtures of Ar, Oxygen (O₂) or Nitrogen (N₂) can be utilized in case of reactive sputtering. While the DC method is used for sputtering of conducting targets (NM, AFM or FM metals), RF sputtering is necessary for the growth of films from insulating targets such as, for instance, MgO. In fact, in the DC case, positive ions would accumulate at the surface of the insulating target, thus shielding and eventually stopping the sputtering of atoms off the target. In RF instead, the fast and alternating electromagnetic field prevents the formation and screening of these cations, allowing the target atoms to be knocked off it [124].

As previously mentioned, the G-system is also equipped with an IBD gun (RFICP 40 model from Kaufman & Robinson, Inc [125]). The latter is composed by an ion source that uses RF discharge to generate positive ions that are accelerated and focused as a beam (using a system of three Molybdenum grids, see Fig. 3.3) onto the selected material target. The gas used for the RF discharge is Krypton (other common discharge gases are Ar, O₂, and N₂). Also, an external neutralizer (see Fig. 3.2(B)) is utilized to generate many electrons whose function is to counterbalance the cations charge in order to prevent (I) beam divergence, caused by mutual scattering of these ions, and (II) positive ions accumulation onto the target [124]. The pressure used during IBD deposition is $\sim 10^{-4}$ Torr. Both metallic and insulating materials can be sputtered using this technique. The G-system's IBD has 5 individually-selectable targets assembled below the ion source outermost grid and next to the neutralizer, as shown in Fig. 3.2(B).

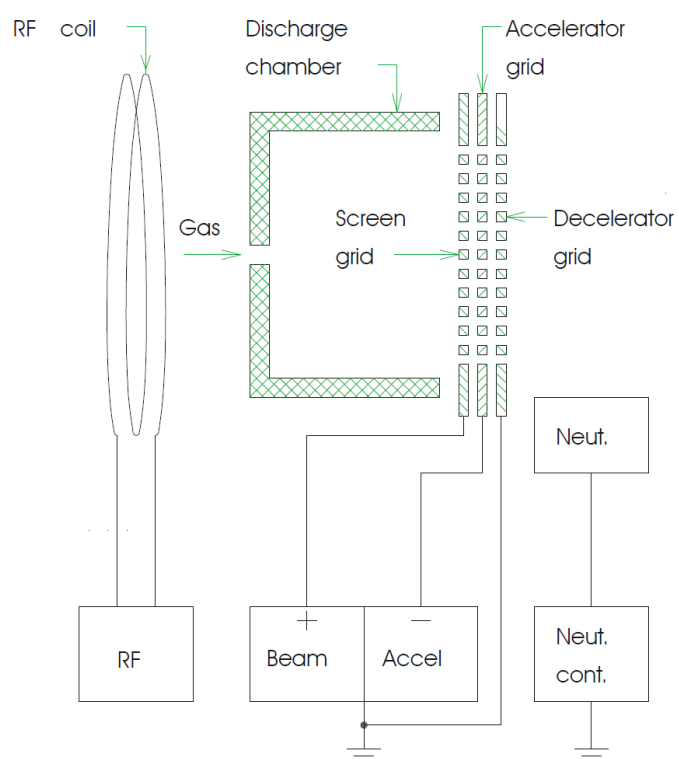


FIGURE 3.3: Schematics of a Kaufman ion source used for IBD [125].

Chapter 4

Buffer layers development and optimization

4.1 Introduction

Magnetic tunnel junctions are commonly formed by stacking of ultra-thin films of several different materials, generally on a silicon substrate. The films are grown in a layer-by-layer fashion, should be ideally defects-free, and forming with extremely smooth and abrupt interfaces between layers to ensure optimal MTJ devices performances. The choice of the type of underlayer material is of critical importance for the development of the magnetic electrodes and the tunneling barrier. Each underlayer must act as a template to promote the epitaxial growth of the overlayers with the desired crystal structure and crystallographic orientation. The formation of overlayers having undesired phases or misoriented film grains likely leads to detrimental MTJ properties.

Normally, few criteria can be followed for the appropriate selection of buffer layer materials. Firstly, crystallographic properties including the structure symmetry and the in-plane lattice dimensions must be taken into consideration for a suitable match with the overlayer material. By superimposing two materials having matching crystal symmetries, one is able to lessen the likelihood of defects and strain formation in the bilayer. This happens when atoms being deposited on a film uniformly cover its surface in a ordered manner, i.e. at energetically-favorable atomic sites and not at interstitial positions.

Also, the lattice mismatch of two crystal structures, which is defined as $f = (a_{OL} - a_{BL})/a_{BL}$, a_{OL} and a_{BL} being the lattice constants of the overlayer and the buffer layer respectively, plays an important role in defining the degree of strain and dislocations present in a film and, therefore, must be minimized. A film strain can be tensile when $f < 0$, or compressive if $f > 0$, and might lead to film buckling or, in some cases, to an alteration of the film morphology from a 2D layer-by-layer fashion to a 3D crystallites formation, giving rise to rough and sometimes non-continuous overlayers [126]. On the other hand, an in-plane rotation of the overlayer lattice during deposition, in order to minimize the large lattice mismatch, can be beneficial and, sometimes, lead to a coincidence matching ('quasi-epitaxial') of the two lattices [127, 128].

Another important aspect that must be taken into account while superimposing thin films formed from different materials is the possibility of chemical reactions (e.g. intermixing or oxidation/reduction) at their interface. For instance, a partial intermixing between a buffer layer and an overlayer might take place (with or without annealing treatments) if the two materials can form a mixed phase that is chemically stable. Since it is difficult to predict the degree of this interdiffusion and foresee its dependence on time and temperature [126], the growth of adjacent layers using immiscible elements is also greatly recommended.

4.2 Selection of buffer layers for the growth of tetragonal Mn_3Ge films

Thin films of tetragonal Mn_3 -based Heusler compounds have been demonstrated to exhibit PMA but they have been grown only using single crystalline substrates such as $\text{SrTiO}_3(001)$ or $\text{MgO}(001)$, using buffer layers formed from a variety of materials but preferably chromium (Cr) or platinum (Pt) [88, 111, 113, 122, 123, 129, 130]. Single crystal substrates are far more expensive than Si substrates, therefore they are not suitable for technologically-relevant applications. Furthermore, in MRAM architectures, the MTJs are usually grown on wires that are formed from polycrystalline copper (Cu), that might also be covered with other polycrystalline or amorphous layers [87]. Also, the use of buffer layers formed with heavy metal elements like Pt for the growth of the magnetic electrodes is detrimental for MTJs that are operated using the STT mechanism, for the reasons explained in Chapter 1.

Thin films of Mn_3Ge grown directly on an amorphous SiO_2 surface do not display a well-defined crystalline texture. The magnetic anisotropy of these Mn_3Ge films is not constrained along preferential crystallographic directions and, therefore, the film magnetization is not aligned perpendicular to the film surface. Sometimes the use of a buffer layer, not only with the appropriate structure but also with the right crystallographic orientation, can promote the suitable growth of overlayers with the desired texture. For example, when deposited directly on an amorphous surface such as SiO_2 , materials with a *fcc* structure like Cu or Pt will preferentially be textured with (111) crystal planes parallel to the surface of the film; instead, *bcc* materials will tend to grow with (110) crystal planes parallel to the surface of the film. Therefore, it is vital to find a proper combination of buffer layers that, once grown on $\text{Si}(001)/\text{SiO}_2$ substrates, will be highly (001)-textured in

order to promote the out-of-plane (001)-oriented growth of Mn_3Ge thin films. Such underlayer must also have an in-plane lattice constant (or constants) that matches as much as possible with the one of bulk $\text{D0}_{22}\text{-Mn}_3\text{Ge}$.

The unit cell of $\text{D0}_{22}\text{-Mn}_3\text{Ge}$ has the following lattice constants: $a = 3.75 \text{ \AA}$ and $c = 7.12 \text{ \AA}$. As mentioned in Chapter 2, the structure of $\text{D0}_{22}\text{-Mn}_3\text{Ge}$ forms in a layer-by-layer fashion, with Mn-Mn atoms located in one layer, and Mn-Ge atoms located in the adjacent layer (refer to Fig. 2.6). This atomic configuration can be seen as a superlattice version of a simpler L1_2 *fcc* structure. Fig. 4.1 shows an example of $\text{L1}_2\text{-IrMn}_3$. Also in this case, the Mn-Mn atoms are positioned in one layer, while Ir-Mn atoms sit on the adjacent layer, with a crystal symmetry that matches one of the two $\text{D0}_{22}\text{-Mn}_3\text{Ge}$ sublattices. Moreover, the in-plane lattice parameter of IrMn_3 (3.78 \AA) happens to be very similar to the one of Mn_3Ge (3.75 \AA): these two materials have a very small lattice mismatch, $f \sim -1\%$. Hence, IrMn_3 represents a good candidate as buffer material for the epitaxial growth of Mn_3Ge thin films.

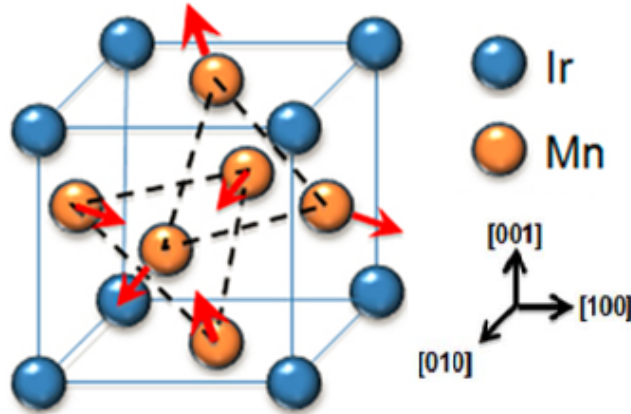


FIGURE 4.1: Schematics of a $\text{L1}_2\text{-IrMn}_3$ unit cell. The triangular and non-collinear alignment of the Mn atoms' moments is highlighted by the dashed black lines and red arrows [131].

IrMn_3 is a well-known AFM material, characterized by a non-collinear and triangular configuration of the Mn magnetic moments [131], as shown in Fig. 4.1.

IrMn₃ has been widely used for in-plane magnetized MTJs [132] as an exchange-bias layer to magnetically fix the orientation of the reference electrode. In 2004, the growth of (001)-oriented IrMn₃ seed layers on TaN films, grown using Si/SiO₂ substrates, was reported by Parkin and collaborators [20]. In their work, the IrMn₃ films were sometimes found to be polycrystalline, showing random (111)-oriented grains that caused the propagation of structural defects through the MTJ over-layers. Polycrystalline IrMn₃ layers consisting of grains that are, instead, strongly (001)-textured are needed to sustain the growth of (001)-textured Mn₃Ge thin films, to guarantee that the tetragonal elongated axis aligns perpendicular to the film plane.

4.2.1 Si(001)/ SiO₂/ TaN/ IrMn₃ (TI)

200 Å-thick Ta_{1-x}N_x films were deposited at RT on amorphous Si/SiO₂ substrates by reactive magnetron sputtering from a Ta target, using a gas mixture of Ar and N₂. The gas pressure during deposition was of 3 mTorr. RBS was used to study the Ta_{1-x}N_x films composition. An ideal ratio of 90% Ar and 10% N₂ led to the formation of TaN films with a 1:1 composition. Out-of-plane x-ray diffraction (XRD) measurements were carried out at RT using a Bruker GADDS system to investigate the structural properties of the Ta_{1-x}N_x series (Fig. 4.2). Films with a preferential *fcc*-(111) texture were formed using gases mixtures in the range between 90/10 and 75/25. On the other hand, for lower (or zero) N₂ gas contents, mixed *hcp* and *bcc* phases with weak texture were found. 100 Å-thick IrMn₃ films were then sputtered at RT from a IrMn₃ target using IBD onto the Ta_{1-x}N_x underlayers. The 1:3 composition of the IrMn₃ films was confirmed by RBS.

The XRD data from Fig. 4.3a show that a pure Ta underlayer (black curve) promoted the growth of IrMn₃ with a preferential (111) orientation. Instead,

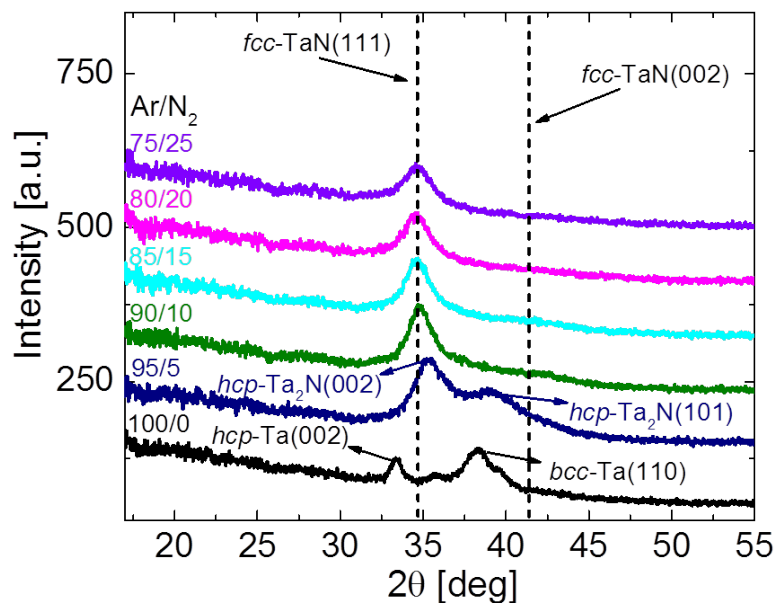


FIGURE 4.2: $\omega - 2\theta$ XRD scans of different 200 Å $\text{Ta}_{1-x}\text{N}_x$ films. The different Ar/ N_2 ratios used during deposition are labeled one the left side of the graph.

within the entire 95/5 – 75/25 range, all the IrMn_3 films grown on the $\text{Ta}_{1-x}\text{N}_x$ underlayers crystallized with (001) planes that were parallel to the film plane.

Furthermore, structural properties of 100 Å-thick IrMn_3 films deposited onto a Ta_1N_1 underlayer (grown using the ideal 90/10 Ar/ N_2 ratio) with different thicknesses are illustrated in Fig. 4.3b. As previously discussed for the general case of materials with a *fcc* structure, the IrMn_3 films showed a (111)-oriented texture when deposited directly on the amorphous SiO_2 surface, i.e. at zero thickness of TaN (olive curve). However, all the other IrMn_3 films were found to crystallize with the preferential (001) orientation, with IrMn_3 -(002) Bragg peak intensities increasing for increasing thickness of the TaN underlayer [133].

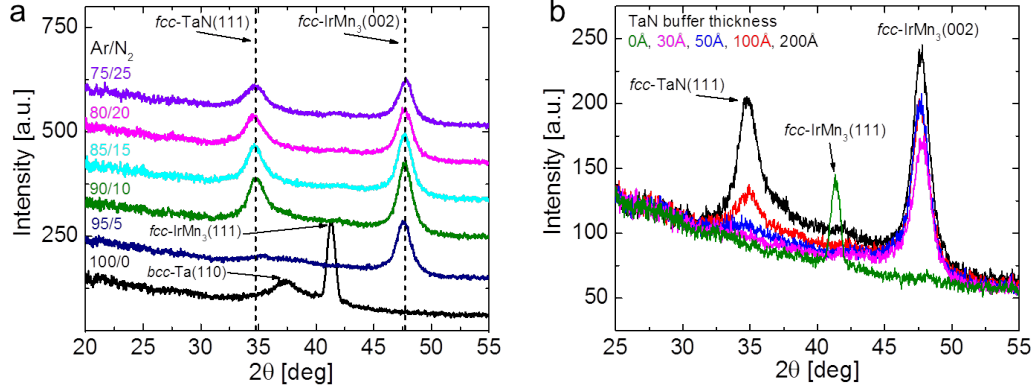


FIGURE 4.3: $\omega-2\theta$ XRD scans of (a) 100 Å IrMn₃ films grown onto 200 Å Ta_xN_{1-x} films; the different Ar/N₂ ratios used during deposition of the Ta_xN_{1-x} films are labeled on the left side of the graph; and (b) 100 Å IrMn₃ films grown onto Ta₁N₁ layers (using the Ar/N₂ ratio of 90/10) deposited with different thicknesses [87].

4.2.2 Si(001)/SiO₂/TaN/IrMn₃/TaN (TIT)

During the annealing step of the Mn₃Ge films (the deposition and optimization of these films will be presented in the next chapter) grown onto TI buffer layers, an inter-diffusion at the interface between the IrMn₃ and Mn₃Ge layers was detected (see Fig. 4.4) by high-resolution transmission electron microscopy (HRTEM) and electron energy loss spectroscopy (EELS) measurements carried out using a JEOL ARM 200F with a Cold-FEG source operated at 200 keV.

EELS data clearly revealed an inter-mixing of the Ir and Ge elements between these two layers (Fig. 4.5a and 4.5b). This segregation of elements was found to be detrimental for the magnetic properties of the Mn₃Ge layer, i.e. a substantial reduction of magnetic moment and perpendicular magnetic anisotropy was discovered (see next chapter). An ultra-thin 10-20 Å TaN layer was deposited at RT on TI layers (TIT) before Mn₃Ge in order to prevent this interdiffusion. Indeed,

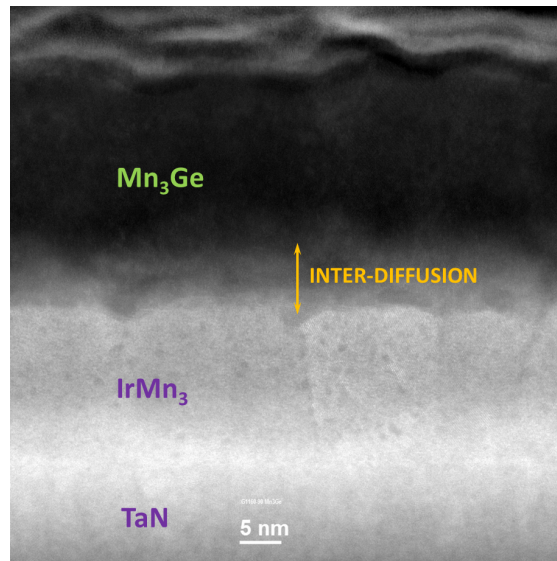


FIGURE 4.4: HRTEM showing inter-layers atomic migration through grain boundaries caused by thermal annealing after Mn_3Ge deposition. The sample stack was: $\text{Si}(001)/250 \text{ \AA} \text{SiO}_2/200 \text{ \AA} \text{TaN}/200 \text{ \AA} \text{IrMn}_3(\text{TI})/300 \text{ \AA} \text{Mn}_3\text{Ge}$ (grown at RT and *in-situ* annealed at $450 \text{ }^\circ\text{C}$)/ $30 \text{ \AA} \text{Ta}$.

EELS data confirmed that no sign of mass transport occurred when the TaN diffusion barrier was used, as shown in Fig. 4.5d. The use of only a single TaN buffer layer (without IrMn_3) led to the formation of Mn_3Ge films having much poorer quality.

4.2.3 $\text{MgO}(001)/\text{MgO}/\text{Cr}$ (MC)

In recent years, tetragonal Mn_{3+x}Ge Heusler films have been directly deposited either onto $\text{MgO}(001)$ single crystal substrates [130] or using Cr- [129] and Cr/Rh buffered $\text{MgO}(001)$ substrates [110]. In all these cases, the Mn_{3+x}Ge films displayed decent or good PMA properties. Thus, in this work, it was decided to also grow Mn_3Ge films on Cr-buffered $\text{MgO}(001)$ single crystal substrates to compare

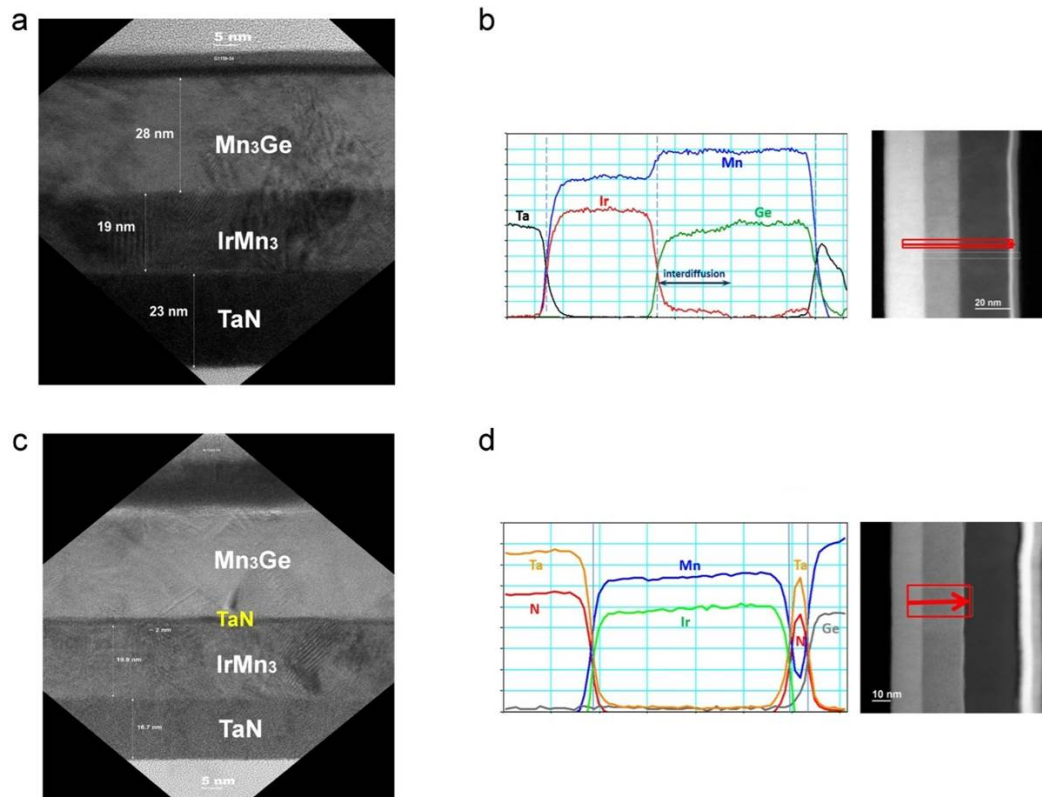


FIGURE 4.5: (a) and (c): HRTEM images of films with the structure Si(001)/ 250 Å SiO₂/ 200 Å TaN/ 200 Å IrMn₃ (TI)/ 300 Å Mn₃Ge (grown at RT and *in-situ* annealed at 450 °C)/ 30 Å Ta, and Si(001)/ 250 Å SiO₂/ 200 Å TaN/ 200 Å IrMn₃/ 20 Å TaN (TIT)/ 300 Å Mn₃Ge (grown at RT and *in-situ* annealed at 450 °C)/ 30 Å Ta, respectively. (b) and (d): EELS data from the corresponding (a) and (c) structures. The concentration of Ta, N, Mn, Ir, and Ge was determined within the samples' probed regions (shown in the right panels with the red horizontal rectangles and arrows) [87].

their properties with respect to films deposited on amorphous Si/SiO₂ substrates using both TI and TIT seed layers.

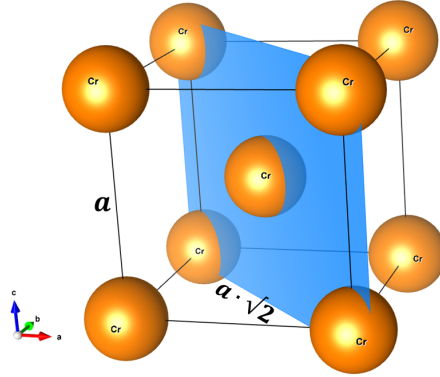


FIGURE 4.6: Schematic of the *bcc*-Cr unit cell. The (110) plane is shown in blue.

Cr is a 3d transition metal that typically crystallizes with a *bcc* structure. Within the Cr unit cell, the (110) plane is the most dense atomic plane, as illustrated in Fig. 4.6. When deposited on an amorphous surface, Cr atomic layers tend to stack with (110) crystallographic planes that are parallel to the film surface. The Cr lattice parameter, $a = 2.88 \text{ \AA}$, is too small compared to the shorter (in-plane) lattice dimension of Mn₃Ge (3.75 Å), i.e. the compressive strain resulting from the deposition of Mn₃Ge on Cr would be too large. However, a 45 deg in-plane rotation of the Mn₃Ge unit cell with respect to the Cr seed layer, aligning along the $a \cdot \sqrt{2}$ ($\sim 4.07 \text{ \AA}$) direction (as shown in Fig. 4.6), allows a better-matched growth of the Heusler compound on Cr. Yet, this lattice mismatch is quite significant ($f \sim 7\%$) compared to the one between IrMn₃ and Mn₃Ge ($f \sim -1\%$). Therefore, better magnetic properties are expected from Mn₃Ge films grown on TI and TIT buffer layers than from those deposited on Cr.

After being soaked in a methanol bath for 30 minutes, the MgO(001) substrates were inevitably exposed to water vapor prior to being loaded inside the deposition chamber. For this reason, the substrates were initially far from being completely

clean and atomically smooth. It is believed that the substrate surface is likely characterized by atomic steps and microscopic terraces associated to the formation of $\text{Mg}(\text{OH})_2$ brucite [134]. Hence, the $\text{MgO}(001)$ substrates were firstly heated up to $650\text{ }^\circ\text{C}$ in ultra-high vacuum (UHV) for half an hour in order to evaporate the residual brucite. Then, prior to the deposition of Cr, an ultra-thin (20 \AA) MgO layer was grown to uniformly cover and smooth down the substrate surface. The latter was deposited by ion beam sputtering of a $\text{Mg}_{50}\text{O}_{50}$ target at RT. Finally, a 400 \AA -thick Cr layer was deposited using IBD at RT, and consequently annealed in UHV conditions at $700\text{ }^\circ\text{C}$ for 30 minutes. The mechanism through which the Cr atomic layers stacked onto the MgO layer is the same as for the mentioned Cr/ Mn_3Ge case. The obtained MgO/Cr bilayer (with lattice mismatch of $f \sim -3\%$) is referred to as 'MC' buffer layer and it was only utilized with $\text{MgO}(001)$ single crystal substrates. The optimized $\text{MgO}(001)/\text{MC}$ stack showed low surface roughness of less than $\sim 3\text{ \AA}$ and a highly (001)-textured *bcc*-Cr atomic structure. Fig. 4.7 is a summarizing sketch of the substrate/buffer layer combinations that were developed for the growth of tetragonal Mn_3Ge Heusler thin films.

4.3 Summary

In summary, the criteria used for the choice and development of optimal buffer layers for the suitable growth of tetragonal Mn_3Ge thin films with a (001) texture were presented. It was shown that seed layers formed from bilayers of TaN/ IrMn_3 (TI), that were directly deposited on amorphous $\text{Si}(001)/\text{SiO}_2$ substrates at RT, showed a strong out-of-plane (001) texture. Moreover, it was demonstrated that an ultra-thin TaN layer grown on TI could be used to stop the interdiffusion between the IrMn_3 and Mn_3Ge layers, with the final TaN/ IrMn_3 /TaN underlayers named TIT (a patent was filed [133]).

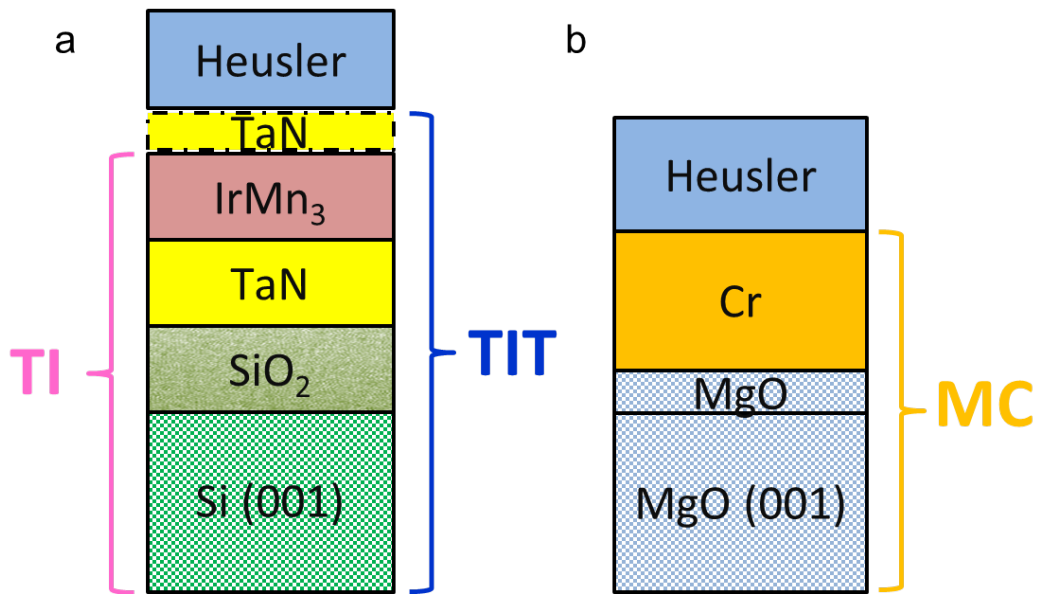


FIGURE 4.7: Schematics and nomenclature of buffer layers developed using (a) amorphous and (b) crystalline substrates [87].

The procedure for the growth of a MgO/Cr (MC) buffer layer deposited on single crystal MgO(001) substrates was also described. The purpose of the MC films was to develop an alternative buffer layer (to TI and TIT) in order to investigate how the different substrate/underlayer combinations would influence the growth of Mn₃Ge and its properties.

Chapter 5

Mn₃Ge: a tetragonal Heusler compound with giant perpendicular magnetic anisotropy

5.1 Optimization of structural, morphological, and magnetic properties of Mn₃Ge thin films

The structural and magnetic properties of Mn₃Ge thin films delicately depend on their composition and atomic order. The latter is strongly affected by the deposition temperature and subsequent anneal. These conditions clearly influence also the smoothness of the Mn₃Ge films.

5.1.1 Composition dependence

Initially, $Mn_{3+x}Ge$ thin films were DC-sputtered at a substrate temperature of 450 °C using Mn_xGe_y targets with different compositions. Amorphous Si/SiO₂ substrates with TI buffer layers were used. The Ar deposition pressure during deposition was 3 mTorr. $Mn_{3+x}Ge$ films were capped with a 30 Å Ta protecting layer (this protective layer was commonly used during the studies of both Mn_3Ge and $Mn_{3-x}Co_xGe$ thin films; Hence, the 30 Å Ta capping film will not be mentioned in the next sections) deposited at RT and utilized to prevent the oxidation of the Heusler films.

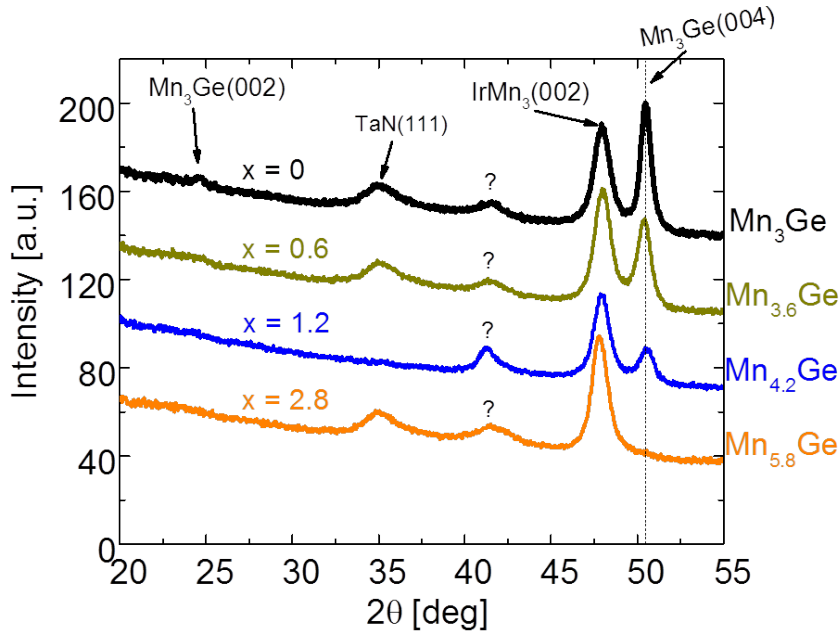


FIGURE 5.1: $\omega - 2\theta$ XRD scans of 300 Å $Mn_{3+x}Ge$ films deposited at a substrate temperature of 450 °C. The undefined peaks, indicated with question marks, possibly correspond to a mixed phase between the $IrMn_3$ and $Mn_{3+x}Ge$ layers.

Fig. 5.1 shows x-ray diffraction measurements carried out at RT on these films. On the right side, the chemical compositions of the Heusler films, measured using

RBS analysis, are displayed. The (004)-oriented Bragg reflection associated with the tetragonal phase of Mn_{3+x}Ge was found for a 2θ angle ~ 50 deg, and gradually increased with decreasing x (Mn poorer films). The finest degree of atomic ordering was found for films with the stoichiometric 3:1 composition (black line in Fig. 5.1). This could also be confirmed by the presence, at a 2θ angle of ~ 25 deg, of the Mn₃Ge-(002) superlattice peak, that proved the formation of ordered and distinct adjacent layers forming the tetragonal structure of Mn₃Ge. The out-of-plane lattice constant of this film was estimated (from the XRD data) to be $c = 7.18$ Å, very close to its bulk value of 7.12 Å.

A SQUID-VSM (Superconducting Quantum Interference Device, SQUID, combined with a Vibrating Sample Magnetometer, VSM) was used to investigate the magnetic properties of the stoichiometric Mn₃Ge Heusler film. The magnetization versus applied magnetic field loops measured at RT are shown in Fig. 5.2. Mn₃Ge clearly displayed a hard FiM behavior: excellent PMA with very large coercive field of ~ 6 T and anisotropy field exceeding 7 T were demonstrated. Also, the value of the spontaneous magnetization, M_S , was ~ 135 emu/cc, slightly lower than the predicted bulk value of 175 emu/cc. This discrepancy was likely due to a substantial inter-diffusion between the IrMn₃ underlayer and the Mn₃Ge layer caused by the high-temperature growth condition. Note that the films with off-stoichiometry composition (Mn_{3+x}Ge with $x \geq 0.6$) displayed inferior properties, namely lower magnetic moment and anisotropy. Given the large PMA and the c lattice constant closely matching with the bulk value (the in-plane a lattice constant was not measured), the Mn₃Ge film was strongly believed to be forming with the desired tetragonal D0₂₂ structure. However, due to the high deposition temperature, the surface roughness of this film was found to be quite high. The root mean square (rms) roughness, r_{rms} , measured using atomic force microscopy, was ~ 40 Å: this value needed to be significantly reduced.

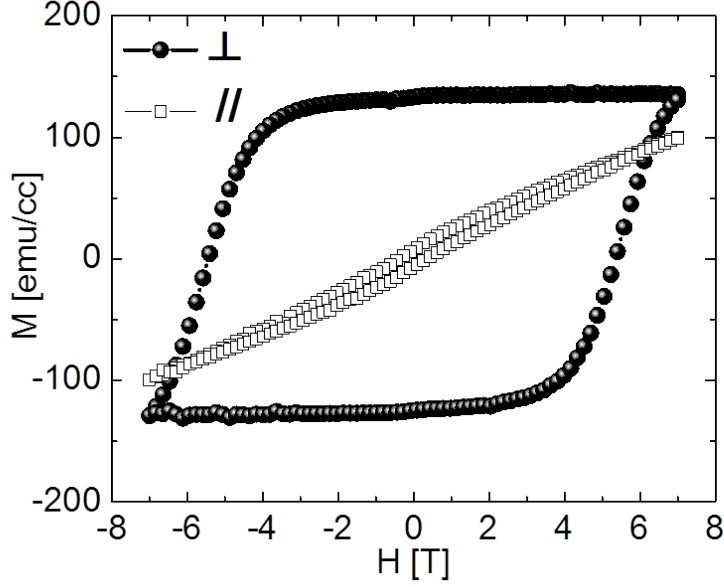


FIGURE 5.2: Mn_3Ge magnetization hysteresis loops with applied magnetic field parallel (empty squares) and perpendicular (solid balls) to the plane of the sample. As a comparison, the magnetization of Mn_3Ge is roughly ten times smaller than the one of $CoFeB$.

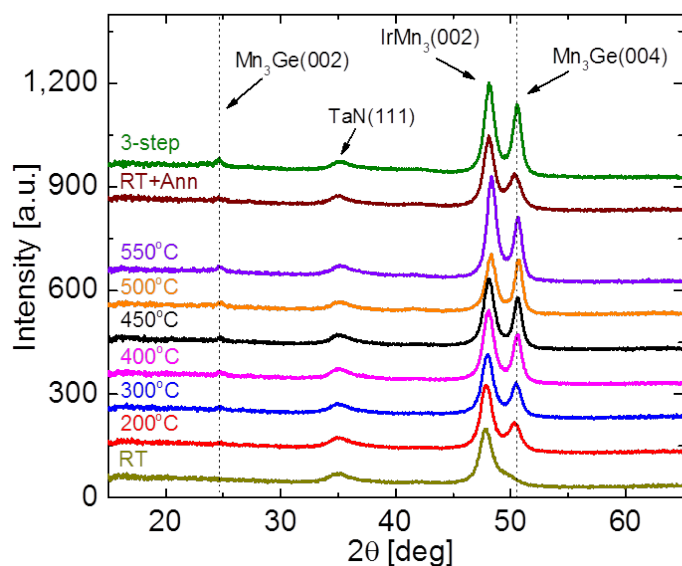
5.1.2 Growth temperature dependence and 3-step process

In order to attain ideal MTJ performance the magnetic electrodes must be atomically smooth. One approach used to improve the film roughness was to deposit Mn_3Ge at lower growth temperatures (T_G). Fig. 5.3 (A) illustrates XRD out-of-plane $\omega - 2\theta$ measurements for a series of 300 Å-thick Mn_3Ge films deposited at increasing T_G . Distinct Mn_3Ge peaks with (001) texture were observed for films grown at T_G only greater than RT. The quality factor, defined as the ratio $I(002)_{exp}/I(004)_{exp}$ of the XRD reflection intensities of Mn_3Ge films (extracted from Fig. 5.3(A)) is shown in the top panel of Fig. 5.3(B). This factor is directly related to the chemical ordering of Mn and Ge in the Heusler alloy. Also, it can be seen that the ratio $I(004)_{Mn_3Ge}/I(002)_{IrMn_3}$ (red open squares), i.e. the measure

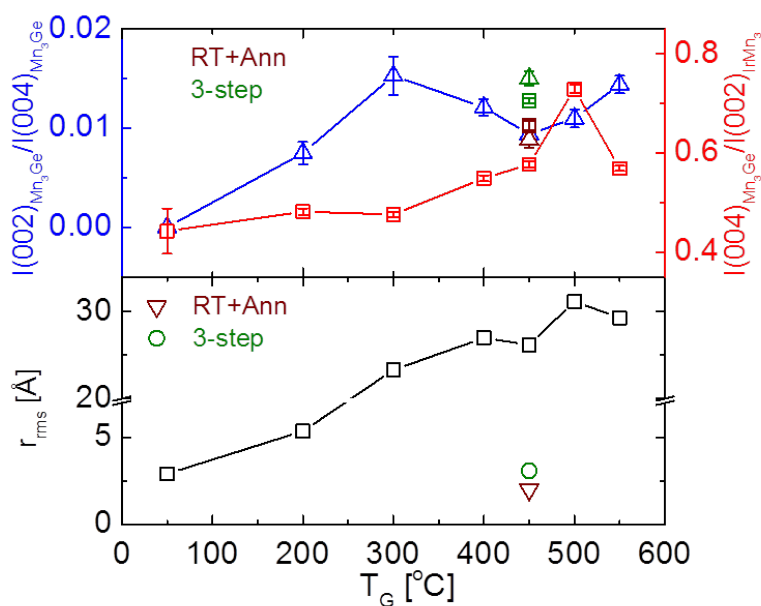
of the Mn₃Ge texture, increases with increasing T_G. The bottom panel in Fig. 5.3(B) displays the dependence of r_{rms} upon T_G: it considerably increases when T_G exceeds modest temperatures of just ~ 200 °C. Specifically, r_{rms} < 5 Å for T_G ≤ 200 °C, while r_{rms} > 20 Å for T_G > 200 °C. Rough Mn₃Ge films formed using such conditions are unsuitable for technological applications, but, at the same time, high temperature depositions were needed to sustain the Heusler structure (as confirmed from the XRD data).

An optimal growth technique was discovered that involved a 3-step process for the Mn₃Ge electrode, in which an initial 20 Å Mn₃Ge layer was grown at 450 °C, followed by a thicker Mn₃Ge layer deposited at T_G = 150 °C, with a final in-situ anneal at 450 °C for 1-2 hours in UHV, leading to smooth films (r_{rms} ~ 3 Å) with comparable chemical ordering as the films grown at T_G = 450 °C (see the olive plot in Fig. 5.3(A) and the olive symbols in Fig. 5.3(B)) [87].

In Fig. 5.4, the magnetic properties of Mn₃Ge films with varying thickness, grown using the 3-step process on amorphous substrates as well as on a crystalline MgO(001) substrate with MC seed layers, are compared. An exceptional PMA character was found for all cases but the highest coercive and anisotropy fields were observed for films grown using the TIT underlayer. Coercive fields of 6 T and anisotropy fields exceeding 7 T were found. Fig. 5.4b summarizes the magnetic moment *m*, coercivity H_C, and uniaxial magnetic anisotropy density K_U for these films. Values of *m* for Mn₃Ge films grown on TIT underlayers were close to those theoretically predicted for bulk Mn₃Ge, but *m* was significantly lower by ~ 15-35% for Mn₃Ge films grown using TI and MC underlayers. For film deposited on MC, it was also found that K_U was considerably lower: this was attributed to the large lattice mismatch (~ 7%) between Cr and Mn₃Ge [87].



(A) XRD measurements of Mn_3Ge films grown at different growth temperatures on Si/SiO₂ substrates using TI underlayers. The top two curves, shown for comparison, represent the RT deposition with in-situ anneal (brown) and the 3-step process (olive).



(B) Dependence of chemical ordering (top panel) and r_{rms} (bottom panel) of Mn_3Ge films upon T_G .

FIGURE 5.3: Structural and topographical properties of Mn_3Ge films deposited using different growth conditions on TI buffer layers

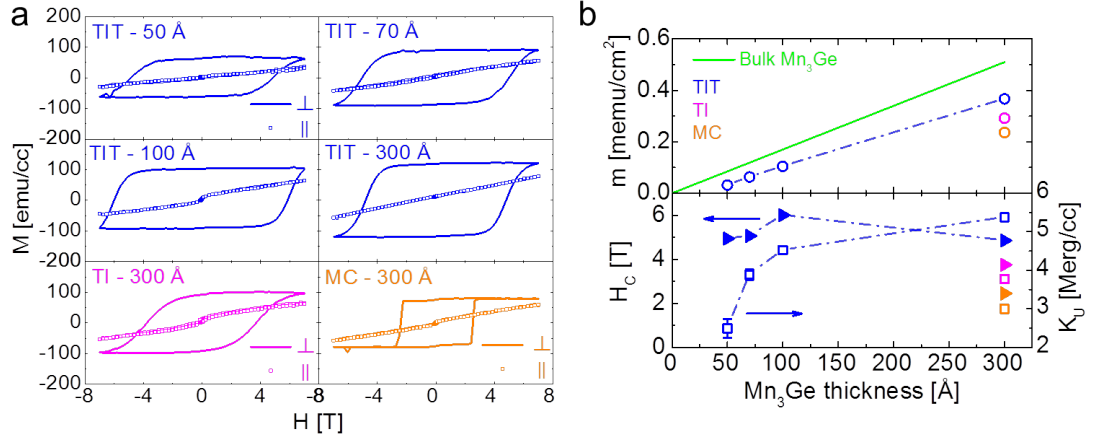


FIGURE 5.4: (a) Magnetization vs. field hysteresis loops, measured at RT, of Mn_3Ge films grown on Si/SiO₂ substrates with TI (magenta), TIT (blue) underlayers, and MgO(001) single crystal substrate with MC (orange) underlayers. TI (TIT) had the following structure: Si/SiO₂/200 Å TaN/200 Å IrMn₃ (/10 Å TaN)); while MC had the following structure: MgO(001)/20 Å MgO/400 Å Cr. For the TIT films the thickness of the Mn_3Ge layer, deposited using the 3-step process, was varied. The out-of-plane (in-plane) loops are shown as solid lines (open squares). (b) Top panel - magnetic moment m , extrapolated from Fig. 5.4(a), versus Mn_3Ge thickness. The green straight line shows the calculated moment of bulk D0₂₂- Mn_3Ge [108]. Bottom panel - coercive field H_C (solid triangles) and uniaxial magnetic anisotropy density K_U (empty squares). The latter was calculated using $K_U = H_K \cdot M_S/2 + 2\pi M_S^2$, where H_K is the effective magnetic field, generally extracted from the M vs. H hard-axis loop as the field at which the magnetization reaches saturation. As displayed in Fig. 5.4a, the Mn_3Ge magnetization could not be fully saturated in the plane of the film using the available magnetic field (7 T); thus, H_K was considered as a lower bound [87].

5.2 Mn₃Ge-based perpendicular magnetic tunnel junctions

5.2.1 Devices fabrication

Once the optimization of the structural, magnetic and morphological properties of the Mn₃Ge films was completed, the following task was to integrate these films into MTJ devices. Before patterning, the samples were post-annealed at 350 °C for 60 minutes in a high-vacuum chamber using an applied magnetic field of 1 T directed out of the plane of the samples. This annealing procedure was carried out in order to improve the quality of the CoFeB layer and its interface with the insulating MgO spacer, the latter being RF-sputtered at RT from a MgO target.

Devices with sizes of $1 \times 2 \mu\text{m}^2$ and ~ 30 nm in diameter were fabricated by standard optical lithography and e-beam lithography, respectively. The MTJ structures used are displayed in Fig. 5.5. CoFeB and Mn₃Ge layers formed the magnetic electrodes: the first one was used as the free layer, while the second one as the pinned layer.

Only the free layer was patterned to define the junction size while the reference layer was not patterned, as illustrated in Fig. 5.6d. The lateral sides of the MTJ devices were protected with an Al₂O₃ layer (brighter color at both sides of the junction in Fig. 5.6d), and the electrical device contacts were formed using a 50 Å Ru/650 Å Au bilayer [87].

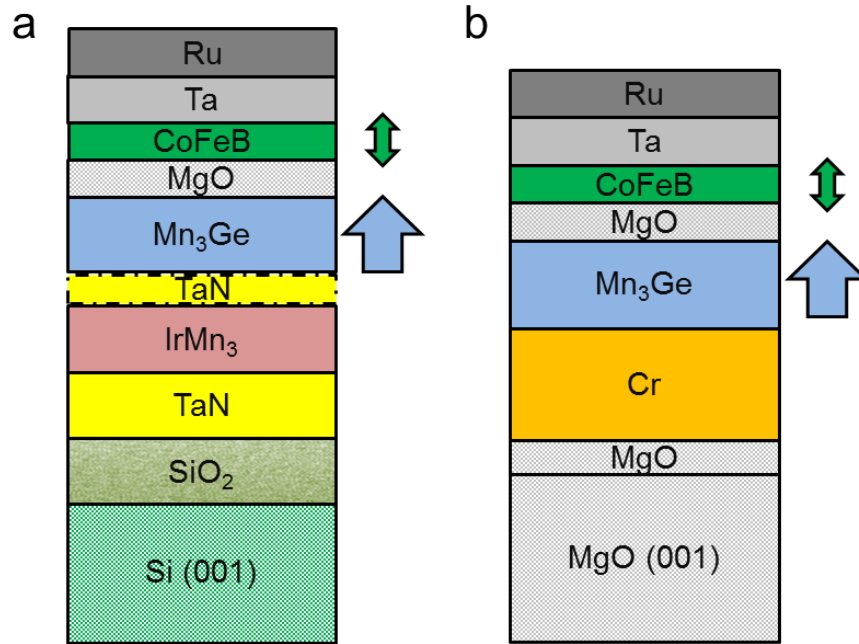


FIGURE 5.5: Schematics of the MTJ structures grown on (a) amorphous Si/SiO₂ and (b) MgO(001) single crystal substrates. In some cases a TaN diffusion barrier layer was used as illustrated by the dashed line. The CoFeB layers had a 20:60:20 composition.

5.2.2 Tunneling magnetoresistance properties

The tunneling magnetoresistance of the patterned devices was evaluated using a Quantum Design DynaCool physical property measurement system and a custom-built probe station equipped with Keithley source meters 2602 and 2400.

The TMR versus perpendicular magnetic field measured at 300 K (smaller squares) and 3 K (larger squares) is displayed in Fig. 5.6a for the patterned MTJ devices ($1 \times 2 \mu\text{m}^2$) developed using the TI and TIT underlayers. For all cases, very high applied magnetic fields (± 9 T) were needed in order to align the magnetic moments of the Mn₃Ge and CoFeB layers parallel to each other (P state) due to the the giant uniaxial anisotropy of Mn₃Ge. The junction resistance was higher in the P state compared to the AP state, that was obtained when the CoFeB moment

switched its direction at applied magnetic fields close to zero. Therefore, the TMR - defined as $[(R_{AP} - R_P)/R_{AP}] \times 100$ - was negative with values of $\sim -35\%$ at 300 K and $\sim -74\%$ at 3 K. These were the highest values of TMR reported to date in p-MTJ devices using a tetragonally distorted Heusler compound as a magnetic electrode.

A HRTEM image of a typical MTJ device with a width of 27 nm, displayed in Fig. 5.6d, shows the great quality of the structure and device patterning. Fig. 5.6b illustrates that, for a given MTJ device, R_{AP} barely changed, while R_P monotonically increased as T decreased, resulting in higher TMR for lower temperatures. Nevertheless, these values of TMR were much smaller than those predicted by density functional theory (DFT) calculations [87], as discussed in details in the next section.

5.2.3 Theoretical calculations of TMR and influence of the Brillouin zone filtering effect

Ab initio calculations of the electronic structure and transport properties of Mn₃Ge/MgO/Fe MTJs were performed to explain the low TMR found experimentally. In order to simplify the calculations, a *bcc* Fe system was used rather than CoFeB (used in the experiments) [87]. The electronic structure and transmission functions of Mn₃Ge/MgO/Fe and Fe/MgO/Fe MTJs were calculated using a tight-binding linear muffin-tin orbital method in the atomic sphere approximation (TB-LMTO-ASA) with the local density approximation of density functional theory (LDA/DFT) for the exchange-correlation energy. For the Mn₃Ge/MgO/Fe MTJ, the lattice constants of Mn₃Ge used were $a = 3.816 \text{ \AA}$ and $c = 7.261 \text{ \AA}$. The relaxed positions of the atoms at the Mn₃Ge/MgO interface (for all possible terminations)

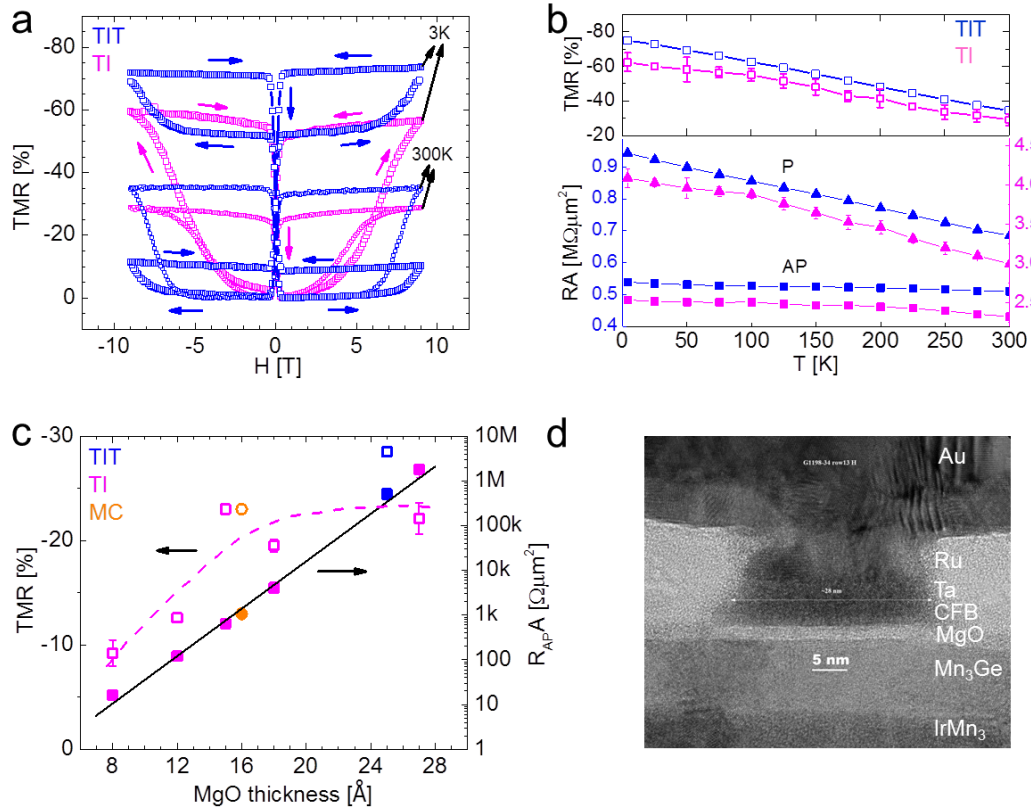


FIGURE 5.6: (a) TMR vs. H (perpendicular to the device plane) measured at 300 K (smaller squares) and 3 K (bigger squares) for MTJ devices grown using TI (magenta) and TIT (blue) buffer layers. For the TIT junction, two sets of data were measured at 3 K (blue bigger squares) after cooling down the device from 300 K in a magnetic field of +9 T and -9 T, respectively. These data are mirror images of each other, as can be noticed from the figure. All the other measurements were performed without field-cooling. (b) Temperature dependence of TMR (top panel) and R_{PA} and R_{APA} (bottom panel). (c) MgO thickness dependence of TMR (open symbols) and R_{APA} product (solid symbols), averaged over more than 20 devices. Solid and dashed lines are guides to the eye for R_{APA} and TMR, respectively. R_{APA} scaled exponentially with the MTJ barrier thickness. For fast evaluation of the TMR, the R_{AP} and R_P values were evaluated at +0.3 T and -0.3 T respectively, instead of sweeping the magnetic field from ± 9 T. (d) HRTEM image of an MTJ device \sim in size, with the following structure: Si/250 \AA SiO_2 /200 \AA TaN/200 \AA $IrMn_3$ /300 \AA Mn_3Ge /15 \AA MgO/15 \AA CoFeB/50 \AA Ta/50 \AA Ru [87].

were determined using the VASP molecular dynamic program. The O-top configuration was found to be the most stable configuration (as compared to Mg-top and Mg-hollow) for both terminations, in agreement with [135]. Regarding the Fe/MgO interface the atomic positions from [136] were used.

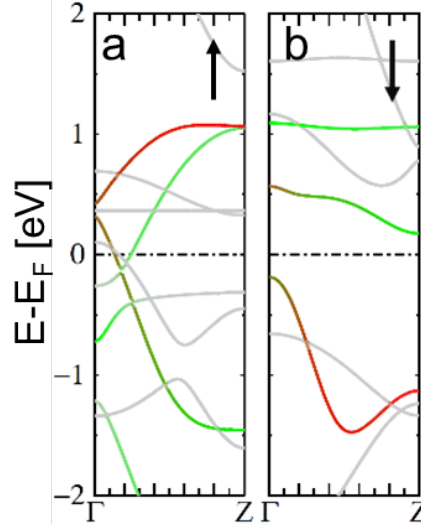


FIGURE 5.7: (a) Majority and (b) minority electron bands of bulk- Mn_3Ge along the Γ -Z line (along the k_z -axis) in the BZ. The red, green and light-grey colors of the bands were mixed with weights proportional to the projection of the wave function of the band to specific orbitals as follow: red color represented the $m = 0$ basis orbitals centered at the Mn and Ge atoms of the Mn-Ge layer, green color represented the $m = 0$ basis orbitals centered at the Mn atoms of the Mn-Mn layer, and grey color referred to all remaining $m \neq 0$ basis orbitals. [137].

In the $Mn_3Ge/MgO/Fe$ system studied, the contribution to transmission from majority Fe electrons is much larger than the one from minority Fe electrons, the latter being strongly suppressed due to the symmetry spin filtering properties of the Fe/MgO interface described in Chapter 1. Figures 5.7a and 5.7b illustrate the (a) majority and (b) minority electron bands of bulk- Mn_3Ge along the Γ -Z line (along the k_z -axis) in the BZ. Only the spin up electrons of bulk- Mn_3Ge have states crossing the Γ -Z line at E_F , and some of these states have significant $m = 0$ weights (red and green). Thus, these states are not prohibited by symmetry considerations

from coupling to the Δ_1 evanescent band of MgO having the smallest attenuation constant (refer to Chapter 1, section 1.2.1). Therefore, the combination of three factors - (I) the absence of minority Mn₃Ge states near E_F along Γ -Z line, (II) the presence of majority Mn₃Ge states crossing the Γ -Z line at E_F , and (III) the Γ -point focusing property of the MgO spacer - are referred to as the Brillouin zone filtering (BZF) effect [137] (see Fig. 5.8).

For a sufficiently large number of MgO layers, N_{MgO} , the BZF suppresses the contribution to transmission of the Mn₃Ge spin down electron channel. Similarly to the spin symmetry filtering, the strength of the BZF effect increases with N_{MgO} , since both effects are based on the Γ -point focusing property of the MgO barrier. As the transmission in a Mn₃Ge/MgO/Fe MTJ is mainly dominated by majority Fe electrons for both the P and AP configurations, the dominant contributions to T_P and T_{AP} originate from majority and minority Mn₃Ge electrons, respectively. Since the influence of the minority Mn₃Ge electrons to the transmission is suppressed by the BZF effect, the ratio T_P/T_{AP} (equivalent to the TMR) should increase with N_{MgO} (i.e. T_{AP} should decrease with increasing N_{MgO}).

In addition to the BZF mechanism, another factor played a significant role in determining the sign of the TMR: this was the native layer-dependent SP of Mn₃Ge. As shown in Fig. 5.9, both the Mn-Mn and Mn-Ge layers possess negative SP. Therefore, unlike the Fe/MgO case where the spin symmetry filtering and the positive SP of Fe strengthen each other, in the Mn₃Ge/MgO case the BZF effect and the negative SP of Mn₃Ge compete against one another. Specifically, the BZF tends to make the TMR of the Mn₃Ge/MgO/Fe system positive (by suppressing the contribution of the \downarrow Mn₃Ge electrons to the transmitted current), while the SP of Mn₃Ge tends to make the TMR negative (by favoring the contribution of the \downarrow Mn₃Ge electrons to the transmitted current). Thus, the overall sign of the TMR is determined by a delicate balance of these two conflicting mechanisms and

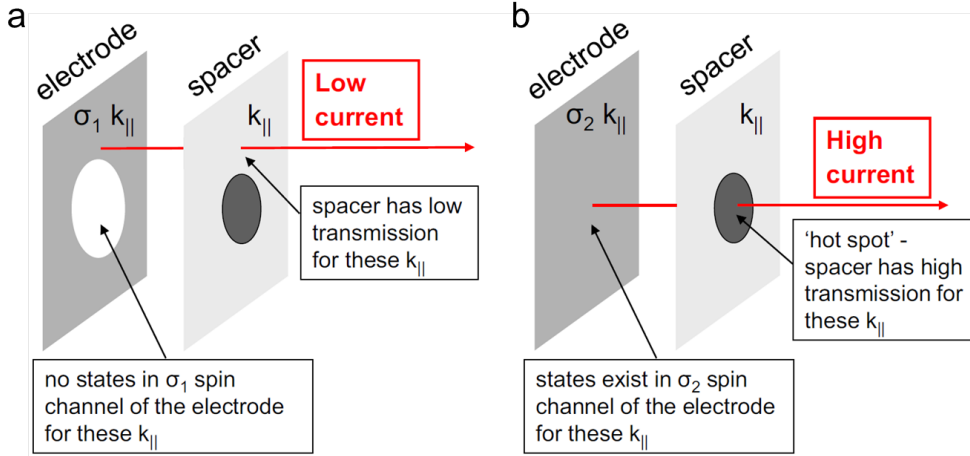


FIGURE 5.8: The Brillouin zone filtering effect in MTJs arises when the spacer has high transmission in some part of the 2D BZ surface, and the electrode does not have states in this part of the 2D BZ in one spin channel (leading to (a) low transmission) while it has states in this part of the 2D BZ in the other spin channel (leading to (b) high transmission). Therefore, the BZF mechanism tends to enhance the TMR of a tunnel junction. Reprinted with permission from [137] Copyright (2015) by the American Physical Society.

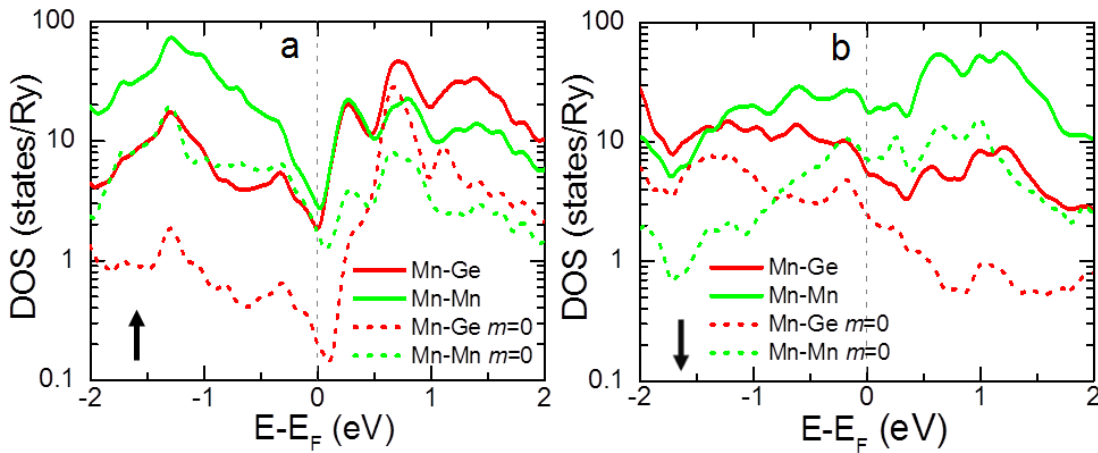


FIGURE 5.9: Majority (a) and minority (b) electron DOS of bulk- Mn_3Ge projected to Mn-Mn and Mn-Ge layers (solid green and red lines, respectively), as well as to $m = 0$ basis orbitals of Mn-Mn and Mn-Ge layers (dashed green and red lines, respectively) [87].

it could be influenced by different factors, such as N_{MgO} , the Mn_3Ge termination layers interfacing MgO (see Fig. 5.10b), and also the applied bias voltage.

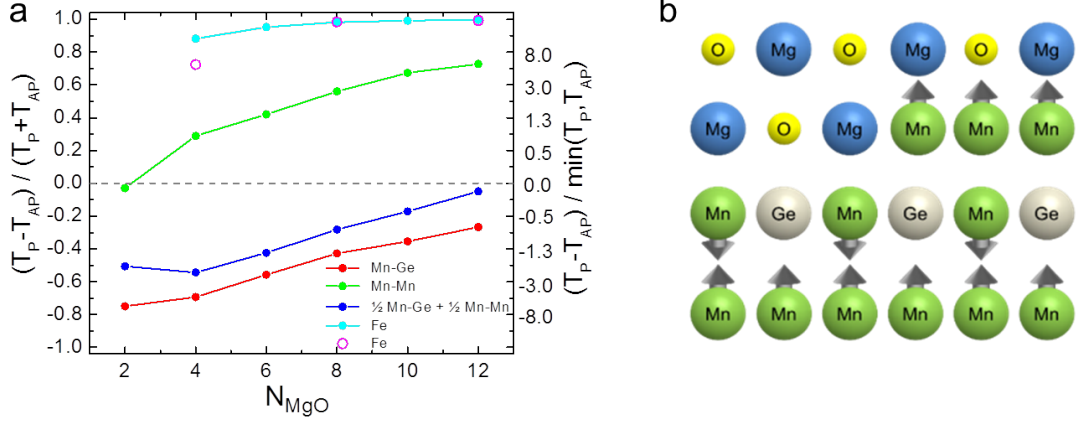


FIGURE 5.10: (a) TMR for $Mn_3Ge/MgO/Fe$ and $Fe/MgO/Fe$ MTJs versus N_{MgO} . The TMR for the $Mn_3Ge/MgO/Fe$ junction with Mn-Mn termination is shown in green, with Mn-Ge termination in red, and for the device with 'steps' (i.e. half of the device area with Mn-Mn termination and half with with Mn-Ge termination) it is shown in dark blue. The TMR for the $Fe/MgO/Fe$ MTJ calculated here by TB-LMTO method is shown in cyan color and calculated by the layer KKR method [16] is shown in pink. (b) Schematic of an atomic step between two distinct terminations of Mn_3Ge with opposite magnetic moments [87].

The evanescent state of bulk MgO with the smallest attenuation constant for states with fixed $k_{\parallel} \neq 0$ still consists mostly of $m = 0$ orbitals (i.e. s-orbitals of Mg and p_z -orbitals of O) in the area of the 2D BZ close to the Γ -point. Hence, due to symmetry considerations, this evanescent state of MgO will couple more strongly to the $m = 0$ orbitals than to $m \neq 0$ orbitals of the Mn_3Ge termination layers. Fig. 5.9a shows that the spin up DOS projected to $m = 0$ orbitals at E_F of the Mn-Ge layer is roughly an order of magnitude smaller than the spin down DOS projected to $m = 0$ orbitals at E_F ; on the other hand, for the Mn-Mn layer the DOS projected to $m = 0$ orbitals in both majority and minority channels do not significantly differ. Thus, this large difference in SP of the Mn-Ge and Mn-Mn

layers favors a more negative TMR for the Mn-Ge termination as compared to the Mn-Mn one, considering the same N_{MgO} . This conclusion is in agreement with the TMR presented in Fig. 5.10a. Here, the TMR for a $\text{Mn}_3\text{Ge}/\text{MgO}/\text{Fe}$ MTJ was displayed as a function of N_{MgO} , for $N_{\text{MgO}} \geq 2$. Two definitions of TMR were used: $(T_{\text{P}} - T_{\text{AP}}) / \min(T_{\text{P}}, T_{\text{AP}})$, which can vary from $-\infty$ to $+\infty$, (definition generally used for the experimental data) and $(T_{\text{P}} - T_{\text{AP}}) / (T_{\text{P}} + T_{\text{AP}})$, that can vary from -1 to +1. T_{P} and T_{AP} define the transmission functions (calculated at zero bias voltage) corresponding to the P and AP states, respectively. Indeed, the TMR is negative for the Mn-Ge termination (decreasing in magnitude with N_{MgO}), while it is positive for the Mn-Mn termination (increasing in magnitude with N_{MgO}). As the BZF effect gets stronger with increasing MgO thickness, the TMR in the case of the Mn-Ge termination layer would eventually (at sufficiently large N_{MgO}) change sign and become positive.

These considerations explain the low TMR values found experimentally in MTJs formed using a Mn_3Ge electrode. Even though the $\text{Mn}_3\text{Ge}/\text{MgO}$ interface was very smooth (refer to Fig. 5.6d) inevitably there would be some atomic scale fluctuations in the morphology of the Heusler layer giving rise to regions with Mn-Mn and Mn-Ge terminations interfacing the MgO spacer (see Fig. 5.10b), due to the underlying structure of the Mn_3Ge compound. The simplest way to model such fluctuations was to average the transmission functions over the different terminations (separately for P and AP states), assuming that the MgO thickness was the same across the device. The TMR calculated using this simple model with the assumption of equal areas occupied by Mn-Ge and Mn-Mn terminations is displayed in Fig. 5.10a with dark blue symbols. The calculations gave a negative TMR since both T_{P} and T_{AP} for the Mn-Ge termination were larger than those for the Mn-Mn termination (for all the N_{MgO} considered, i.e. ranging from 2 to 12). The negative TMR was consistent with the experimental data previously shown.

Note that due to the large 10.5% lattice mismatch between MgO and Mn₃Ge the BZF effect, which critically depends on the existence of the well-defined 2D BZ at the Mn₃Ge/MgO interface, was possibly more suppressed in actual devices as compared to the effect of the large negative SP that was less sensitive to the existence of the 2D BZ. Therefore, both ‘ideal crystal’ theoretical simulations (Fig. 5.10a) and non-ideal crystal arguments predicted negative TMR for the Mn₃Ge/MgO/Fe MTJ system, in strong agreement the experimental results (e.g. at low temperatures a TMR of $\sim -75\%$ was measured for a junction having a ~ 27 Å-thick MgO, see Fig. 5.6b) [87].

5.3 Summary

In summary, it was shown that the structural properties of Mn₃Ge thin films sensitively depend on their composition. The highest degree of atomic order was found in films forming with the stoichiometric 3:1 composition. For the first time, a method to grow highly textured and smooth ferrimagnetic Mn₃Ge Heusler films (with thicknesses down to only 50 Å) displaying giant perpendicular magnetic anisotropy on amorphous Si/SiO₂ substrates (a patent was published [133]) was presented. The discovery of suitable buffer layers and an optimized technique for the deposition of Mn₃Ge made possible the integration of these Heusler films into perpendicularly-magnetized magnetic tunnel junction devices, using Mn₃Ge as a reference electrode (and a soft CoFeB layer as recording electrode).

However, the compensated and negative TMR measured for these devices was strongly influenced by unavoidable atomic steps of the Mn₃Ge films at the interface with the MgO tunnel barrier. Transmission function calculations of similar MTJs showed that the TMR arising from Mn-Mn and Mn-Ge termination layers had

opposite signs, thus the overall TMR was compensated. A possible explanation for the low TMR was given by elucidating the delicate balance between two opposing effects that were taking place in such junctions: the Brillouin zone filtering effect and the negative bulk SP of the Mn₃Ge termination layers.

Chapter 6

Doping Mn_3Ge with Cobalt: study of the structural, electronic and magnetic properties of a $\text{Mn}_{3-x}\text{Co}_x\text{Ge}$ system

In the previous chapter it was shown that perpendicular magnetic tunnel junctions including a MgO spacer sandwiched by a FiM Mn_3Ge Heusler compound as reference electrode and a thin CoFeB layer as recording electrode displayed low TMR at RT. The TMR was compensated due to two competing mechanisms: the negative bulk spin polarization of Mn_3Ge , favoring a negative TMR, and the Brillouin zone filtering effect (originating at the $\text{Mn}_3\text{Ge}/\text{MgO}$ interface), favoring a positive TMR. One possible way to avoid this problem was to 'suppress' the BZF effect and let the SP be the only mechanism from Mn_3Ge to influence the tunneling properties of the $\text{Mn}_3\text{Ge}/\text{MgO}/\text{CoFeB}$ p-MTJs. Therefore, theoretical and experimental studies of the variation of the structural, electronic and magnetic

properties of a $Mn_{3-x}Co_xGe$ system for different concentrations of Co were carried out and compared. The main idea was to identify the right amount of Co that could modify the electronic configuration of the majority and minority Mn_3Ge electron bands and suppress the BZF mechanism, yet developing a FiM Heusler compound forming with a tetragonal structure, showing large PMA and same-sign layer-dependent SP. This optimized Heusler compound would be a better candidate than Mn_3Ge and could potentially satisfy all the requirements set for the electrodes materials to be integrated in p-MTJs for next-generation STT-MRAM.

6.1 Theoretical calculations

DFT calculations were carried out using the generalized gradient approximation of the density functional theory implemented within VASP program with projector augmented wave potentials. The ground state structure, whether cubic or tetragonal and whether regular or inverse, with its corresponding lattice constants and magnetic configuration of a $Mn_{3-x}Co_xGe$ system were investigated. The lowest energy configuration for $x = 0, 0.25, 0.5, 1, 1.5, 2$ was found from total energy calculations for different ordering of the Mn and Co atoms within the unit cell. The unit cell was varied in size according to x : for $x = 0, 1$ and 2 the unit cell was composed by 4 atoms; for $x = 0.5$ and 1.5 , it was composed by had 8 atoms; finally, for $x = 0.25$ the unit cell was composed by 16 atoms. To find the ground state magnetic configuration the energy was calculated for many different initial magnetic configurations. For compounds with 4 atoms in the unit cell, a $6 \times 6 \times 6$ k-point mesh was used for an initial rough estimation of the lattice parameters, and a $10 \times 10 \times 10$ k-point mesh with the energy cut-off equal to 400 eV was used for a fine-tuning of the lattice parameters. For compounds with 8 atoms and 16

atoms per unit cell, the number of k-divisions was reduced along the elongated axes.

x	Alloy	Reg/Inv	a_{tet} [Å]	c_{tet} [Å]	a_{cub} [Å]	$E_{cub}-E_{tet}$ [eV per 4 atoms]	Phase	m_{tot} [μ_B per 4 atoms]	Formula for 4-atom cells along z-axis	$m_{(O)}$ [μ_B]	$m_{(T)}$ [μ_B]	$m_{(T)}$ [μ_B]
0	Mn_3Ge	Reg=Inv	3.73	7.09	5.74	0.10	Tet	1.01		-2.70	1.88	1.88
							Cub	1.00		2.60	-0.86	-0.86
0.25	$Mn_{2.75}Co_{0.25}Ge$	$Mn_2CoGe:Inv$	3.73	7.05	5.74	0.07	Tet	0.49	Mn_3Ge cell	-2.68	1.79	1.86
									Mn_3Ge cell	-2.67	1.86	1.84
									Mn_3Ge cell	-2.68	1.79	1.86
							Cub	1.5	Mn_2CoGe cell	-2.71	2.18	-0.21
									Mn_3Ge cell	2.64	-0.79	-0.83
									Mn_3Ge cell	2.59	-0.97	-0.78
Mn_3Ge cell	2.59	-0.79	-0.78									
Mn_2CoGe cell	2.59	-0.75	0.79									
0.5	$Mn_{2.5}Co_{0.5}Ge$	$Mn_2CoGe:Inv$	3.73	7.01	5.74	0.04	Tet	0.01	Mn_3Ge cell	-2.69	1.70	1.85
									Mn_2CoGe cell	-2.67	2.16	-0.20
							Cub	2.00	Mn_3Ge cell	2.59	-0.64	-0.78
									Mn_2CoGe cell	2.63	-0.82	0.79
1	Mn_2CoGe	Inv	3.74	6.88	5.74	0.07	Tet	0.97		2.62	-2.10	0.40
							Cub	3.00		2.70	-0.70	0.90
1.5	$Mn_{1.5}Co_{1.5}Ge$	$Mn_2CoGe:Inv$	-	-	5.74	No Tet	Cub	4.00	Mn_2CoGe cell	2.87	-0.95	0.96
		$MnCo_2Ge:Reg$	-	-	5.74	$MnCo_2Ge$ cell			2.84	1.05	1.05	
2	$MnCo_2Ge$	Reg	-	-	5.74	No Tet	Cub	5.00		2.95	0.99	0.99

TABLE 6.1: Structure type, lattice constants, stability energy, total magnetic moment per $Mn_{3-x}Co_xGe$ formula unit (considering 4 atoms), and magnetic moment, m , of individual Mn and Co atoms. Individual m values refer to atoms of Co if highlighted in bold characters, and Mn if otherwise. Magnetic moments $m_{(O)}$ and $m_{(T)}$ specify individual atoms located at octahedrally-coordinated (layer with the main group Ge atoms) and tetrahedrally-coordinated sites, respectively, in the indicated 4-atom cells [138].

Table 6.1 summarizes the ground state structure and the corresponding magnetic state for both the cubic and tetragonal structures. In some cases no metastable tetragonal state was found. The minimum energy configuration was found to be tetragonal for Mn_3Ge , tetragonal-inverse for Mn_2CoGe , and cubic-regular for $MnCo_2Ge$. The minimal energy configuration for 8 and 16 atoms in the unit cell corresponded to stacking of the 4-atom unit cells along the z axis. Thus, for $x = 0.5$, the ground state was composed of a tetragonal-inverse Mn_2CoGe unit cell placed above a tetragonal Mn_3Ge unit cell. For $x = 0.25$, the ground state consisted of a tetragonal-inverse Mn_2CoGe unit cell placed above three tetragonal Mn_3Ge unit cells. Finally, for $x = 1.5$, the ground state was composed of the

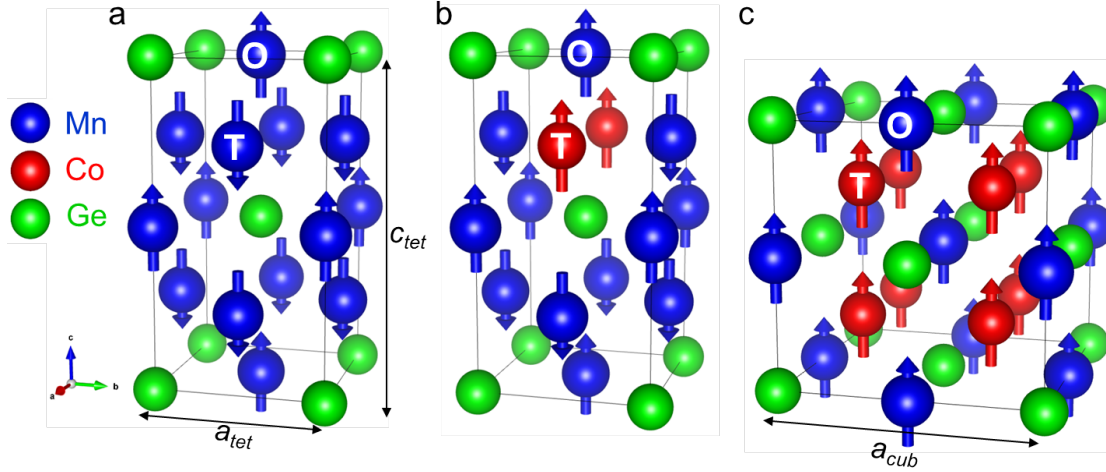


FIGURE 6.1: Examples of crystal structure of (a) tetragonal- Mn_3Ge , (b) tetragonal- $Mn_{2.5}Co_{0.5}Ge$ and (c) cubic- $MnCo_2Ge$. a_{tet} , c_{tet} and a_{cub} describe the tetragonal and cubic lattice constants, respectively. The tetragonal unit cell can be derived from the cubic one by means of a 45° in-plane rotation ($a_{cub} = \sqrt{2} \cdot a_{tet}$), and an elongation along the c axis. Note that the direction of the Mn and Co spins were chosen such that the unit cell's net magnetic moment is positive along the $-c$ axis in (a) and (b), and along the $+c$ axis in (c). The white O and T letters refer to randomly chosen examples of octahedrally-coordinated and tetrahedrally-coordinated sites within each unit cell. The atoms size is not to scale [138].

cubic-inverse Mn_2CoGe unit cell placed above the cubic-regular $MnCo_2Ge$ unit cell. The calculations showed that the ground state remained tetragonal for x up to and including 1. For $x > 1$ the ground state became cubic. For the cubic phases, the magnetic moment was found to satisfy the Slater-Pauling rule [139, 140, 141] for all x values that were studied. The Slater-Pauling rule states that the magnetic moment, m in μ_B , per 4-atom unit cell varies as the number of the valence electrons, N_V , per 4-atom unit cell: $m = N_V - 24$.

The individual calculated moments of the Mn and Co atoms on the octahedrally-coordinated (O) and the two tetrahedrally-coordinated (T) sites (see Fig. 6.1) are shown in Table 6.1. For all the compositions shown, the O site was always

preferentially occupied by Mn in agreement with the “lightest atom” rule [90]. Furthermore, the magnitude of the moment of the Mn atom at this site was robust and slightly changed with Co composition. The sign of this moment changed according to whether this moment was dominant or not. The moments of the Mn and Co atoms on the T sites changed significantly from the cubic to the tetragonal phase but they took up similar values, independent of the Co content, for each of these phases, within one of 4-atom unit cell building blocks. In both the cubic and tetragonal phases the Co moments (which are on the T sites) are always aligned ferromagnetically with the Mn moment on the O site, while the moment of the Mn atom on the T site is always aligned anti-parallel to the Mn moment on the O site (refer to Fig. 6.1). In the cubic phase the total moment of Mn_3Ge had the same sign as the Mn moment on the O site. When Co was added, it substituted for Mn atoms on a T site whose moments are aligned antiparallel to the total moment so that the net moment increased, following the Slater-Pauling rule. On the other hand in the tetragonal phase, the total moment of Mn_3Ge had the opposite sign of the Mn moment on the O site. Therefore, the addition of Co (again on the T site) initially reduced the total moment, until at $x = 0.5$ the total moment was reduced to zero. Further increases in the Co content then caused the moment to increase.

6.1.1 Influence of Cobalt doping on the Brillouin zone filtering effect

From the partial density of states (pDOS) (see Appendix A), that were calculated from the electronic structure, it was possible to extract a layer-dependent spin

x	Alloy	Ground state	Layer z position	Layer name	m [μ_B]	SP	BZF effect	Half-metallic
0	Mn_3Ge	Tet	0	Mn-Ge	-2.7	-0.63	YES	NO
			0.5	Mn-Mn	3.67	-0.77		
0.25	$Mn_{2.75}Co_{0.25}Ge$	Tet	0	Mn-Ge	-2.68	-0.40	NO	NO
			0.125	Mn-Mn	3.65	-0.68		
			0.25	Mn-Ge	-2.67	-0.63		
			0.375	Mn-Mn	3.7	-0.72		
			0.5	Mn-Ge	-2.68	-0.62		
			0.625	Mn-Mn	3.65	-0.74		
			0.75	Mn-Ge	-2.71	-0.30		
0.875	Mn-Co	1.97	-0.52					
0.5	$Mn_{2.5}Co_{0.5}Ge$	Tet	0	Mn-Ge	-2.69	-0.46	NO	NO
			0.25	Mn-Mn	3.55	-0.75		
			0.5	Mn-Ge	-2.67	-0.54		
			0.75	Mn-Co	1.96	-0.56		
1	Mn_2CoGe	Tet	0	Mn-Ge	2.62	0.50	NO	NO
			0.5	Mn-Co	-1.7	0.85		
1.5	$Mn_{1.5}Co_{1.5}Ge$	Cub	0	Mn-Ge	2.87	1.00	YES	YES
			0.25	Mn-Co	0.01	1.00		
			0.5	Mn-Ge	2.84	1.00		
			0.75	Co-Co	2.1	1.00		
2	$MnCo_2Ge$	Cub	0	Mn-Ge	2.95	1.00	YES	YES
			0.5	Co-Co	1.98	1.00		

TABLE 6.2: Layer-dependent bulk spin polarization for different Co concentrations. The z axis corresponds to the c out-of-plane unit cell axis (refer to Fig. 2.6). Note that for $x = 0, 1, 2$ there are only 2 repeating layers. For each x , the lower energy configuration with lattice parameters from Table 6.1 were used. The values of m were extracted from Table 6.1, while the values of SP were calculated from the partial density of states of Appendix A [138].

polarization SP , defined as follows:

$$SP = [pDOS(maj) - pDOS(min)] / [pDOS(maj) + pDOS(min)],$$

in which $pDOS(maj)$ and $pDOS(min)$ respectively correspond to the majority and minority spin-polarized partial DOS calculated at E_F for each layer of each unit cell, as displayed in Table 6.2. Note that each layer consisted of two atoms. The values of SP shown in the table referred only to the ground state configuration of each system. All the cubic phases, independently from the Co composition,

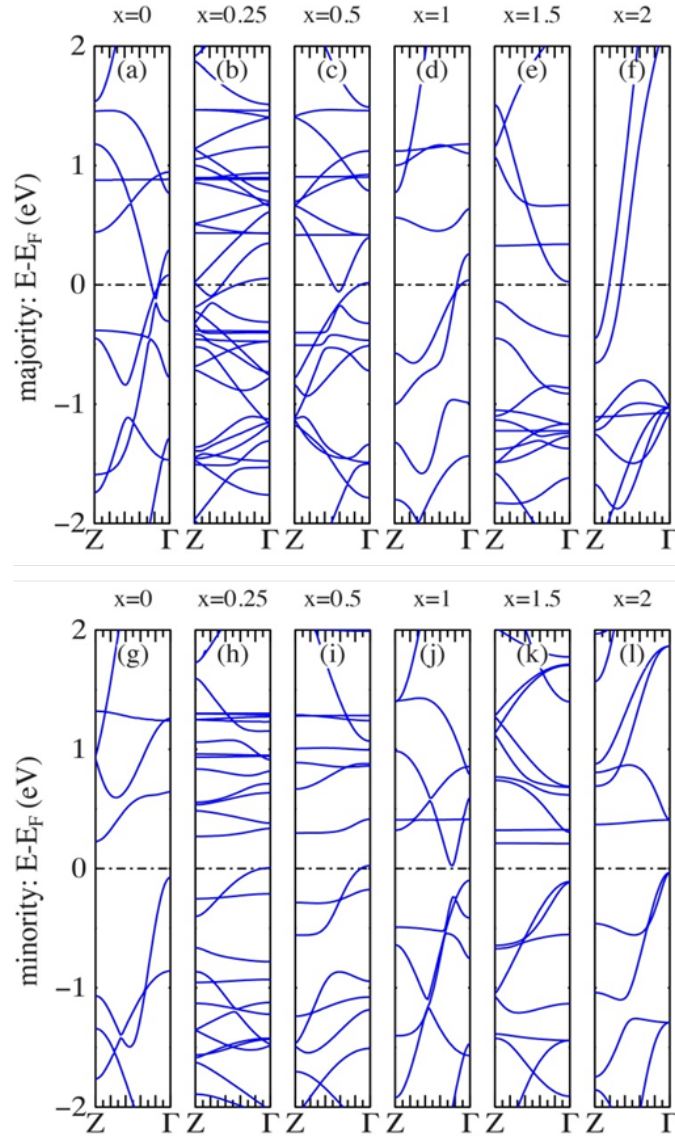


FIGURE 6.2: Majority (a-f) and minority (g-l) electron bands of bulk $Mn_{3-x}Co_xGe$ along the Z- Γ line in the BZ for different Co contents, calculated for the corresponding ground state configuration [138].

displayed a half-metallic behavior, i.e. $SP = 1$. It was also found that the SP of each layer in the unit cell had the same sign for all Co compositions and phases, and that SP was always of the same sign as the moment of Mn at the O site (i.e. at the Mn-Ge layer).

Moreover, the bands structure along the Z- Γ line in the BZ of each $Mn_{3-x}Co_xGe$ system was investigated and it is shown in Fig. 6.2 for the majority (a-f) and minority (g-l) spin channels. In the $x = 0$ case, only the majority electrons of bulk- Mn_3Ge had states crossing the Z- Γ line at E_F thus, for the considerations presented in Chapter 5, Mn_3Ge showed BZF properties. However, for increasing x up to and including 1 (corresponding to compounds still having a tetragonal configuration in the ground state) both \uparrow and \downarrow electron bands had states crossing the Z- Γ line at E_F , thus leading to a suppression of the BZF effect. Cubic $Mn_{1.5}Co_{1.5}Ge$ ($x = 1.5$) and $MnCo_2Ge$ ($x = 2$) compounds displayed a half-metallicity behavior, i.e. the gap in the minority electron bands occurred for DOS evaluated along all the wavevectors k in the 3D BZ (and not only along the Z- Γ line). These results are summarized in Table 6.2.

6.2 Experimental results and comparison with theoretical predictions

6.2.1 Thin films growth method

The samples were grown using the G-system in an Ar environment at a pressure of 3 mTorr. The films stack used for this study was the following: Si(001)/250 Å SiO_2 /200 Å TaN/100 Å IrMn₃/300 Å $Mn_{3-x}Co_xGe$ /30 Å Ta. While the Mn_3Ge ($x = 0$) film was deposited by off-axis sputtering of a Mn_3Ge single target, the $Mn_{3-x}Co_xGe$ ($0 < x \leq 2$) films were grown by co-sputtering of Mn, Co and $Co_{10}Mn_{45}Ge_{45}$ targets. The ratio between the powers used for the Mn and Co targets was varied, while a constant power was used for the $Co_{10}Mn_{45}Ge_{45}$ target. All the $Mn_{3-x}Co_xGe$ layers were deposited using the 3-step process (presented in

Chapter 5): an initial 20 Å $Mn_{3-x}Co_xGe$ layer was deposited at 450 °C, followed by a 280 Å $Mn_{3-x}Co_xGe$ layer grown at 150 °C, with a final in-situ anneal at 450 °C for 1-2 hours in UHV. All the other layers in the stack were deposited at RT.

6.2.2 Structural and magnetic properties variation upon Cobalt doping

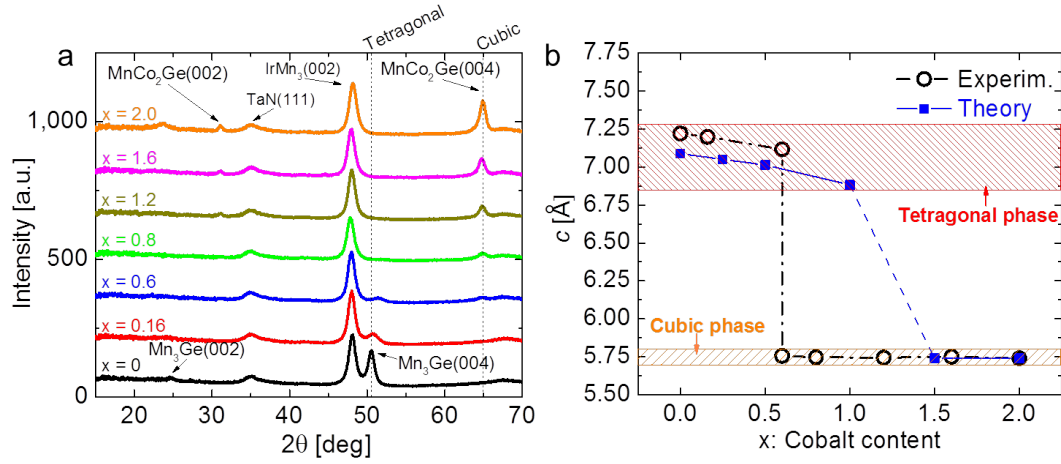


FIGURE 6.3: (a) XRD out-of-plane ω - 2θ scans of 300 Å-thick $Mn_{3-x}Co_xGe$ films. The 'Tetragonal' and 'Cubic' dotted lines are guides for the eyes. (b) The experimental c lattice parameters, extrapolated from (a), are illustrated with black empty circles. The theoretical c lattice constants (taken from Table 6.1) are shown in blue solid squares. The red and orange gridded areas are guides for the eyes [138].

The results from x-ray diffraction measurements carried out on the $Mn_{3-x}Co_xGe$ samples are illustrated in Fig. 6.3a for the different Co concentrations used. When $x = 0$, the Mn_3Ge compound displayed a pure tetragonal structure with a strong (001) texture. Not surprisingly, these results were very similar to those shown for Mn_3Ge films described in Chapter 5. For higher Co concentrations up to and including $x = 0.6$, the tetragonal Bragg reflection with (004) orientation clearly

decreased in intensity, broadening and shifting to higher 2θ angles: this was a clear sign of the decrease of unit cell's c lattice dimension with increasing Co content, as expected from the DFT calculations (see table 6.1). Only for $x = 0.6$ (blue line in Fig. 6.3a), (004) peaks corresponding to both the tetragonal and cubic structures were found, signature of a mixed-phase compound. A further increase in the Co content ($0.6 < x \leq 2$) led to the total disappearance of the tetragonal peak and the stabilization of the cubic phase ($2\theta_{\text{cub-(002)}} \sim 30$ deg and $2\theta_{\text{cub-(004)}} \sim 65$ deg) with the c lattice constant setting around $c_{\text{cub}} (\equiv a_{\text{cub}}) \sim 5.75$ Å. The latter value is in strong agreement with the lattice parameter of L2₁-cubic MnCo₂Ge Heusler previously reported in the literature [142, 143, 144]. These results were summarized in Fig. 6.3b which shows a comparison between the theoretical and experimental c lattice parameters for different x . It turns out that the transition from the tetragonal to the cubic phase in the measured films took place for a concentration of Co that was smaller than what predicted from the theoretical calculations. This is due to a finite degree of atomic disorder in the sputtered films.

Thin films formed from magnetic materials having a tetragonal structure might display uniaxial PMA due to magnetocrystalline anisotropy [104, 119, 145]; instead, if formed from materials having a cubic structure, i.e. with negligible magnetocrystalline anisotropy, they would likely have magnetic moments lying along the plane of the film due to effects induced from shape anisotropy, as explained in Chapter 2. Therefore, it was predictable that the structural evolution of the $Mn_{3-x}Co_xGe$ films from tetragonal to cubic with increasing Co content would cause the magnetic properties of the films to transition from PMA to IMA. This concept was in fact confirmed from the hysteresis loops measured at RT and displayed in Fig. 6.4. The magnetization versus applied field - perpendicular (Fig. 6.4a) and parallel (Fig. 6.4b) to the sample plane - loops are illustrated for different Co

concentrations. In Fig. 6.4a, TD- Mn_3Ge (black line) displays high PMA with large coercive fields, $H_C \sim 3.6$ T, and a low $M_S \sim 100$ emu/cc, reflecting the FiM configuration. While for the $x = 0.16$ film (red line), that still formed with a tetragonal structure (refer to Fig. 6.3a), the magnetization was too low to display a clear hysteresis, the PMA properties of the films with $x > 0.16$ quickly degraded, leading to IMA as expected from the structural change.

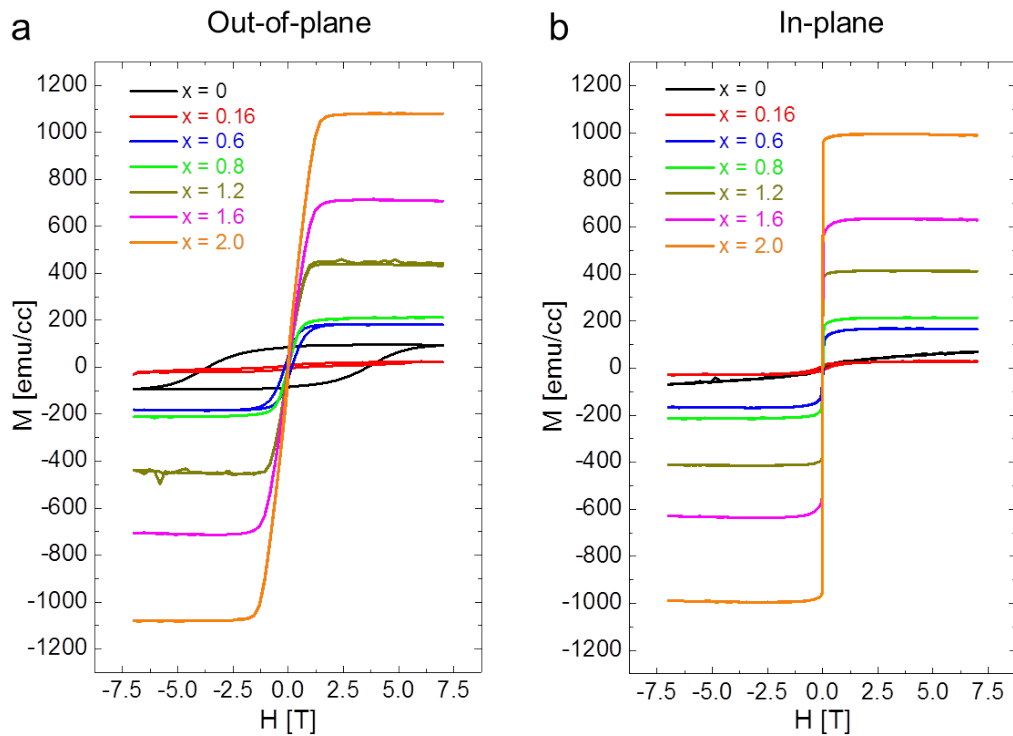


FIGURE 6.4: (a) Out-of-plane and (b) in-plane M vs. H loops of the 300 Å-thick $Mn_{3-x}Co_xGe$ films grown using amorphous Si/SiO₂ substrates, measured using a SQUID-VSM [138].

Fig. 6.5 compares the $Mn_{3-x}Co_xGe$ magnetization variation upon increasing Co content between the theoretical calculations and the experiments. In agreement with the considerations made above while describing Table 6.1, it was found experimentally that the magnetization firstly decreased (from the tetragonal- Mn_3Ge

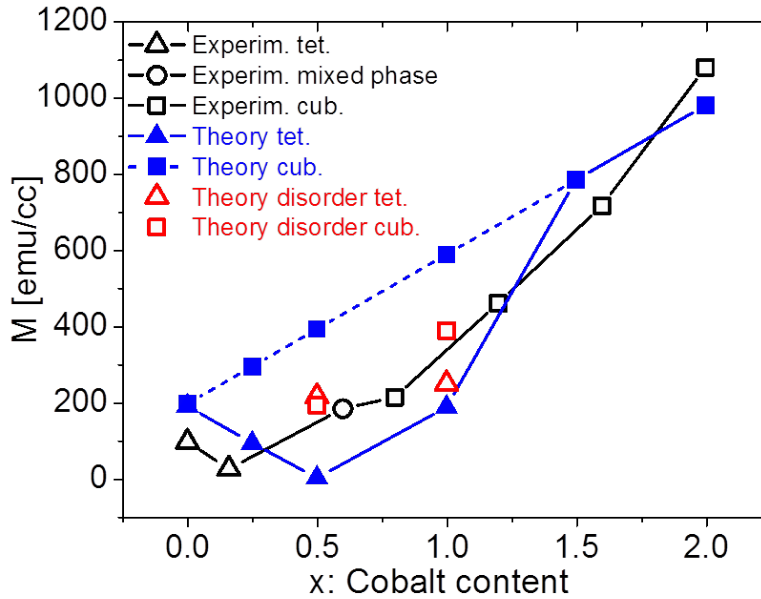


FIGURE 6.5: Experimental (black empty symbols) and theoretically predicted (solid blue symbols) values of magnetization of the $Mn_{3-x}Co_xGe$ system. Triangles and squares refer to tetragonal and cubic structures, respectively, while the circle refers to a mixed phase. The red empty symbols refer to calculations of *disordered* cubic and tetragonal structures (see Tables B.1 and B.2 in Appendix B). The blue solid line connects the values of the magnetization of the ground state configurations, while the dashed line was used as a guide for the eyes to highlight the linear trend of the Slater-Pauling rule for the cubic systems only. The ground state of Mn_3Ge ($x = 0$) was the tetragonal configuration with $m/f.u.$ of 1 Bohr magneton (see Table 6.1); this was a similar value, in module, as in the cubic- Mn_3Ge phase (the two symbols overlapped in the graph). Experimental data were extrapolated from the out-of-plane M vs H hysteresis loops (Fig. 6.4a). The theoretical data were obtained by dividing the calculated magnetic moment per formula unit (in μ_B) by the respective unit cell volume (in cc), and multiplying by the units ($9.27 \cdot 10^{-21}$ emu) and unit cell (2, i.e. the unit cell is composed by twice the number of atoms than the corresponding formula unit) conversion factors [138].

value) approaching 0, and then increased with increasing Co concentrations. For $x = 0.5$, the calculations predicted the ground state configuration to be tetragonal with a total moment equal to zero; however, the magnetization found experimentally for the film with $x = 0.6$ was significantly higher than zero (black empty circle in Fig. 6.5) since this film was shown to have a mixed cubic and tetragonal structure, as illustrated in Fig. 6.3a. In order to explain the discrepancy between the experimental and theoretical trends of M , computational studies of *disordered* $Mn_{3-x}Co_xGe$ structures, i.e. systems with energetically-unfavorable atomic configurations with Co atoms placed not only at T sites but also at O sites [90], for $x = 0.5$ and 1 were performed (see Appendix B). It was found that, in some cases, a *disordered* system could take a magnetization value that is in between those of the cubic and tetragonal configurations of the corresponding 'ordered' system (see the red open symbols in Fig. 6.5 that better fitted with the experimental trend of M). Note that the difference in the stability energy between the 'ordered' cubic and tetragonal configurations for the Co-doped systems (indicated in Table 6.1) was relatively small, in certain cases being close to the energy associated with thermal excitations at RT (0.025 eV). Thus, $Mn_{3-x}Co_xGe$ films with $x \neq 0$ are likely to show some degree of atomic disorder.

Finally, Fig. 6.6a summarizes the dependence of the coercivity (H_C) and the effective field (H_K) of the Heusler films depending on the Co content. The evolution from PMA to IMA reflected in a rapid decrease of the coercivity from the 'hard'- Mn_3Ge case to the 'soft'- $Mn_{3-x}Co_xGe$ cases with $x \geq 0.6$. A similar tendency was observed for H_K , since the MCA of the films decreased accordingly to the structural change. Also, Fig. 6.6b shows that the films roughness did not particularly change with increasing Co concentrations: relatively smooth surfaces ($r_{rms} < 7 \text{ \AA}$) were measured for the complete $Mn_{3-x}Co_xGe$ series.

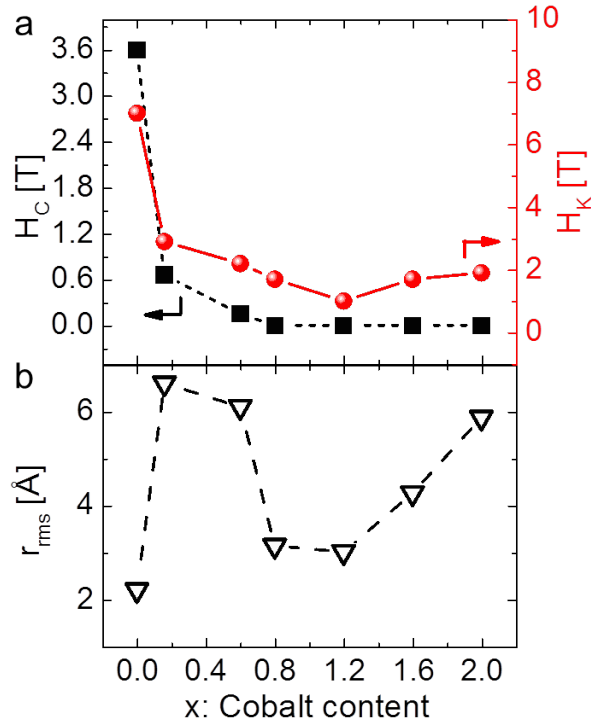


FIGURE 6.6: (a) Coercive field H_C (black squares, left ordinate) and effective field H_K (red balls, right ordinate). H_C was collected from the easy-axis M vs H loops as the magnetic field at which the sample was demagnetized. H_K is usually evaluated from the M vs. H hard-axis loop as the magnetic field at which the magnetization reaches saturation. Note that the magnetization of Mn_3Ge was expected to saturate at high magnetic fields that were not assessable by the measurement tool; therefore, H_K was assumed (as a lower bound) to be 7 T in the $x = 0$ case (refer to Fig. 6.4b). (b) Root-mean-square surface roughness [138].

6.3 Summary

In summary, the evolution of the structural and magnetic properties of a $Mn_{3-x}Co_xGe$ Heusler system was investigated both theoretically and experimentally and compared for different Co concentrations. Both studies confirmed that the system

structure configuration changes from tetragonal to cubic with increasing Co content. This resulted in a transition of the magnetic properties from a ferri-magnetic and PMA character, to a ferro-magnetic and IMA character. The experimental results were shown to be in good agreement with the theoretical predictions for both 'ordered' and 'disordered' systems.

A theoretical study of the electronic properties of the $Mn_{3-x}Co_xGe$ system showed that the Brillouin zone filtering effect, which was responsible for the sign change of the tunneling spin polarization of the Mn-Mn layer in the case of ($x = 0$) Mn_3Ge (hence compensating the tunneling magnetoresistance), could be eliminated by doping the compound with Co. Additionally, for all x contents, the layer-dependent spin polarizations of each compound were predicted to have the same sign. This means that the tunneling (through a MgO barrier) of spin-polarized electrons from different termination layers forming these compounds (with $x > 0$) would not be compensated.

Chapter 7

Conclusions

The research performed in this dissertation was aimed at finding and developing novel magnetic materials that could potentially fulfill the key material requirements of large perpendicular magnetic anisotropy, low magnetization, high spin polarization and low damping for perpendicular spin-transfer-torque magnetic random access memory applications.

Given these prerequisites, this work has primarily focused on the investigation of the tetragonally-distorted Mn_3Ge Heusler compound. A method to grow highly textured Mn_3Ge Heusler films displaying low magnetic moment and giant perpendicular magnetic anisotropy with coercive fields up to 6 T on amorphous substrates was shown, thereby opening a path to their potential use for many applications such as magnetic recording media and rare-earth free hard magnets. The uniaxial perpendicular anisotropy of the Mn_3Ge films was promoted by the 'broken' symmetry of the tetragonal structure and not by interface-driven effects, like in the case of CoFeB thin films that are commonly used in perpendicular MTJs.

However, in Mn₃Ge-based perpendicular magnetic tunnel junctions it was found that the tunneling magnetoresistance was strongly influenced by unavoidable atomic steps in the Mn₃Ge morphology at the MgO tunnel barrier interface (Mn-Mn and Mn-Ge termination layers). It was shown from theoretical calculations of the transmission functions of a Mn₃Ge/MgO/Fe MTJ system that the Mn-Mn and Mn-Ge termination layers, having opposite magnetization, display opposite tunneling spin polarization, therefore they compensate one another leading to low negative TMR, in agreement with the experimental findings.

This effect was rationalized as the consequence of a delicate balance between two opposing mechanisms that take place in such tunnel junctions. One is the Brillouin zone filtering effect arising at the Mn₃Ge/MgO interface which allowed the coupling of *majority* Mn₃Ge electrons with specific orbital symmetries at the Fermi energy along the Γ -Z line of the 2D BZ with electronic states within the MgO band gap with Δ_1 symmetry and smallest attenuation constant; instead, *minority* Mn₃Ge electrons do not couple to these Δ_1 states of MgO and their contribution to transmission is then suppressed. Hence, an *increase* in magnitude of the TMR for both Mn-Mn and Mn-Ge terminations for increasing thicknesses of the MgO spacer is observed. On the other hand, the negative bulk spin polarization of Mn₃Ge enhances the tunneling of *minority* electrons in both Mn-Mn and Mn-Ge terminations independently of the MgO thickness, thus favoring a *negative* TMR. Note that if the contribution of the Brillouin zone filtering effect was to be suppressed, the TMR, which would then only depend on the spin polarization of Mn₃Ge, would be of the same (negative) sign for both termination layers and would not be compensated.

Therefore, the second part of this work aimed at modifying the electronic properties of Mn₃Ge by doping it with increasing concentrations of Co (Mn_{3-x}Co_xGe with $0 \leq x \leq 2$), in order to eliminate the Brillouin zone filtering effect while

maintaining the tetragonal structure (to still guarantee the PMA requirement for p-MTJs) and the ferrimagnetic configuration (to still guarantee the low magnetic moment requirement for p-MTJs).

It was indeed proved from DFT calculations of the electronic properties of the $\text{Mn}_{3-x}\text{Co}_x\text{Ge}$ system that the Brillouin zone filtering mechanism can be easily eliminated using Co concentrations in the $0 < x \leq 1$ range. Also, within this range, each compound was predicted to be tetragonal in the ground state, with each constituting layer having same sign of spin polarization. In contrast, for $x > 1$ all the compounds were predicted to crystallize with a cubic structure and to be half-metallic (i.e. 100% positive spin polarization for the entire 3D Fermi surface and not only along the Z- Γ line). However, experimental studies of the structural and magnetic properties of $\text{Mn}_{3-x}\text{Co}_x\text{Ge}$ thin films showed that the transition from the tetragonal to the cubic structure took place already for concentrations close to $x \sim 0.6$, in which a mixed tetragonal and cubic phase was observed. For $x > 0.6$, all the $\text{Mn}_{3-x}\text{Co}_x\text{Ge}$ films crystallized with a cubic structure. The discrepancy between the structural properties found from calculations and experiments is due to a finite degree of atomic disorder within the sputtered films.

Nonetheless, it was demonstrated that a film with a small amount of Co ($x = 0.16$) had a tetragonal structure with a magnetic moment close to zero, in agreement with the theoretical predictions. This compound had the advantageous prerequisites to be a good candidate for p-MTJs, but unfortunately this was not tested. Future studies could focus on the investigation of the tunneling magnetoresistance in junction devices formed using this compound as ferrimagnetic electrode and MgO as insulating barrier. The purpose would be to experimentally verify whether the Brillouin zone filtering effect can indeed be eliminated using this Heusler compound instead of Mn_3Ge , in the hope of demonstrating large TMR ratios at room temperature. These studies would be of significant interest not

only to understand their fundamental physics but also for technologically-relevant application purposes.

This work has provided a roadmap for finding novel materials that can potentially enhance the performances of spin transfer torque magnetic random access memories. The properties of these materials, that can be identified by the use of computational techniques, might altogether fulfill all the main material requirements for such application. I personally believe in the potentiality of STT-MRAM to cover a broad spectrum of applications and I am excited about the perspective of seeing it - in the near future - integrated in many everyday technological devices which most people, throughout the world, could afford and take advantage of. The idea of conducting high-impact research applied to the development of new memories or devices on a mass-production scale has struck me and it always will.

Appendix A

Calculations of layer-dependent density of states of the $\text{Mn}_{3-x}\text{Co}_x\text{Ge}$ systems

In this section, the partial density of states (pDOS) of the $\text{Mn}_{3-x}\text{Co}_x\text{Ge}$ systems, that were obtained from studies of their electronic structure for $x = 0, 0.25, 0.5, 1, 1.5,$ and $2,$ are shown. These calculations were carried out following the same criteria and considerations presented in section 6.1. The lattice constants of the ground state structure configuration used for each x were taken from Table 6.1. In the following figures, each plot displays the DOS of the majority (upper panel) and minority (lower panel) electron bands for the layers forming the $\text{Mn}_{3-x}\text{Co}_x\text{Ge}$ compounds.

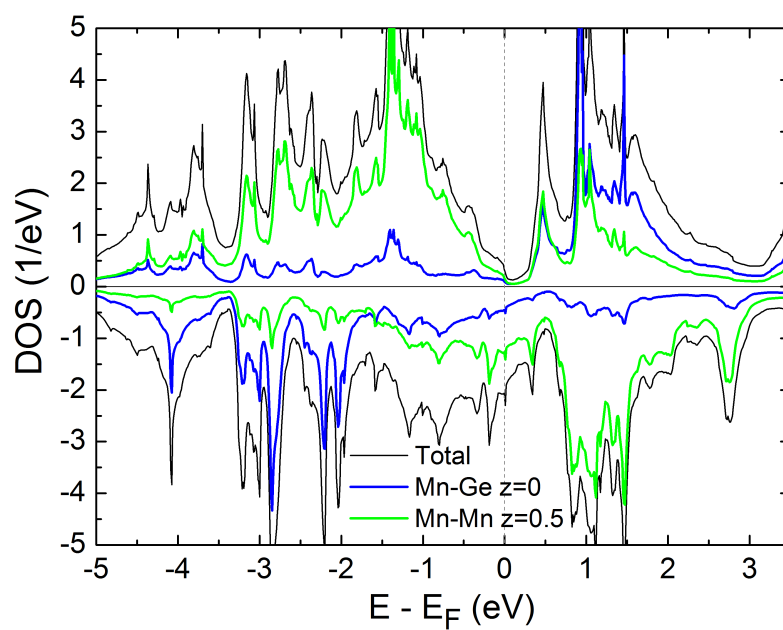
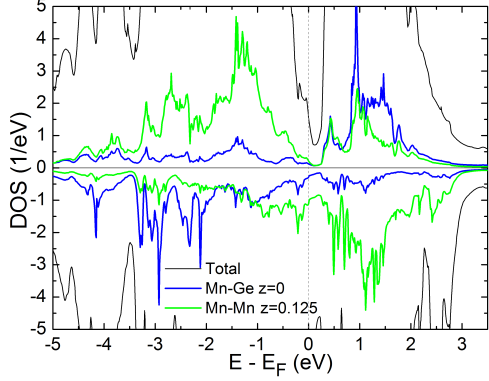
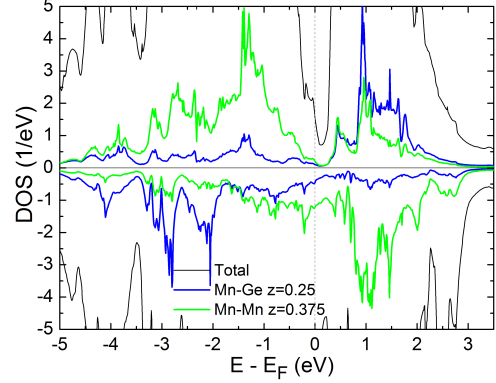


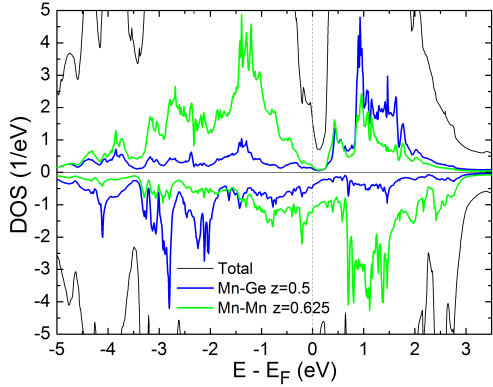
FIGURE A.1: Layer-dependent DOS of bulk Mn_3Ge calculated for its ground state configuration (tetragonal). Both Mn-Ge and Mn-Mn layers had more states at E_F within the minority spin channel than in the majority one. Thus, this compound was not half-metallic and showed negative spin polarization for both layers, as shown in Table 6.2 [138].



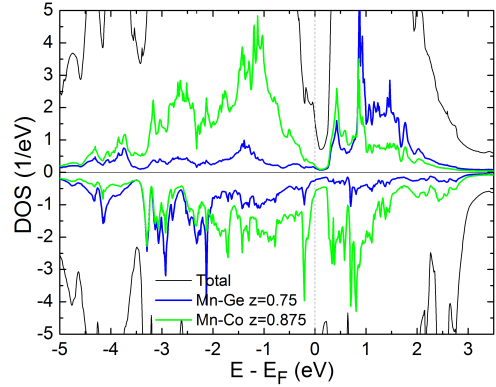
(A) Layer-dependent DOS of the $z=0$ and $z=0.125$ layers of bulk $Mn_{2.75}Co_{0.25}Ge$ calculated for its ground state configuration (tetragonal). Both Mn-Ge and Mn-Mn layers had more states at E_F within the minority spin channel than in the majority one. Thus, these layers showed negative spin polarization, as shown in Table 6.2.



(B) Layer-dependent DOS of the $z=0.25$ and $z=0.375$ layers of bulk $Mn_{2.75}Co_{0.25}Ge$ calculated for its ground state configuration (tetragonal). Both Mn-Ge and Mn-Mn layers had more states at E_F within the minority spin channel than in the majority one. Thus, these layers showed negative spin polarization, as shown in Table 6.2.

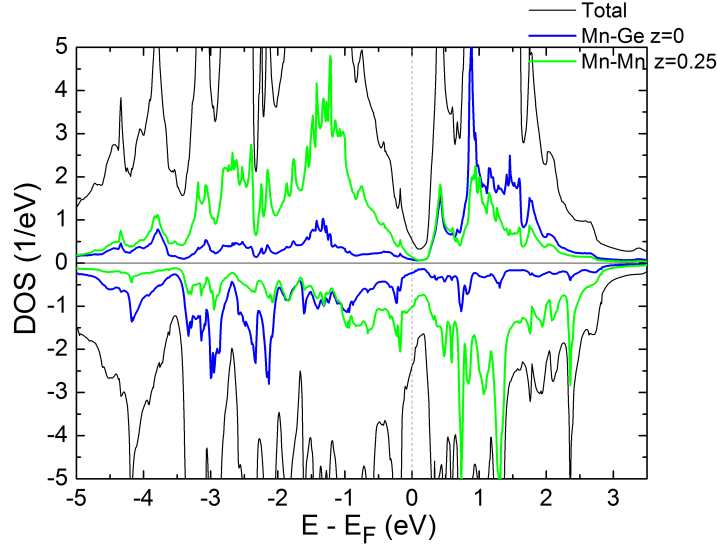


(C) Layer-dependent DOS of the $z=0.5$ and $z=0.625$ layers of bulk $Mn_{2.75}Co_{0.25}Ge$ calculated for its ground state configuration (tetragonal). Both Mn-Ge and Mn-Mn layers had more states at E_F within the minority spin channel than in the majority one. Thus, these layers showed negative spin polarization, as shown in Table 6.2.

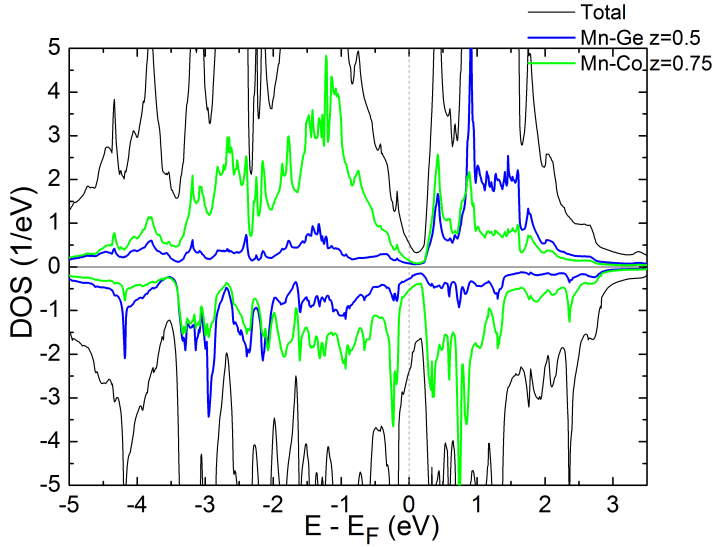


(D) Layer-dependent DOS of the $z=0.75$ and $z=0.875$ layers of bulk $Mn_{2.75}Co_{0.25}Ge$ calculated for its ground state configuration (tetragonal). Both Mn-Ge and Mn-Co layers had more states at E_F within the minority spin channel than in the majority one. Thus, these layers showed negative spin polarization, as shown in Table 6.2. Considering (A), (B), (C), and (D) together the $Mn_{2.75}Co_{0.25}Ge$ compound was found not to be half-metallic.

FIGURE A.2: Layer-dependent DOS of $Mn_{2.75}Co_{0.25}Ge$



(A) Layer-dependent DOS of the $z=0$ and $z=0.25$ layers of bulk $Mn_{2.5}Co_{0.5}Ge$ calculated for its ground state configuration (tetragonal). Both Mn-Ge and Mn-Mn layers had more states at E_F within the minority spin channel than in the majority one. Thus, these layers showed negative spin polarization, as shown in Table 6.2.



(B) Layer-dependent DOS of the $z=0.5$ and $z=0.75$ layers of bulk $Mn_{2.5}Co_{0.5}Ge$ calculated for its ground state configuration (tetragonal). Both Mn-Ge and Mn-Co layers had more states at E_F within the minority spin channel than in the majority one. Thus, these layers showed negative spin polarization, as shown in Table 6.2. Considering (A) and (B) together the $Mn_{2.5}Co_{0.5}Ge$ compound was found not to be half-metallic.

FIGURE A.3: Layer-dependent DOS of $Mn_{2.5}Co_{0.5}Ge$

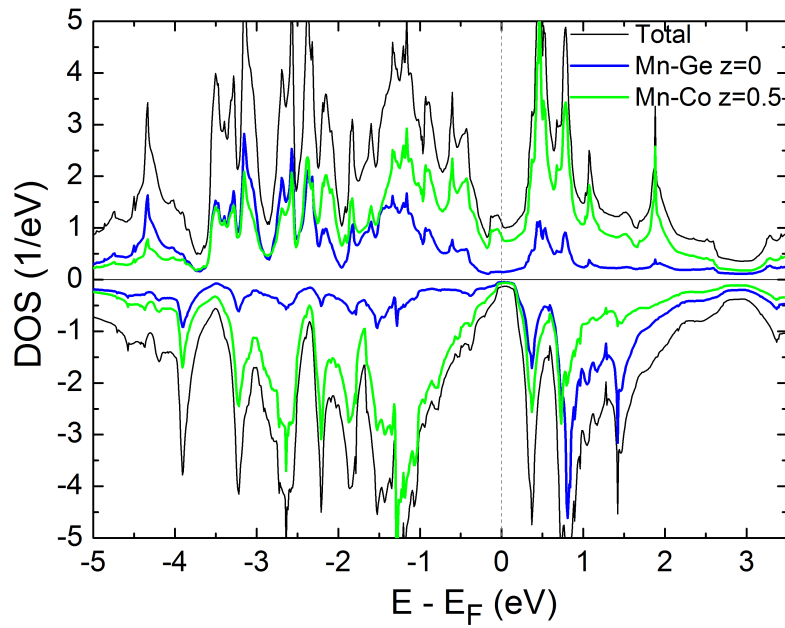
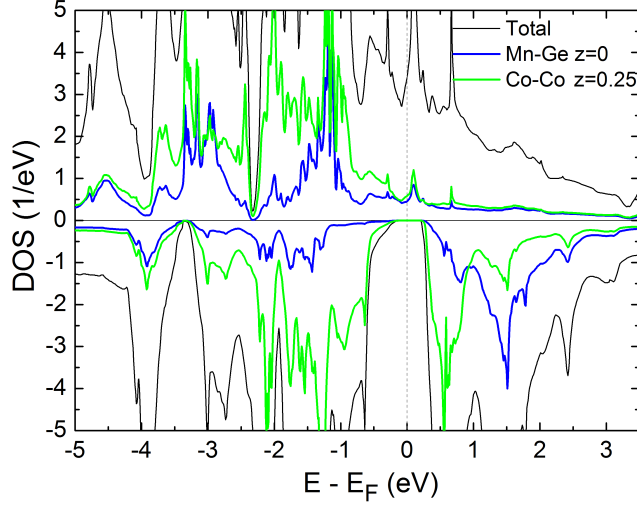
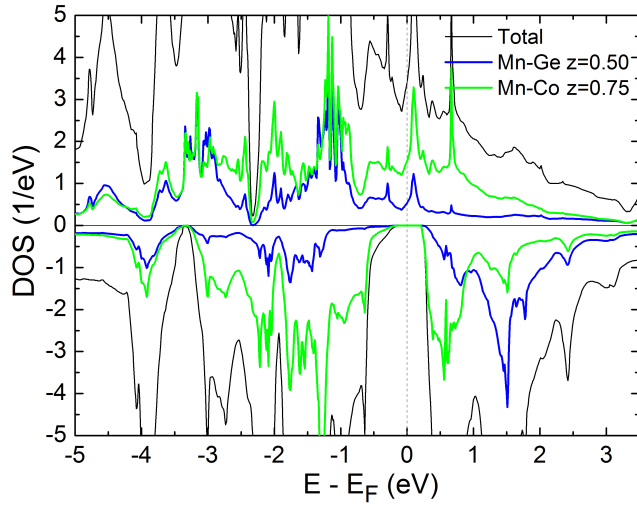


FIGURE A.4: Layer-dependent DOS of bulk Mn_2CoGe calculated for its ground state configuration (tetragonal). Both Mn-Ge and Mn-Co layers have more states at E_F within the majority spin channel than in the minority one. Thus, this compound is not half-metallic and shows positive spin polarization for both layers, as shown in Table 6.2 [138].



(A) Layer-dependent DOS of the $z=0$ and $z=0.25$ layers of bulk $Mn_{1.5}Co_{1.5}Ge$ calculated for its ground state configuration (cubic). Both Mn-Ge and Co-Co layers had states at E_F only within the majority spin channel, and none within the minority one. Thus, these layers showed positive spin polarization, as shown in Table 6.2.



(B) Layer-dependent DOS of the $z=0.5$ and $z=0.75$ layers of bulk $Mn_{2.5}Co_{0.5}Ge$ calculated for its ground state configuration (cubic). Both Mn-Ge and Mn-Co layers had states at E_F only within the majority spin channel, and none within the minority spin channel. Thus, these layers showed positive spin polarization, as shown in Table 6.2. Considering (A) and (B) together the $Mn_{2.5}Co_{0.5}Ge$ compound was found to be half-metallic with $SP = 1$.

FIGURE A.5: Layer-dependent DOS of $Mn_{1.5}Co_{1.5}Ge$

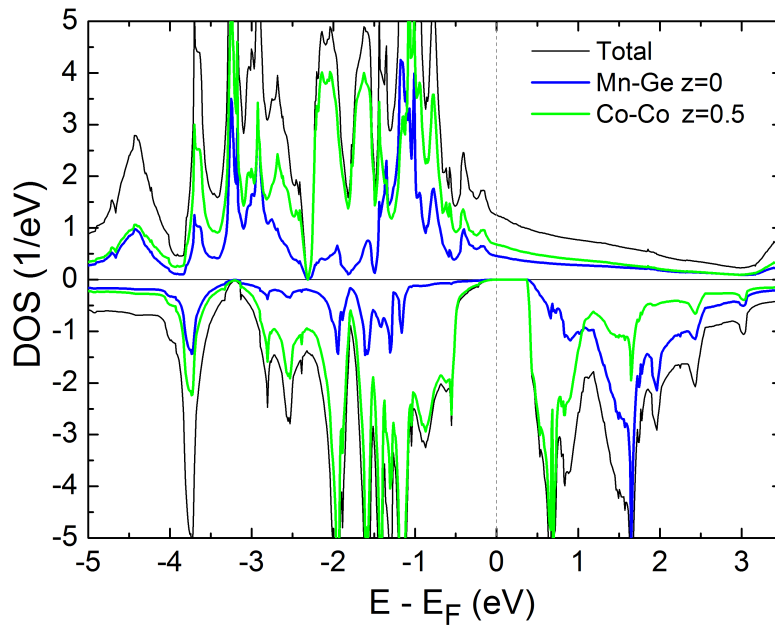


FIGURE A.6: Layer-dependent DOS of bulk $MnCo_2Ge$ calculated for its ground state configuration (cubic). Both Mn-Ge and Co-Co layers have states at E_F only within the majority spin channel, and none within the minority spin channel. Thus, this compound is half-metallic with $SP = 1$, as shown in Table 6.2 [138].

Appendix B

Calculations of disordered $\text{Mn}_{3-x}\text{Co}_x\text{Ge}$ systems

$$x = 0.5$$

In this section the influence of atomic disorder on the energy configuration and magnetic moment of a $\text{Mn}_{2.5}\text{Co}_{0.5}\text{Ge}$ system was investigated. Each crystal structure considered here was defined by 4 unit cells stacked on top of each other, from unit cell 1 (bottom) to 4 (top). The total number of atoms used was 16, with each unit cell consisting of 4 atoms. The theoretical calculations were carried out for many different atomic configurations, with Ge atoms always fixed at octahedral positions, Ge(O'), while the position of the 2 Co atoms (highlighted in bold in Table B.1) were varied. The theoretical lattice parameters used are $a = 3.73 \text{ \AA}$ and $c = 7.0124 \text{ \AA}$ for the tetragonal phase and $a = 5.752 \text{ \AA}$ for the cubic phase (taken from Table 6.1).

Unit cell 1	Unit cell 2	Unit cell 3	Unit cell 4	Structure	E_{tot} [meV]	m_{tot} [μ_B per 4 atoms]
Mn ₃ Ge	Mn ₃ Ge	Mn ₃ Ge	Co(T)Co(T') Mn(O)Ge(O')	Tet	-125.017	-0.161
				Cub	-125.085	-2
Mn ₃ Ge	Mn ₃ Ge	Co(T)Mn(T') Mn(O)Ge(O')	Mn(T) Co(T') Mn(O)Ge(O')	Tet	-125.142	0.003
				Cub	-124.942	-2
Mn ₃ Ge	Mn ₃ Ge	Mn(T) Co(T') Mn(O)Ge(O')	Mn(T) Co(T') Mn(O)Ge(O')	Tet	-125.085	0.008
				Cub	-124.956	-2
Mn ₃ Ge	Co(T)Mn(T') Mn(O)Ge(O')	Mn ₃ Ge	Mn(T) Co(T') Mn(O)Ge(O')	Tet	-125.127	-0.013
				Cub	-124.981	-2
Mn ₃ Ge	Mn(T) Co(T') Mn(O)Ge(O')	Mn ₃ Ge	Mn(T) Co(T') Mn(O)Ge(O')	Tet	-125.135	-0.015
				Cub	-124.976	-2
Mn ₃ Ge	Mn ₃ Ge	Mn ₃ Ge	Co(T)Mn(T') Co(O) Ge(O')	Tet	-124.707	1.135
				Cub	-123.947	-0.99
Mn ₃ Ge	Mn ₃ Ge	Mn ₃ Ge	Mn(T) Co(T') Co(O) Ge(O')	Tet	-124.707	1.135
				Cub	-123.947	-0.99
Mn ₃ Ge	Mn ₃ Ge	Co(T)Mn(T) Mn(O)Ge(O')	Mn(T)Mn(T') Co(O) Ge(O')	Tet	-124.707	1.135
				Cub	-123.947	-0.99
Mn ₃ Ge	Mn ₃ Ge	Mn(T)Mn(O) Co(T') Ge(O')	Mn(T)Mn(T') Co(O) Ge(O')	Tet	-124.707	1.135
				Cub	-123.947	-0.99
Mn ₃ Ge	Co(T)Mn(T') Mn(O)Ge(O')	Mn ₃ Ge	Mn(T)Mn(T') Co(O) Ge(O')	Tet	-124.756	1.128
				Cub	-123.955	-0.97
Mn ₃ Ge	Mn(T) Co(T') Mn(O)Ge(O')	Mn ₃ Ge	Mn(T)Mn(T') Co(O) Ge(O')	Tet	-124.756	1.128
				Cub	-123.955	-0.97
Mn ₃ Ge	Mn ₃ Ge	Mn(T)Mn(T') Co(O) Ge(O')	Mn(T)Mn(T') Co(O) Ge(O')	Tet	-124.362	2.115
				Cub	-123.927	0.025
Mn ₃ Ge	Mn(T)Mn(T') Co(O) Ge(O')	Mn ₃ Ge	Mn(T)Mn(T') Co(O) Ge(O')	Tet	-123.766	2.808
				Cub	-122.89	0.883

TABLE B.1: Energy configuration and magnetic moment of a *disordered* $Mn_{2.5}Co_{0.5}Ge$ system. The values of m_{tot} highlighted in bold correspond to the ones shown in Fig. 6.5 with red open symbols [138].

$$\mathbf{x} = \mathbf{1}$$

In this section the influence of atomic disorder on the energy configuration and magnetic moment of a Mn_2CoGe system was investigated. Each crystal structure considered here was defined by 4 unit cells stacked on top of each other, from unit cell 1 (bottom) to 4 (top). The total number of atoms used was 16, with each unit cell consisting of 4 atoms. The theoretical calculations were carried out for many different atomic configurations, with Ge atoms always fixed at octahedral positions, Ge(O'), while the position of the 2 Co atoms (highlighted in bold in Table B.2) were varied. The theoretical lattice parameters used are $a = 3.74 \text{ \AA}$ and $c = 6.8816 \text{ \AA}$ for the tetragonal phase and $a = 5.742 \text{ \AA}$ for the cubic phase (taken from Table 6.1).

Unit cell 1	Unit cell 2	Unit cell 3	Unit cell 4	Structure	E_{tot} [meV]	m_{tot} [μ_B per 4 atoms]
Mn(T)Co(T')Mn(O)Ge(O')	Mn(T)Co(T')Mn(O)Ge(O')	Mn ₃ Ge	Co(T)Co(T')Mn(O)Ge(O')	Tet	-121.076	-1.07
				Cub	-121.328	-3
Mn(T)Co(T')Mn(O)Ge(O')	Mn(T)Co(T')Mn(O)Ge(O')	Co(T)Mn(T')Mn(O)Ge(O')	Mn(T)Co(T')Mn(O)Ge(O')	Tet	-121.144	-0.965
				Cub	-121.100	-3
Mn(T)Co(T')Mn(O)Ge(O')	Mn(T)Co(T')Mn(O)Ge(O')	Mn(T)Co(T')Mn(O)Ge(O')	Mn(T)Co(T')Mn(O)Ge(O')	Tet	-121.016	-0.95
				Cub	-121.158	-3
Mn(T)Co(T')Mn(O)Ge(O')	Co(T)Mn(T')Mn(O)Ge(O')	Mn(T)Co(T')Mn(O)Ge(O')	Mn(T)Co(T')Mn(O)Ge(O')	Tet	-121.144	-0.965
				Cub	-121.100	-3
Mn(T)Co(T')Mn(O)Ge(O')	Co(T)Mn(T')Mn(O)Ge(O')	Mn ₃ Ge	Co(T)Mn(T')Co(O)Ge(O')	Tet	-120.753	0.253
				Cub	-120.159	-1.653
Mn(T)Co(T')Mn(O)Ge(O')	Mn(T)Co(T')Mn(O)Ge(O')	Mn ₃ Ge	Mn(T)Co(T')Co(O)Ge(O')	Tet	-120.683	0.3
				Cub	-120.198	-1.988
Mn(T)Co(T')Mn(O)Ge(O')	Mn(T)Co(T')Mn(O)Ge(O')	Co(T)Mn(T')Mn(O)Ge(O')	Mn(T)Mn(T')Co(O)Ge(O')	Tet	-120.753	0.253
				Cub	-120.160	-1.66
Mn(T)Co(T')Mn(O)Ge(O')	Mn(T)Co(T')Mn(O)Ge(O')	Mn(T)Co(T')Mn(O)Ge(O')	Mn(T)Mn(T')Co(O)Ge(O')	Tet	-120.683	0.3
				Cub	-120.199	-1.98
Mn(T)Co(T')Mn(O)Ge(O')	Co(T)Mn(T')Mn(O)Ge(O')	Mn(T)Co(T')Mn(O)Ge(O')	Mn(T)Mn(T')Co(O)Ge(O')	Tet	-120.798	0.245
				Cub	-120.120	-1.615
Mn(T)Co(T')Mn(O)Ge(O')	Mn(T)Co(T')Mn(O)Ge(O')	Mn(T)Co(T')Mn(O)Ge(O')	Mn(T)Mn(T')Co(O)Ge(O')	Tet	-120.683	0.3
				Cub	-120.199	-1.98
Mn(T)Co(T')Mn(O)Ge(O')	Mn(T)Co(T')Mn(O)Ge(O')	Mn(T)Mn(T')Co(O)Ge(O')	Mn(T)Mn(T')Co(O)Ge(O')	Tet	-120.270	1.168
				Cub	-120.077	-0.97
Mn(T)Co(T')Mn(O)Ge(O')	Mn(T)Mn(T')Co(O)Ge(O')	Mn(T)Co(T')Mn(O)Ge(O')	Mn(T)Mn(T')Co(O)Ge(O')	Tet	-120.158	0.638
				Cub	-119.223	-0.97
Mn(T)Co(T')Mn(O)Ge(O')	Mn ₃ Ge	Mn(T)Co(T')Mn(O)Ge(O')	Co(T)Co(T')Mn(O)Ge(O')	Tet	-121.112	-1.078
				Cub	-121.307	-3
Mn(T)Co(T')Mn(O)Ge(O')	Mn ₃ Ge	Mn(T)Co(T')Mn(O)Ge(O')	Co(T)Mn(T')Co(O)Ge(O')	Tet	-120.755	0.115
				Cub	-120.161	-1.313
Mn(T)Co(T')Mn(O)Ge(O')	Mn ₃ Ge	Mn(T)Co(T')Mn(O)Ge(O')	Mn(T)Co(T')Co(O)Ge(O')	Tet	-120.705	0.46
				Cub	-120.178	-1.848
Co(T)Co(T')Mn(O)Ge(O')	Mn ₃ Ge	Mn ₃ Ge	Co(T)Co(T')Mn(O)Ge(O')	Tet	-120.974	-1.265
				Cub	-121.465	-3
Mn ₃ Ge	Co(T)Co(T')Mn(O)Ge(O')	Mn ₃ Ge	Co(T)Co(T')Mn(O)Ge(O')	Tet	-121.007	-1.293
				Cub	-121.517	-3
Mn(T)Co(T')Mn(O)Ge(O')	Co(T)Mn(T')Mn(O)Ge(O')	Mn(T)Co(T')Mn(O)Ge(O')	Co(T)Mn(T')Mn(O)Ge(O')	Tet	-121.261	-0.978
				Cub	-120.984	-3

TABLE B.2: Energy configuration and magnetic moment of a *disordered* Mn_2CoGe system. The values of m_{tot} highlighted in bold correspond to the ones shown in Fig. 6.5 with red open symbols [138].

Bibliography

- [1] M. A. Omar, *Elementary Solid State Physics: Principles and Applications*. Addison-Wesley Publishing Company, 1993.
- [2] C. Chappert, A. Fert, and F. Van Dau, “The emergence of spin electronics in data storage,” *Nanoscience and Technology*, p. 147, 2007.
- [3] J. M. D. Coey, *Magnetism and magnetic materials*. Cambridge; New York: Cambridge University Press, 2009.
- [4] S. A. Wolf, “Spintronics: A Spin-Based Electronics Vision for the Future,” *Science*, vol. 294, pp. 1488–1495, Nov. 2001.
- [5] M. N. Baibich, J. M. Broto, A. Fert, F. N. Van Dau, F. Petroff, P. Etienne, G. Creuzet, A. Friederich, and J. Chazelas, “Giant Magnetoresistance of (001)Fe/(001)Cr Magnetic Superlattices,” *Physical Review Letters*, vol. 61, pp. 2472–2475, Nov. 1988.
- [6] G. Binasch, P. Grünberg, F. Saurenbach, and W. Zinn, “Enhanced magnetoresistance in layered magnetic structures with antiferromagnetic interlayer exchange,” *Physical Review B*, vol. 39, pp. 4828–4830, Mar. 1989.
- [7] M. Julliere, “Tunneling between ferromagnetic films,” *Physics Letters A*, vol. 54, pp. 225–226, Sept. 1975.

-
- [8] J. S. Moodera, L. R. Kinder, T. M. Wong, and R. Meservey, "Large Magnetoresistance at Room Temperature in Ferromagnetic Thin Film Tunnel Junctions," *Physical Review Letters*, vol. 74, pp. 3273–3276, Apr. 1995.
- [9] T. Miyazaki and N. Tezuka, "Spin polarized tunneling in ferromagnet/insulator/ferromagnet junctions," *Journal of Magnetism and Magnetic Materials*, vol. 151, pp. 403–410, Dec. 1995.
- [10] A. D. Kent and D. C. Worledge, "A new spin on magnetic memories," *Nature nanotechnology*, vol. 10, no. 3, pp. 187–191, 2015.
- [11] S. Maekawa and U. Gafvert, "Electron tunneling between ferromagnetic films," *IEEE Transactions on Magnetics*, vol. 18, pp. 707–708, Mar. 1982.
- [12] J. Nowak and J. Rauhuzkiewicz, "Spin dependent electron tunneling between ferromagnetic films," *Journal of Magnetism and Magnetic Materials*, vol. 109, pp. 79–90, Feb. 1992.
- [13] J.-G. J. Zhu and C. Park, "Magnetic tunnel junctions," *Materials Today*, vol. 9, no. 11, pp. 36–45, 2006.
- [14] T. Miyazaki, T. Yaoi, and S. Ishio, "Large magnetoresistance effect in (82)Ni-Fe/Al-Al(2)O(3)/Co magnetic tunneling junction," *Journal of Magnetism and Magnetic Materials*, vol. 98, pp. L7–L9, July 1991.
- [15] T. Miyazaki and N. Tezuka, "Giant magnetic tunneling effect in Fe/Al(2)O(3)/Fe junction," *Journal of Magnetism and Magnetic Materials*, vol. 139, pp. L231–L234, Jan. 1995.
- [16] W. H. Butler, X.-G. Zhang, T. C. Schulthess, and J. M. MacLaren, "Spin-dependent tunneling conductance of Fe/MgO/Fe sandwiches," *Physical Review B*, vol. 63, p. 054416, Jan. 2001.

- [17] J. Mathon and A. Umerski, “Theory of tunneling magnetoresistance of an epitaxial Fe/MgO/Fe(001) junction,” *Physical Review B*, vol. 63, p. 220403, May 2001.
- [18] M. Bowen, V. Cros, F. Petroff, A. Fert, C. M. Boubeta, J. L. Costa-Krämer, J. V. Anguita, A. Cebollada, F. Briones, J. M. d. Teresa, L. Morellón, M. R. Ibarra, F. Güell, F. Peiró, and A. Cornet, “Large magnetoresistance in Fe/MgO/FeCo(001) epitaxial tunnel junctions on GaAs(001),” *Applied Physics Letters*, vol. 79, pp. 1655–1657, Sept. 2001.
- [19] J. Faure-Vincent, C. Tiusan, E. Jouguelet, F. Canet, M. Sajieddine, C. Belloward, E. Popova, M. Hehn, F. Montaigne, and A. Schuhl, “High tunnel magnetoresistance in epitaxial Fe/MgO/Fe tunnel junctions,” *Applied Physics Letters*, vol. 82, no. 25, p. 4507, 2003.
- [20] S. S. P. Parkin, C. Kaiser, A. Panchula, P. M. Rice, B. Hughes, M. Samant, and S.-H. Yang, “Giant tunnelling magnetoresistance at room temperature with MgO (100) tunnel barriers,” *Nature Materials*, vol. 3, pp. 862–867, Dec. 2004.
- [21] S. Yuasa, A. Fukushima, T. Nagahama, K. Ando, and Y. Suzuki, “High Tunnel Magnetoresistance at Room Temperature in Fully Epitaxial Fe/MgO/Fe Tunnel Junctions due to Coherent Spin-Polarized Tunneling,” *Japanese Journal of Applied Physics*, vol. 43, pp. L588–L590, Apr. 2004.
- [22] S. Yuasa, T. Nagahama, A. Fukushima, Y. Suzuki, and K. Ando, “Giant room-temperature magnetoresistance in single-crystal Fe/MgO/Fe magnetic tunnel junctions,” *Nature Materials*, vol. 3, pp. 868–871, Dec. 2004.
- [23] D. D. Djayaprawira, K. Tsunekawa, M. Nagai, H. Maehara, S. Yamagata, N. Watanabe, S. Yuasa, Y. Suzuki, and K. Ando, “230% room-temperature

- magnetoresistance in CoFeB/MgO/CoFeB magnetic tunnel junctions,” *Applied Physics Letters*, vol. 86, p. 092502, Feb. 2005.
- [24] S. Ikeda, J. Hayakawa, Y. Ashizawa, Y. M. Lee, K. Miura, H. Hasegawa, M. Tsunoda, F. Matsukura, and H. Ohno, “Tunnel magnetoresistance of 604% at 300k by suppression of Ta diffusion in CoFeB/MgO/CoFeB pseudo-spin-valves annealed at high temperature,” *Applied Physics Letters*, vol. 93, p. 082508, Aug. 2008.
- [25] D. Apalkov, A. Ong, A. Driskill-Smith, M. Krounbi, A. Khvalkovskiy, S. Watts, V. Nikitin, X. Tang, D. Lottis, K. Moon, X. Luo, and E. Chen, “Spin-transfer torque magnetic random access memory (STT-MRAM),” *ACM Journal on Emerging Technologies in Computing Systems*, vol. 9, pp. 1–35, May 2013.
- [26] S. S. P. Parkin, K. P. Roche, M. G. Samant, P. M. Rice, R. B. Beyers, R. E. Scheuerlein, E. J. O’Sullivan, S. L. Brown, J. Bucchigano, D. W. Abraham, Y. Lu, M. Rooks, P. L. Trouilloud, R. A. Wanner, and W. J. Gallagher, “Exchange-biased magnetic tunnel junctions and application to nonvolatile magnetic random access memory (invited),” *Journal of Applied Physics*, vol. 85, pp. 5828–5833, Apr. 1999.
- [27] W. J. Gallagher, J. H. Kaufman, S. S. P. Parkin, and R. E. Scheuerlein, “Magnetic memory array using magnetic tunnel junction devices in the memory cells,” June 1997. Patent US5640343 A.
- [28] S. Tehrani, J. M. Slaughter, M. Deherrera, B. N. Engel, N. D. Rizzo, J. Salter, M. Durlam, R. W. Dave, J. Janesky, B. Butcher, K. Smith, and G. Grynkewich, “Magnetoresistive random access memory using magnetic tunnel junctions,” *Proceedings of the IEEE*, vol. 91, pp. 703–714, May 2003.

- [29] J. M. Slaughter, N. D. Rizzo, F. B. Mancoff, R. Whig, K. Smith, S. Aggarwal, and S. Tehrani, "Toggle and Spin Toggle and Spin-Torque MRAM: Status and Outlook Torque MRAM: Status and Outlook Torque MRAM: Status and Outlook," *Trans. Magn*, vol. 41, p. 132, 2010.
- [30] S. S. P. Parkin, N. More, and K. P. Roche, "Oscillations in exchange coupling and magnetoresistance in metallic superlattice structures: Co/Ru, Co/Cr, and Fe/Cr," *Physical Review Letters*, vol. 64, pp. 2304–2307, May 1990.
- [31] D. E. Heim and S. S. P. Parkin, "Magnetoresistive spin valve sensor with improved pinned ferromagnetic layer and magnetic recording system using the sensor," Nov. 1995. Patent US5465185 A.
- [32] L. Savtchenko, A. Korkin, B. Engel, N. Rizzo, M. Deherrera, and J. Janesky, "Method of writing to a scalable magnetoresistance random access memory element," July 2003. Patent US20030128603 A1.
- [33] B. N. Engel, J. Akerman, B. Butcher, R. W. Dave, M. DeHerrera, M. Durlam, G. Grynkewich, J. Janesky, S. V. Pietambaram, N. D. Rizzo, J. M. Slaughter, K. Smith, J. J. Sun, and S. Tehrani, "A 4-Mb toggle MRAM based on a novel bit and switching method," *IEEE Transactions on Magnetics*, vol. 41, pp. 132–136, Jan. 2005.
- [34] L. Thomas, G. Jan, J. Zhu, H. Liu, Y.-J. Lee, S. Le, R.-Y. Tong, K. Pi, Y.-J. Wang, D. Shen, R. He, J. Haq, J. Teng, V. Lam, K. Huang, T. Zhong, T. Torng, and P.-K. Wang, "Perpendicular spin transfer torque magnetic random access memories with high spin torque efficiency and thermal stability for embedded applications (invited)," *Journal of Applied Physics*, vol. 115, p. 172615, May 2014.

- [35] J. C. Slonczewski, “Current-driven excitation of magnetic multilayers,” *Journal of Magnetism and Magnetic Materials*, vol. 159, pp. L1–L7, June 1996.
- [36] L. Berger, “Emission of spin waves by a magnetic multilayer traversed by a current,” *Physical Review B*, vol. 54, no. 13, p. 9353, 1996.
- [37] M. Tsoi, A. G. M. Jansen, J. Bass, W.-C. Chiang, M. Seck, V. Tsoi, and P. Wyder, “Excitation of a Magnetic Multilayer by an Electric Current,” *Physical Review Letters*, vol. 80, pp. 4281–4284, May 1998.
- [38] n. Myers, n. Ralph, n. Katine, n. Louie, and n. Buhrman, “Current-induced switching of domains in magnetic multilayer devices,” *Science (New York, N.Y.)*, vol. 285, pp. 867–870, Aug. 1999.
- [39] J. Sun, “Current-driven magnetic switching in manganite trilayer junctions,” *Journal of Magnetism and Magnetic Materials*, vol. 202, pp. 157–162, June 1999.
- [40] J. A. Katine, F. J. Albert, R. A. Buhrman, E. B. Myers, and D. C. Ralph, “Current-Driven Magnetization Reversal and Spin-Wave Excitations in Co/Cu/Co Pillars,” *Physical Review Letters*, vol. 84, pp. 3149–3152, Apr. 2000.
- [41] S. Mangin, D. Ravelosona, J. A. Katine, M. J. Carey, B. D. Terris, and E. E. Fullerton, “Current-induced magnetization reversal in nanopillars with perpendicular anisotropy,” *Nature Materials*, vol. 5, pp. 210–215, Mar. 2006.
- [42] J. Sun and D. Ralph, “Magnetoresistance and spin-transfer torque in magnetic tunnel junctions,” *Journal of Magnetism and Magnetic Materials*, vol. 320, pp. 1227–1237, Apr. 2008.

- [43] J. Katine and E. E. Fullerton, “Device implications of spin-transfer torques,” *Journal of Magnetism and Magnetic Materials*, vol. 320, pp. 1217–1226, Apr. 2008.
- [44] Y. Huai, F. Albert, P. Nguyen, M. Pakala, and T. Valet, “Observation of spin-transfer switching in deep submicron-sized and low-resistance magnetic tunnel junctions,” *Applied Physics Letters*, vol. 84, no. 16, p. 3118, 2004.
- [45] G. D. Fuchs, N. C. Emley, I. N. Krivorotov, P. M. Braganca, E. M. Ryan, S. I. Kiselev, J. C. Sankey, J. A. Katine, D. C. Ralph, and R. A. Buhrman, “Spin-transfer effects in nanoscale magnetic tunnel junctions,” *arXiv preprint cond-mat/0404002*, 2004.
- [46] Z. Diao, A. Panchula, Y. Ding, M. Pakala, S. Wang, Z. Li, D. Apalkov, H. Nagai, A. Driskill-Smith, L.-C. Wang, E. Chen, and Y. Huai, “Spin transfer switching in dual MgO magnetic tunnel junctions,” *Applied Physics Letters*, vol. 90, p. 132508, Mar. 2007.
- [47] M. Hosomi, H. Yamagishi, T. Yamamoto, K. Bessho, Y. Higo, K. Yamane, H. Yamada, M. Shoji, H. Hachino, C. Fukumoto, and others, “A novel non-volatile memory with spin torque transfer magnetization switching: Spin-RAM,” *IEDM Tech. Dig*, vol. 459, 2005.
- [48] T. Kawahara, R. Takemura, K. Miura, J. Hayakawa, S. Ikeda, Y. M. Lee, R. Sasaki, Y. Goto, K. Ito, T. Meguro, F. Matsukura, H. Takahashi, H. Matsuoka, and H. Ohno, “2 Mb SPRAM (SPin-Transfer Torque RAM) With Bit-by-Bit Bi-Directional Current Write and Parallelizing-Direction Current Read,” *IEEE Journal of Solid-State Circuits*, vol. 43, pp. 109–120, Jan. 2008.
- [49] C. J. Lin, S. H. Kang, Y. J. Wang, K. Lee, X. Zhu, W. C. Chen, X. Li, W. N. Hsu, Y. C. Kao, M. T. Liu, and others, “45nm low power CMOS logic

- compatible embedded STT MRAM utilizing a reverse-connection 1t/1mtj cell,” in *2009 IEEE International Electron Devices Meeting (IEDM)*, pp. 1–4, IEEE, 2009.
- [50] S. Chung, K. M. Rho, S. D. Kim, H. J. Suh, D. J. Kim, H. J. Kim, S. H. Lee, J. H. Park, H. M. Hwang, S. M. Hwang, J. Y. Lee, Y. B. An, J. U. Yi, Y. H. Seo, D. H. Jung, M. S. Lee, S. H. Cho, J. N. Kim, G. J. Park, G. Jin, A. Driskill-Smith, V. Nikitin, A. Ong, X. Tang, Y. Kim, J. S. Rho, S. K. Park, S. W. Chung, J. G. Jeong, and S. J. Hong, “Fully integrated 54nm STT-RAM with the smallest bit cell dimension for high density memory application,” in *Electron Devices Meeting (IEDM), 2010 IEEE International*, pp. 12.7.1–12.7.4, Dec. 2010.
- [51] N. D. Rizzo, D. Houssameddine, J. Janesky, R. Whig, F. B. Mancoff, M. L. Schneider, M. DeHerrera, J. J. Sun, K. Nagel, S. Deshpande, H. J. Chia, S. M. Alam, T. Andre, S. Aggarwal, and J. M. Slaughter, “A Fully Functional 64 Mb DDR3 ST-MRAM Built on 90 nm CMOS Technology,” *IEEE Transactions on Magnetics*, vol. 49, pp. 4441–4446, July 2013.
- [52] T. Yamamoto, H. Kano, Y. Higo, K. Ohba, T. Mizuguchi, M. Hosomi, K. Bessho, M. Hashimoto, H. Ohmori, T. Sone, K. Endo, S. Kubo, H. Narisawa, W. Otsuka, N. Okazaki, M. Motoyoshi, H. Nagao, and T. Sagara, “Magnetoresistive random access memory operation error by thermally activated reversal (invited),” *Journal of Applied Physics*, vol. 97, p. 10P503, May 2005.
- [53] E. Chen, D. Apalkov, Z. Diao, A. Driskill-Smith, D. Druist, D. Lottis, V. Nikitin, X. Tang, S. Watts, S. Wang, S. A. Wolf, A. W. Ghosh, J. W. Lu, S. J. Poon, M. Stan, W. H. Butler, S. Gupta, C. K. A. Mewes,

- T. Mewes, and P. B. Visscher, “Advances and Future Prospects of Spin-Transfer Torque Random Access Memory,” *IEEE Transactions on Magnetism*, vol. 46, pp. 1873–1878, June 2010.
- [54] J. Z. Sun, “Spin-current interaction with a monodomain magnetic body: A model study,” *Physical Review B*, vol. 62, pp. 570–578, July 2000.
- [55] L. Liu, T. Moriyama, D. C. Ralph, and R. A. Buhrman, “Reduction of the spin-torque critical current by partially canceling the free layer demagnetization field,” *Applied Physics Letters*, vol. 94, p. 122508, Mar. 2009.
- [56] T. Kishi, H. Yoda, T. Kai, T. Nagase, E. Kitagawa, M. Yoshikawa, K. Nishiyama, T. Daibou, M. Nagamine, M. Amano, S. Takahashi, M. Nakayama, N. Shimomura, H. Aikawa, S. Ikegawa, S. Yuasa, K. Yakushiji, H. Kubota, A. Fukushima, M. Oogane, T. Miyazaki, and K. Ando, “Lower-current and fast switching of a perpendicular TMR for high speed and high density spin-transfer-torque MRAM,” in *2008 IEEE International Electron Devices Meeting*, pp. 1–4, Dec. 2008.
- [57] M. Gajek, J. J. Nowak, J. Z. Sun, P. L. Trouilloud, E. J. O’Sullivan, D. W. Abraham, M. C. Gaidis, G. Hu, S. Brown, Y. Zhu, R. P. Robertazzi, W. J. Gallagher, and D. C. Worledge, “Spin torque switching of 20 nm magnetic tunnel junctions with perpendicular anisotropy,” *Applied Physics Letters*, vol. 100, p. 132408, Mar. 2012.
- [58] G. Jan, Y.-J. Wang, T. Moriyama, Y.-J. Lee, M. Lin, T. Zhong, R.-Y. Tong, T. Torng, and P.-K. Wang, “High Spin Torque Efficiency of Magnetic Tunnel Junctions with MgO/CoFeB/MgO Free Layer,” *Applied Physics Express*, vol. 5, p. 093008, Sept. 2012.

- [59] S. Ikeda, K. Miura, H. Yamamoto, K. Mizunuma, H. D. Gan, M. Endo, S. Kanai, J. Hayakawa, F. Matsukura, and H. Ohno, “A perpendicular-anisotropy CoFeB–MgO magnetic tunnel junction,” *Nature Materials*, vol. 9, pp. 721–724, Sept. 2010.
- [60] D. C. Worledge, G. Hu, D. W. Abraham, J. Z. Sun, P. L. Trouilloud, J. Nowak, S. Brown, M. C. Gaidis, E. J. O’Sullivan, and R. P. Robertazzi, “Spin torque switching of perpendicular Ta-CoFeB-MgO-based magnetic tunnel junctions,” *Applied Physics Letters*, vol. 98, p. 022501, Jan. 2011.
- [61] D. C. Worledge, G. Hu, P. L. Trouilloud, D. W. Abraham, S. Brown, M. C. Gaidis, J. Nowak, E. J. O’Sullivan, R. P. Robertazzi, J. Z. Sun, and W. J. Gallagher, “Switching distributions and write reliability of perpendicular spin torque MRAM,” in *Electron Devices Meeting (IEDM), 2010 IEEE International*, pp. 12.5.1–12.5.4, Dec. 2010.
- [62] M. Yoshikawa, E. Kitagawa, T. Nagase, T. Daibou, M. Nagamine, K. Nishiyama, T. Kishi, and H. Yoda, “Tunnel Magnetoresistance Over 100% in MgO-Based Magnetic Tunnel Junction Films With Perpendicular Magnetic L1(0)-FePt Electrodes,” *IEEE Transactions on Magnetism*, vol. 44, pp. 2573–2576, Nov. 2008.
- [63] M. Nakayama, T. Kai, N. Shimomura, M. Amano, E. Kitagawa, T. Nagase, M. Yoshikawa, T. Kishi, S. Ikegawa, and H. Yoda, “Spin transfer switching in TbCoFe/CoFeB/MgO/CoFeB/TbCoFe magnetic tunnel junctions with perpendicular magnetic anisotropy,” *Journal of Applied Physics*, vol. 103, p. 07A710, Apr. 2008.
- [64] W. Kim, J. H. Jeong, Y. Kim, W. C. Lim, J. H. Kim, J. H. Park, H. J. Shin, Y. S. Park, K. S. Kim, S. H. Park, Y. J. Lee, K. W. Kim, H. J. Kwon,

- H. L. Park, H. S. Ahn, S. C. Oh, J. E. Lee, S. O. Park, S. Choi, H. K. Kang, and C. Chung, "Extended scalability of perpendicular STT-MRAM towards sub-20nm MTJ node," in *Electron Devices Meeting (IEDM), 2011 IEEE International*, pp. 24.1.1–24.1.4, Dec. 2011.
- [65] P. F. Carcia, A. D. Meinhaldt, and A. Suna, "Perpendicular magnetic anisotropy in Pd/Co thin film layered structures," *Applied Physics Letters*, vol. 47, pp. 178–180, July 1985.
- [66] S. Mangin, Y. Henry, D. Ravelosona, J. A. Katine, and E. E. Fullerton, "Reducing the critical current for spin-transfer switching of perpendicularly magnetized nanomagnets," *Applied Physics Letters*, vol. 94, p. 012502, Jan. 2009.
- [67] H. Kurt, M. Venkatesan, and J. M. D. Coey, "Enhanced perpendicular magnetic anisotropy in Co/Ni multilayers with a thin seed layer," *Journal of Applied Physics*, vol. 108, p. 073916, Oct. 2010.
- [68] T. Graf, C. Felser, and S. S. Parkin, "Simple rules for the understanding of Heusler compounds," *Progress in Solid State Chemistry*, vol. 39, pp. 1–50, May 2011.
- [69] C. Felser, G. H. Fecher, and B. Balke, "Spintronics: A Challenge for Materials Science and Solid-State Chemistry," *Angewandte Chemie International Edition*, vol. 46, pp. 668–699, Jan. 2007.
- [70] S. Chadov, X. Qi, J. Kübler, G. H. Fecher, C. Felser, and S. C. Zhang, "Tunable multifunctional topological insulators in ternary Heusler compounds," *Nature Materials*, vol. 9, pp. 541–545, July 2010.

- [71] H. Lin, L. A. Wray, Y. Xia, S. Xu, S. Jia, R. J. Cava, A. Bansil, and M. Z. Hasan, “Half-Heusler ternary compounds as new multifunctional experimental platforms for topological quantum phenomena,” *Nature Materials*, vol. 9, pp. 546–549, July 2010.
- [72] F. Kalarasse, B. Bennecer, and A. Mellouki, “Optical properties of the filled tetrahedral semiconductors LiMgX (X=N, P and As),” *Journal of Physics: Condensed Matter*, vol. 18, no. 31, p. 7237, 2006.
- [73] S.-H. Wei and A. Zunger, “Alloy-stabilized semiconducting and magnetic zinc-blende phase of MnTe,” *Physical review letters*, vol. 56, no. 22, p. 2391, 1986.
- [74] J. J. Martin, “Thermal conductivity of Mg(2)Si, Mg(2)Ge and Mg(2)Sn,” *Journal of Physics and Chemistry of Solids*, vol. 33, pp. 1139–1148, Jan. 1972.
- [75] Y. Nishino, M. Kato, S. Asano, K. Soda, M. Hayasaki, and U. Mizutani, “Semiconductorlike behavior of electrical resistivity in Heusler-type Fe(2)VAI compound,” *Physical review letters*, vol. 79, no. 10, p. 1909, 1997.
- [76] N. Kawamiya, Y. Nishino, M. Matsuo, and S. Asano, “Electrical-resistance maximum near the Curie point in [Fe(1-x)V(x)](3)Ga and [Fe(1-x)Ti(x)](3)Ga,” *Physical Review B*, vol. 44, no. 22, p. 12406, 1991.
- [77] J. H. Wernick, G. W. Hull, T. H. Geballe, J. E. Bernardini, and J. V. Waszczak, “Superconductivity in ternary Heusler intermetallic compounds,” *Materials Letters*, vol. 2, no. 2, pp. 90–92, 1983.
- [78] H. A. Kierstead, B. D. Dunlap, S. K. Malik, A. M. Umarji, Shenoy, and GK, “Coexistence of ordered magnetism and superconductivity in Pd(2)YbSn,” *Physical Review B*, vol. 32, no. 1, p. 135, 1985.

- [79] R. N. Shelton, L. S. Hausermann-Berg, P. Klavins, H. D. Yang, M. S. Anderson, and C. A. Swenson, “Electronic phase transition and partially gapped Fermi surface in superconducting Lu(5)Ir(4)Si(10),” *Physical Review B*, vol. 34, no. 7, p. 4590, 1986.
- [80] S. Sakurada and N. Shutoh, “Effect of Ti substitution on the thermoelectric properties of (Zr,Hf)NiSn half-Heusler compounds,” *Applied Physics Letters*, vol. 86, p. 082105, Feb. 2005.
- [81] O. Meshcheriakova, S. Chadov, A. K. Nayak, U. K. Rößler, J. Kübler, G. André, A. A. Tsirlin, J. Kiss, S. Hausdorf, A. Kalache, W. Schnelle, M. Nicklas, and C. Felser, “Large Noncollinearity and Spin Reorientation in the Novel Mn(2)RhSn Heusler Magnet,” *Physical Review Letters*, vol. 113, Aug. 2014.
- [82] P. G. v. Engen, K. H. J. Buschow, R. Jongebreur, and M. Erman, “PtMnSb, a material with very high magneto optical Kerr effect,” *Applied Physics Letters*, vol. 42, pp. 202–204, Jan. 1983.
- [83] T. Krenke, E. Duman, M. Acet, E. F. Wassermann, X. Moya, L. Mañosa, and A. Planes, “Inverse magnetocaloric effect in ferromagnetic Ni–Mn–Sn alloys,” *Nature Materials*, vol. 4, pp. 450–454, June 2005.
- [84] A. K. Nayak, M. Nicklas, S. Chadov, P. Khuntia, C. Shekhar, A. Kalache, M. Baenitz, Y. Skourski, V. K. Guduru, A. Puri, U. Zeitler, J. M. D. Coey, and C. Felser, “Design of compensated ferrimagnetic Heusler alloys for giant tunable exchange bias,” *Nature Materials*, vol. 14, pp. 679–684, July 2015.
- [85] R. A. de Groot, F. M. Mueller, P. G. v. Engen, and K. H. J. Buschow, “New Class of Materials: Half-Metallic Ferromagnets,” *Physical Review Letters*, vol. 50, pp. 2024–2027, June 1983.

- [86] M. Jourdan, J. Minár, J. Braun, A. Kronenberg, S. Chadov, B. Balke, A. Gloskovskii, M. Kolbe, H. Elmers, G. Schönhense, H. Ebert, C. Felser, and M. Kläui, “Direct observation of half-metallicity in the Heusler compound $\text{Co}(2)\text{MnSi}$,” *Nature Communications*, vol. 5, May 2014.
- [87] J. Jeong, Y. Ferrante, S. V. Faleev, M. G. Samant, C. Felser, and S. S. P. Parkin, “Termination layer compensated tunnelling magnetoresistance in ferrimagnetic Heusler compounds with high perpendicular magnetic anisotropy,” *Nature Communications*, vol. 7, p. 10276, Jan. 2016.
- [88] F. Wu, S. Mizukami, D. Watanabe, H. Naganuma, M. Oogane, Y. Ando, and T. Miyazaki, “Epitaxial $\text{Mn}(2.5)\text{Ga}$ thin films with giant perpendicular magnetic anisotropy for spintronic devices,” *Applied Physics Letters*, vol. 94, no. 12, p. 122503, 2009.
- [89] S. Li, Y. K. Takahashi, T. Furubayashi, and K. Hono, “Enhancement of giant magnetoresistance by $L2(1)$ ordering in $\text{Co}(2)\text{Fe}[\text{Ge}(0.5)\text{Ga}(0.5)]$ Heusler alloy current-perpendicular-to-plane pseudo spin valves,” *Applied Physics Letters*, vol. 103, no. 4, p. 042405, 2013.
- [90] S. V. Faleev, Y. Ferrante, J. Jeong, M. G. Samant, B. Jones, and S. S. P. Parkin, “Unified explanation of chemical ordering, the Slater-Pauling rule, and half-metallicity in full Heusler compounds,” *Physical Review B*, vol. 95, p. 045140, Jan. 2017.
- [91] L. Wollmann, S. Chadov, J. Kübler, and C. Felser, “Magnetism in cubic manganese-rich Heusler compounds,” *Physical Review B*, vol. 90, Dec. 2014.
- [92] J. Winterlik, S. Chadov, A. Gupta, V. Alijani, T. Gasi, K. Filsinger, B. Balke, G. H. Fecher, C. A. Jenkins, F. Casper, J. Kübler, G.-D. Liu, L. Gao, S. S. P. Parkin, and C. Felser, “Design Scheme of New Tetragonal

- Heusler Compounds for Spin-Transfer Torque Applications and its Experimental Realization,” *Advanced Materials*, vol. 24, pp. 6283–6287, Dec. 2012.
- [93] L. Wollmann, S. Chadov, J. Kübler, and C. Felser, “Magnetism in tetragonal manganese-rich Heusler compounds,” *Physical Review B*, vol. 92, p. 064417, Aug. 2015.
- [94] S. V. Faleev, Y. Ferrante, J. Jeong, M. G. Samant, B. Jones, and S. S. Parkin, “Origin of the Tetragonal Ground State of Heusler Compounds,” *Physical Review Applied*, vol. 7, p. 034022, Mar. 2017.
- [95] L. Van Hove, “The Occurrence of Singularities in the Elastic Frequency Distribution of a Crystal,” *Physical Review*, vol. 89, pp. 1189–1193, Mar. 1953.
- [96] H. A. Jahn and E. Teller, “Stability of Polyatomic Molecules in Degenerate Electronic States. I. Orbital Degeneracy,” *Proceedings of the Royal Society of London A: Mathematical, Physical and Engineering Sciences*, vol. 161, pp. 220–235, July 1937.
- [97] J. I. Gersten and F. W. Smith, *The physics and chemistry of materials*. New York: Wiley, 2001.
- [98] J. C. Suits, “Structural instability in new magnetic heusler compounds,” *Solid State Communications*, vol. 18, pp. 423–425, Jan. 1976.
- [99] J. H. van Vleck, “On the anisotropy of cubic ferromagnetic crystals,” *Physical Review*, vol. 52, no. 11, p. 1178, 1937.
- [100] C. Kittel, *Introduction to solid state physics*. Hoboken, NJ: Wiley, 8th ed ed., 2005.

-
- [101] S. Blundell, *Magnetism in condensed matter*. Oxford master series in condensed matter physics, Oxford ; New York: Oxford University Press, 2001.
- [102] T. Burkert, L. Nordström, O. Eriksson, and O. Heinonen, “Giant Magnetic Anisotropy in Tetragonal FeCo Alloys,” *Physical Review Letters*, vol. 93, p. 027203, July 2004.
- [103] A. Winkelmann, M. Przybylski, F. Luo, Y. Shi, and J. Barthel, “Perpendicular Magnetic Anisotropy Induced by Tetragonal Distortion of FeCo Alloy Films Grown on Pd(001),” *Physical Review Letters*, vol. 96, p. 257205, June 2006.
- [104] F. Luo, X. L. Fu, A. Winkelmann, and M. Przybylski, “Tuning the perpendicular magnetic anisotropy in tetragonally distorted Fe(x)Co(1-x) alloy films on Rh (001) by varying the alloy composition,” *Applied Physics Letters*, vol. 91, p. 262512, Dec. 2007.
- [105] E. Krén and G. Kádár, “Neutron diffraction study of Mn(3)Ga,” *Solid State Communications*, vol. 8, pp. 1653–1655, Oct. 1970.
- [106] A. K. Nayak, C. Shekhar, J. Winterlik, A. Gupta, and C. Felser, “Mn(2)PtIn: A tetragonal Heusler compound with exchange bias behavior,” *Applied Physics Letters*, vol. 100, p. 152404, Apr. 2012.
- [107] A. K. Nayak, M. Nicklas, S. Chadov, C. Shekhar, Y. Skourski, J. Winterlik, and C. Felser, “Large Zero-Field Cooled Exchange-Bias in Bulk Mn(2)PtGa,” *Physical Review Letters*, vol. 110, p. 127204, Mar. 2013.

- [108] D. Zhang, B. Yan, S.-C. Wu, J. Kübler, G. Kreiner, S. S. Parkin, and C. Felser, “First-principles study of the structural stability of cubic, tetragonal and hexagonal phases in Mn(3)Z (Z= Ga, Sn and Ge) Heusler compounds,” *Journal of Physics: Condensed Matter*, vol. 25, no. 20, p. 206006, 2013.
- [109] B. Balke, G. H. Fecher, J. Winterlik, and C. Felser, “Mn(3)Ga, a compensated ferrimagnet with high Curie temperature and low magnetic moment for spin torque transfer applications,” *Applied Physics Letters*, vol. 90, p. 152504, Apr. 2007.
- [110] A. Sugihara, K. Suzuki, T. Miyazaki, and S. Mizukami, “Epitaxial Growth of Hard Ferrimagnetic Mn(3)Ge Film on Rhodium Buffer Layer,” *Metals*, vol. 5, pp. 910–919, June 2015.
- [111] H. Kurt, N. Baadji, K. Rode, M. Venkatesan, P. Stamenov, S. Sanvito, and J. M. D. Coey, “Magnetic and electronic properties of D0(22)-Mn(3)Ge (001) films,” *Applied Physics Letters*, vol. 101, no. 13, p. 132410, 2012.
- [112] H. Kurt, K. Rode, M. Venkatesan, P. Stamenov, and J. M. D. Coey, “High spin polarization in epitaxial films of ferrimagnetic Mn(3)Ga,” *Physical Review B*, vol. 83, p. 020405, Jan. 2011.
- [113] M. Li, X. Jiang, M. G. Samant, C. Felser, and S. S. P. Parkin, “Strong dependence of the tetragonal Mn(2.1)Ga thin film crystallization temperature window on seed layer,” *Applied Physics Letters*, vol. 103, no. 3, p. 032410, 2013.
- [114] K. Rode, N. Baadji, D. Betto, Y.-C. Lau, H. Kurt, M. Venkatesan, P. Stamenov, S. Sanvito, J. M. D. Coey, E. Fonda, E. Otero, F. Choueikani,

- P. Ohresser, F. Porcher, and G. André, “Site-specific order and magnetism in tetragonal Mn(3)Ga thin films,” *Physical Review B*, vol. 87, May 2013.
- [115] C. Felser, V. Alijani, J. Winterlik, S. Chadov, and A. K. Nayak, “Tetragonal Heusler Compounds for Spintronics,” *IEEE Transactions on Magnetism*, vol. 49, pp. 682–685, Feb. 2013.
- [116] S. S. P. Parkin, “MgO tunnel barriers and method of formation,” Aug. 2011. Patent US8008097 B2.
- [117] H. Sato, E. C. I. Enobio, M. Yamanouchi, S. Ikeda, S. Fukami, S. Kanai, F. Matsukura, and H. Ohno, “Properties of magnetic tunnel junctions with a MgO/CoFeB/Ta/CoFeB/MgO recording structure down to junction diameter of 11 nm,” *Applied Physics Letters*, vol. 105, p. 062403, Aug. 2014.
- [118] A. D. Kent, “Spintronics: Perpendicular all the way,” *Nature Materials*, vol. 9, pp. 699–700, Sept. 2010.
- [119] D. Weller, A. Moser, L. Folks, M. E. Best, W. Lee, M. F. Toney, M. Schwickert, J. U. Thiele, and M. F. Doerner, “High Ku materials approach to 100 Gbits/in²,” *IEEE Transactions on Magnetism*, vol. 36, pp. 10–15, Jan. 2000.
- [120] H. Sato, M. Yamanouchi, S. Ikeda, S. Fukami, F. Matsukura, and H. Ohno, “Perpendicular-anisotropy CoFeB-MgO magnetic tunnel junctions with a MgO/CoFeB/Ta/CoFeB/MgO recording structure,” *Applied Physics Letters*, vol. 101, p. 022414, July 2012.
- [121] M. Endo, S. Kanai, S. Ikeda, F. Matsukura, and H. Ohno, “Electric-field effects on thickness dependent magnetic anisotropy of sputtered MgO/Co(40)Fe(40)B(20)/Ta structures,” *Applied Physics Letters*, vol. 96, p. 212503, May 2010.

-
- [122] F. Wu, S. Mizukami, D. Watanabe, E. P. Sajitha, H. Naganuma, M. Oogane, Y. Ando, and T. Miyazaki, "Structural and Magnetic Properties of Perpendicular Magnetized Mn Ga Epitaxial Films," *IEEE Transactions on Magnetics*, vol. 46, pp. 1863–1865, June 2010.
- [123] A. Köhler, I. Knez, D. Ebke, C. Felser, and S. S. P. Parkin, "Loss of anisotropy in strained ultrathin epitaxial L1(0) Mn-Ga films," *Applied Physics Letters*, vol. 103, no. 16, p. 162406, 2013.
- [124] D. A. Glocker and S. I. Shah, *Handbook of Thin Film Process Technology*. Institute of Physics Pub., 1995.
- [125] H. R. Kaufman, *Fundamentals of Ion-source Operation*. Commonwealth Scientific Corporation, 1984.
- [126] S. A. Chambers, "Epitaxial growth and properties of thin film oxides," *Surface Science Reports*, vol. 39, pp. 105–180, Aug. 2000.
- [127] H. C. Galloway, J. J. Benítez, and M. Salmeron, "Growth of FeOx on Pt(111) studied by scanning tunneling microscopy," *Journal of Vacuum Science & Technology A*, vol. 12, pp. 2302–2307, July 1994.
- [128] Y. J. Kim, C. Westphal, R. X. Ynzunza, Z. Wang, H. C. Galloway, M. Salmeron, M. A. Van Hove, and C. S. Fadley, "The growth of iron oxide films on Pt(111): a combined XPD, STM, and LEED study," *Surface Science*, vol. 416, pp. 68–111, Oct. 1998.
- [129] A. Sugihara, S. Mizukami, Y. Yamada, K. Koike, and T. Miyazaki, "High perpendicular magnetic anisotropy in D0(22)-Mn(3+x)Ge tetragonal Heusler alloy films," *Applied Physics Letters*, vol. 104, p. 132404, Mar. 2014.

- [130] S. Mizukami, A. Sakuma, A. Sugihara, T. Kubota, Y. Kondo, H. Tsuchiura, and T. Miyazaki, “Tetragonal D0(22) Mn(3+x)Ge Epitaxial Films Grown on MgO(100) with a Large Perpendicular Magnetic Anisotropy,” *Applied Physics Express*, vol. 6, p. 123002, Dec. 2013.
- [131] A. Kohn, A. Kovács, R. Fan, G. J. McIntyre, R. C. C. Ward, and J. P. Goff, “The antiferromagnetic structures of IrMn(3) and their influence on exchange-bias,” *Scientific Reports*, vol. 3, Aug. 2013.
- [132] M. G. Samant, J. Lüning, J. Stöhr, and S. S. P. Parkin, “Thermal stability of IrMn and MnFe exchange-biased magnetic tunnel junctions,” *Applied Physics Letters*, vol. 76, pp. 3097–3099, May 2000.
- [133] J. Jeong, S. S. P. Parkin, and M. G. Samant, “Underlayers for textured films of Heusler compounds,” Aug. 2016. Patent US9406365 B1.
- [134] P. Liu, T. Kendelewicz, G. E. Brown Jr., and G. A. Parks, “Reaction of water with MgO(100) surfaces. Part I: Synchrotron X-ray photoemission studies of low-defect surfaces,” *Surface Science*, vol. 412–413, pp. 287–314, Sept. 1998.
- [135] Y. Miura and M. Shirai, “Theoretical Study on Tunneling Magnetoresistance of Magnetic Tunnel Junctions with D0(22)-Mn(3)Z (Z =Ga,Ge),” *IEEE Transactions on Magnetics*, vol. 50, pp. 1–4, Jan. 2014.
- [136] D. Wortmann, G. Bihlmayer, and S. Blügel, “Ab initio calculations of interface effects in tunnelling through MgO barriers on Fe(100),” *Journal of Physics: Condensed Matter*, vol. 16, no. 48, p. S5819, 2004.
- [137] S. V. Faleev, S. S. P. Parkin, and O. N. Mryasov, “Brillouin zone spin filtering mechanism of enhanced tunneling magnetoresistance and correlation effects in a Co (0001)/h-BN/Co (0001) magnetic tunnel junction,” *Physical Review B*, vol. 92, Dec. 2015.

-
- [138] Y. Ferrante, J. Jeong, S. V. Faleev, M. G. Samant, and S. S. P. Parkin, “Mn(3-x)Co(x)Ge: a tunable, tetragonal, ferrimagnetic Heusler compound with perpendicular anisotropy,” 2016. Work in progress.
- [139] J. C. Slater, “The Ferromagnetism of Nickel. II. Temperature Effects,” *Physical Review*, vol. 49, pp. 931–937, June 1936.
- [140] L. Pauling, “The Nature of the Interatomic Forces in Metals,” *Physical Review*, vol. 54, pp. 899–904, Dec. 1938.
- [141] J. Kübler, “First principle theory of metallic magnetism,” *Physica B+C*, vol. 127, pp. 257–263, Dec. 1984.
- [142] T. Ambrose, J. J. Krebs, and G. A. Prinz, “Magnetic properties of single crystal Co(2)MnGe Heusler alloy films,” *Journal of Applied Physics*, vol. 87, no. 9, p. 5463, 2000.
- [143] J. L. Hilton, “Characterization and stability of the interfaces between manganese-based metals and compound semiconductors grown by molecular beam epitaxy,” *Ph.D. Thesis*, 2006.
- [144] F. Ricci, S. Picozzi, A. Continenza, F. D’Orazio, F. Lucari, K. Westerholt, M. Kim, and A. J. Freeman, “Optical and magneto-optical properties of ferromagnetic full-Heusler films: Experiments and first-principles calculations,” *Physical Review B*, vol. 76, July 2007.
- [145] T. Klemmer, D. Hoydick, H. Okumura, B. Zhang, and W. A. Soffa, “Magnetic hardening and coercivity mechanisms in L1(0) ordered FePd ferromagnets,” *Scripta Metallurgica et Materialia*, vol. 33, pp. 1793–1805, Dec. 1995.

Publications

[1] C. Martinez-Boubeta, **Y. Ferrante**, and S. S. P. Parkin. "Magnetotransport properties of spin-valve structures with Mg spacer layers". Applied Physics Letters 106, 032412 (2015).

[2] J. Jeong*, **Y. Ferrante***, S. V. Faleev, M. G. Samant, C. Felser, and S. S. P. Parkin. "Termination layer compensated tunneling magnetoresistance in ferrimagnetic Heusler compounds with high perpendicular anisotropy". Nature Communications 7, 10276 (2016) - *Equal contribution.

[3] **Y. Ferrante**, J. Jeong, S. V. Faleev, M. G. Samant, and S. S. P. Parkin. "Mn_{3-x}Co_xGe: a tunable, tetragonal, ferrimagnetic Heusler compound with perpendicular anisotropy". Work in progress.

[4] S. V. Faleev, **Y. Ferrante**, J. Jeong, M. G. Samant, and S. S. P. Parkin. "Unified explanation of chemical ordering, the Slater-Pauling rule, and half-metallicity in full Heusler compounds". Physical Review B 95, 045140 (2017).

[5] S. V. Faleev, **Y. Ferrante**, J. Jeong, M. G. Samant, and S. S. P. Parkin. "Origin of the Tetragonal Ground State of Heusler Compounds". Physical Review Applied 7, 034022 (2017).

[6] J. Zhang, T. Phung, A. Pushp, **Y. Ferrante**, J. Jeong, C. Rettner, B. P. Hughes, S. Yang, Y. Jiang, and S. S. P. Parkin. "Bias dependence of spin transfer torque in Co_2MnSi Heusler alloy based magnetic tunnel junctions". *Applied Physics Letters* 110, 172403 (2017).

Acknowledgements

First and foremost, I would like to thank Prof. Dr. Stuart S. P. Parkin for his supervision and support during my Ph.D research conducted at his extraordinary lab at Almaden IBM Research Center in San Jose, California. I am so amazed by his brilliancy, enthusiasm, passion, energy, and his constant forward-thinking mindset. I am honored to have had the opportunity to learn from him during this important stage of my professional life.

I am also deeply grateful to my mentor and friend Jaewoo Jeong without whom many of our achievements could not have been possible. I enjoyed collaborating with him on a daily basis and consider myself very lucky to have acquired significant amount of knowledge from him and to have been inspired by his passion for research. I thank Jaewoo for those incredible moments of gratification we have shared in the times of our most exciting discoveries after long periods of hard work.

Special thanks go to Sergey Faleev not only for his valuable contribution to this work with the DFT calculations, but also for the many stimulating discussions we had.

I would also like to extend my sincere appreciation to my other colleagues Mahesh Samant, Mazhar Ali, Timothy Phung, Aakash Pushp, and See-Hun Yang for their help, suggestions, and discussions.

I am thankful to Kevin Roche, Chris Lada, Larry Lindebauer, and Manny Hernandez for their vital support with the G-system maintenance.

I am grateful for the constant contribution from Andrew Kellock with his countless number of RBS measurements, Phil Rice, Teya Topuria, Erik Lara, Eugene Delenia, and Leslie Thompson for the TEM and EELS studies, as well as Brian Hughes and Charles Rettner for the lithography patterning of our samples.

I also would like to thank Dr. Luisa Bozano for her ongoing support and kindness throughout the years of my Ph.D research at Almaden.

Many thanks to my colleagues and friends Andrea Fantini, Donata Passarello, Panos Filippou, Tom Pattison, and all the other interns I have met for our special time spent together inside and outside IBM. Our lunches and routine coffee breaks have allowed all of us to laugh, connect, relax, and distract from a hard day of work.

Finally, I would like to thank my mother Pina, my father Beppe, my wife Beili, my brother Ivan, my sister-in-law Justine, and all of my friends here in California and back in Italy for their continuous love and encouragement. Senza di voi nulla di tutto cio' sarebbe stato possibile.

Curriculum Vitae

First Name: Yari
Family Name: Ferrante
Gender: Male
Date of Birth: December 21st, 1988
Place of Birth: Turin, Italy
Address: 6525 Kaneko Drive, San Jose, 95119 CA, USA
Nationality: Italian

ACADEMIC EDUCATION

06/2013–10/2017 *Doctor of Philosophy in Engineering (Physics)*
Martin-Luther-University Halle-Wittenberg, Halle, Germany

10/2010–09/2012 *Master's Degree in Nanotechnology*
Polytechnic of Turin, Italy
Institute National Polytechnic of Grenoble, France
Ecole Polytechnique Fédérale de Lausanne, Switzerland

10/2007–10/2010 *Bachelor's Degree in Electronics Engineering*
Polytechnic of Turin, Italy

Yari Ferrante
San Jose, California, USA
21st November 2017

Eidesstattliche Erklärung

Hiermit erkläre ich, YARI FERRANTE, dass ich die vorliegende Arbeit mit dem Titel: **Development of tetragonal Heusler compounds with perpendicular anisotropy for Magnetic Random Access Memory applications** in allen Teilen selbständig verfasst und keine anderen als die angegebenen Quellen und Hilfsmittel benutzt habe. Alle wörtlich oder sinngemäß übernommenen Textstellen habe ich als solche kenntlich gemacht.

Ferner liegen gegen mich weder gerichtliche Vorstrafen vor, noch sind staatsanwaltliche Ermittlungen oder Disziplinarverfahren eingeleitet worden.

Des Weiteren erkläre ich hiermit, dass ich bisher keine andere Arbeit zur Promotion eingereicht noch mit einer anderen Arbeit den Versuch zur Promotion unternommen habe.

San Jose, California, USA

den 21. November 2016

YARI FERRANTE